University of Texas at El Paso
ScholarWorks@UTEP

Open Access Theses & Dissertations

2023-05-01

# Study Of Different Heat Treatments And Aging Conditions For Observing Microstructures And Mechanical Properties Of Lpbf Fabricated F357 Alloy

Victor Adrian Medrano Balderas
*University of Texas at El Paso*

Follow this and additional works at: https://scholarworks.utep.edu/open_etd

 Part of the Aerospace Engineering Commons, and the Mechanical Engineering Commons

## Recommended Citation

Medrano Balderas, Victor Adrian, "Study Of Different Heat Treatments And Aging Conditions For Observing Microstructures And Mechanical Properties Of Lpbf Fabricated F357 Alloy" (2023). *Open Access Theses & Dissertations*. 3825.
https://scholarworks.utep.edu/open_etd/3825

This is brought to you for free and open access by ScholarWorks@UTEP. It has been accepted for inclusion in Open Access Theses & Dissertations by an authorized administrator of ScholarWorks@UTEP. For more information, please contact lweber@utep.edu.

STUDY OF DIFFERENT HEAT TREATMENTS AND AGING CONDITIONS FOR OBSERVING MICROSTRUCTURES AND MECHANICAL PROPERTIES OF LPBF FABRICATED F357 ALLOY

VICTOR ADRIAN MEDRANO BALDERAS
Master's Program in Mechanical Engineering

APPROVED:

_____
Francisco Medina, Ph.D., Chair

_____
Ryan Wicker, Ph.D.

_____
Amit Lopes, Ph.D.

_____
Edel Arrieta, Ph.D.

_____
Stephen Crites, Ph.D.
Dean of the Graduate School

Copyright ©

by

Victor Adrián Medrano Balderas

2023

# DEDICATION

Dedicado a mi familia, amigos y compañeros que me ayudaron en este camino.

# STUDY OF DIFFERENT HEAT TREATMENTS AND AGING CONDITIONS FOR OBSERVING MICROSTRUCTURES AND MECHANICAL PROPERTIES OF LPBF FABRICATED F357 ALLOY

by

VICTOR ADRIAN MEDRANO BALDERAS

THESIS

Presented to the Faculty of the Graduate School of
The University of Texas at El Paso
in Partial Fulfillment
of the Requirements
for the Degree of

MASTER OF SCIENCE

Department of Aerospace and Mechanical Engineering
THE UNIVERSITY OF TEXAS AT EL PASO
May 2023

# ACKNOWLEDGEMENT

First and foremost, I express my gratitude to Dr. Francisco Medina, my boss, advisor, and, most importantly, my mentor. I will be eternally grateful to him for allowing me to work at the W.M. Keck Center for 3D Innovation for almost two years, motivating me every day at the laboratory, and trusting me to pursue new objectives and goals.

I also want to express my deepest gratitude to Dr. Edel Arrieta; I'm entirely sure that most of the knowledge I got from the laboratory it's thanks to him; his hard work is something every work need; every company needs an Engineer as Dr. Edel Arrieta, his endless knowledge of every topic and way of work are the most admirable attributes a person could have.

I want to recognize the work and support of the different friends I made over the years at UTEP; I'm sure that this hasn't have been possible without the support of these people from the Mechanical Engineering Department as well as the people from the W.M. Keck Center for 3D Innovation, they have given me so much and helped me grow professionally and most important, personally.

Lastly, and most importantly, I want to thank my family. My dad, Jaime Medrano, my mom, Lorena Balderas, and my siblings, Jaime, Vania, and Erick Medrano, have given me everything; I am pretty sure I haven't been here without their unconditional support and love; this goal is also yours.

# ABSTRACT

Aluminum F357 is a widely used material for casting in the aerospace and additive manufacturing industry. Heat treatments are commonly applied to some aluminum alloys to modify their properties. With a further study on the aging and performance of the F357 with 3D printing technology, several industries benefit from this; military, automotive, and aerospace are some examples because of the numerous components cast in service. This work presents the mechanical properties of F357 specimens fabricated with EOS technology and subjected to heat treatments.

Heat treatment conditions were applied to tensile specimens and tested. Furthermore, the specimens were subjected to artificial thermal aging for 100 h and 1000 h at two different temperatures (285 ºF and 350 ºF), and their mechanical properties were also determined. Finally, remarks on the comparison between the heat treatments and the effect of thermal aging on the microstructures and mechanical properties of the specimens will be presented.

# TABLE OF CONTENTS

# LIST OF TABLES

# LIST OF FIGURES

# CHAPTER 1: INTRODUCTION

3D printing, or as is known in the industry, additive manufacturing, refers to the layer-by-layer deposition of material to build a three-dimensional structure or design directed from a design file designed on CAD software [1]. This technology allows complex geometries that shouldn't be possible with traditional techniques such as casting or machining, which consist of "substrate" the material instead of adding. Also, additive manufacturing technologies have been increasing in his quality to reach the requirements of the industry and products; as a result, a dramatic increase in the number of scientific publications related to additive manufacturing in the area of metals; the mainly studied metals are steel, titanium, and aluminum alloys; for the latter, the primary type of additive manufacturing technology used is laser powder bed fusion (LPBF), also known as selective laser melting (SLM) [2].

Additive manufacturing has many benefits, such as the freedom of the design, reduced time and money waste, and improved process efficiency [3]. However, additive manufacturing needs several investigations on distinct processes that nowadays still have limitations, known as defects. In Laser Powder Bed Fusion (LPBF), defects can be related to the printing parameters, such as hatch spacing, laser speed, laser power, layer thickness, and printing orientation, among others. Some of the most common defects in LPBF are lack of fusion, keyhole, bailing, and gas porosity, which depend on the parameters, powder feedstock, and performance of the machine to avoid them; a longer explanation of each defect is included in the paper.

The two most important parameters of any build using a Laser Powder Bed Fusion printer are the laser speed and laser power; these two parameters will directly affect the quality of the print; to achieve the highest possible density, ten different variables of parameters are included in trial builds to evaluate which parameters composition were the most appropriate for this printing.

In this project, metallography and density tests will be evaluated and posteriorly check the effectiveness of the parameter's setups. After evaluating and selecting the efficient parameter setup, printing can begin.

According to several investigations, every additive manufacturing component requires heat treatment to improve mechanical properties on the part; the present work investigates the differences between heat treatments, T6, HIP, and Stress Relief will be investigated and compared to determine the mechanical properties of each heat treatment; these heat treatments improve the homogenization of the mechanical characteristics and microstructure of the printed part [4]. Also, artificial aging has been applied to increase strength and temperature stabilization, creating the finest precipitations on the microstructure. On additive manufacturing parts, recent studies have shown heat treatments like Hot Isostatic Pressure reduce porosity and increase the density of the piece, or T6 technique, where the microstructure becomes more constant and uniform, and, as with HIP technique, some porosity is reduced, and the SI precipitates become very fine after the T6 heat treatment.

Finally, the application of different aging conditions and heat treatments to LPBF parts is worthwhile for understanding the material at different aging and heat treatment conditions. Currently, there is no ASTM standard for treating aluminum F357. However, the ASTM F3318 standard will be followed for heat-treating F357. Studies have shown the modification of microstructure and of the mechanical properties at room temperature (25 °C) of laser powder bed fusion aluminum F357 parts involve a variety of post-process heat treatments [5].

In this paper, different processes from additive manufacturing, LPBF technology printing, heat treatments and aging, microstructure analysis, mechanical properties analysis, among others, are explored.

## 1.1 F357 Background

The study of aluminum microstructure and mechanical properties is of interest since this metal is among one of the most abundant elements on Earth, and its properties turn aluminum into a suitable material for various applications. According to Rashad, et al. [6], Tsaknopoulos, et al. [7] and Dahle, et al. [8], various heat treatments and many other metals such as silicon, magnesium, titanium, and chrome are applied to aluminum to change its mechanical properties and microstructure, making it better for different cases and applications. Among aluminum-silicon castings, there is aluminum F357 (AlSi7Mg), a lightweight alloy (2.67 g/cm3 density) with good laser processability, also; this alloy is also called A357, depending on the quantity of beryllium on the material that is usually 0.002% as maximum on the F357, compared with A357 aluminum, which usually contains between 0.04% to 0.07% [9], which means that it changes the dimensions and shapes of the precipitates, the presence of beryllium in the alloys improves the mechanical properties of the part, such as hardness, the corrosion resistance, tensile resistance, and usually reduces the fatigue propagation. On the other hand, the F357 alloy causes a safety problem because of the presence of beryllium, but recent studies have shown that different post processes, such as heat treatments and artificial aging, reduce the residual stresses and modify the microstructure of the part, as well as the mechanical properties compared to the as-built original part conditions [10].

The F357 has been a big part of engineering and manufacturing over the past decades, turning it into one of the most used metals for aircraft parts and aerospace components. In addition, many other aluminum alloys are constantly used in many other industrial processes; some of the applications of aluminum include the fabrication of automotive components such as heat exchangers, chassis frames, and bodywork.

These components usually keep a geometry that is reachable with classic manufacturing processes such as pressure die casting; nevertheless, some other components require more complex geometries, and classic manufacturing methods usually present limitations to these complex geometries since they often produce undesired defects such as porosity on critical areas. With the relatively new appearance of metal additive manufacturing, specifically Laser Powder Bed Fusion (LPBF) technology, these limitations have been largely overcome since many parameters (layer thickness, hatch distance, energy density, etc.) can be modified in order to reduce the appearance of undesired defects. LPBF fabricated parts of aluminum F357 have shown nominal yield stress (YS) of 400 MPa, in contrast with 170 MPa for cast parts [11].

## 1.2 Motivation

Further, the understanding of AM printed parts and postprocessing, such as heat treatments and different aging conditions. Compare the mechanical properties of ASTM F3318 heat treatments and additional aging, as well as the microstructure of all the samples. And finally, a report on the fabrication of F357 printed parts subjected to these heat treatments and aging conditions.

## 1.3 Thesis Objective

- Print the most optimal parts with Laser Powder Bed Fusion F357 aluminum.
- Characterize and analyze F357 microstructure.
- Characterize and analyze F357 mechanical properties.
- Compare the results of how different heat treatments and aging conditions affect F357 printed parts.

# CHAPTER 2: LITERATURE REVIEW

## 2.1 Additive Manufacturing

Additive Manufacturing, also known as 3D printing, refers to the layer-by-layer deposition of a specific material to build a 3-Dimensional part structure directly from a computer-aided design file [12], also known as CAD, by his initials; it consists of designing a part in this software, then exported to the 3D printer to start the building of the part, taking in consideration the limitations of each machine and technology, sometimes supports must be necessary for the successful printing of these parts.

AM technologies have several advantages compared to traditional manufacturing techniques, such as subtractive manufacturing, because additive manufacturing offers an economical and ecological potential [13], using less material to create a part and less waste material; additive manufacturing also allows the building of complex parts, lighter and faster products, with this innovative manufacturing and designing [14].

The additive manufacturing technologies have seven different categories, which are Binder Jetting, Powder Bed Fusion, Material Jetting, Vat Photopolymerization, Direct Energy Deposition, Sheet Lamination, and Material Extrusion; each of them has different functions and different purposes, depending on the quality and standards of the printed parts.

For the fabrication of a metal structure, several steps must be followed, and depending on the manufacturing, some stages may be different of removed [15]; also, we must take into account the application of the printed part; it's different if the part will be used just for prototype purposes, or it will be an industrial or production part. In Figure 1, a flow diagram summarizes the steps followed to complete a successful AM process.

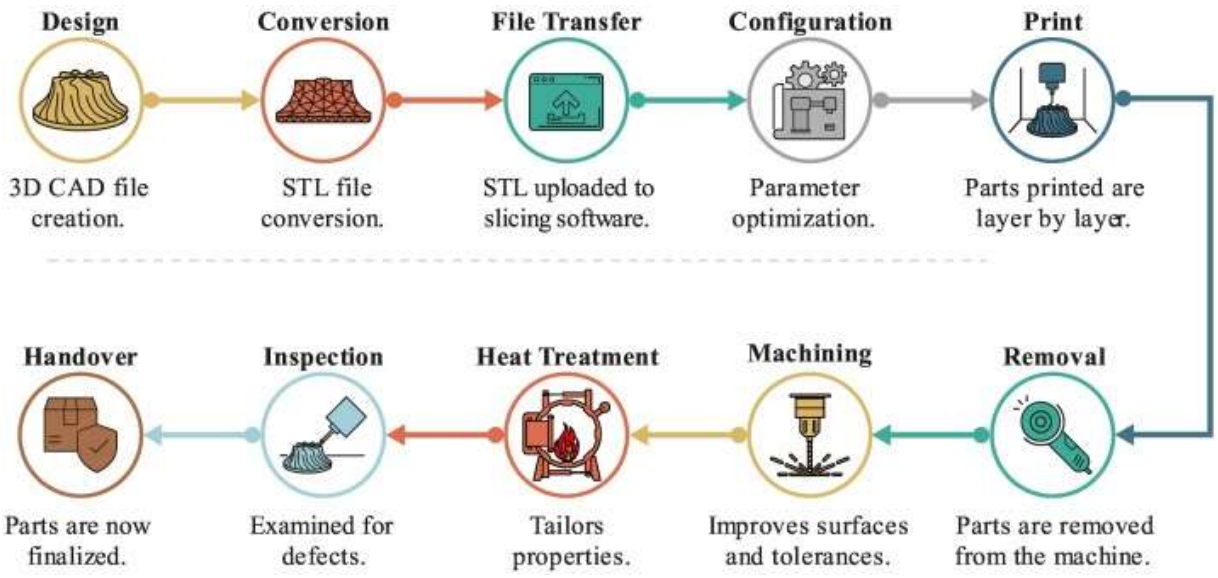


Figure 1. Example of a typical AM workflow [16].

For a better understanding of Figure 1, each step will be briefly described in the next paragraphs:

- Design: for the creation of an additive part, you first need a digital representation of the product. To achieve this, a 3D CAD model must be created; a CAD (computer-aided design) is the use of computer-based software to aid in design processes [17], [18].

- Conversion: to be understood by the printer machine, the file must be converted into a specific type of data called STL (stereolithography) [19], that basically convert every face of the design into triangles to create coordinates and be understood by the software machine. STL file maybe will have dimensional errors due to the way this file creates shapes.

- File transfer: once the STL file is ready, this must be transferred to slicer software for the machine, which converts the 3D design into 2D layers, which are calculated from the STL file.

- Configuration: before printing, parameters must be optimized to have better properties for the printed part; this includes all the process parameters related to the machine and technology used, such as orientation, layer thickness, among others.

- Print: printing varies depending on the technology used, the size, and the geometry of the part, is the most important part of the complete process, at the same time, is typically the most time-consuming; it can take from hours for a small and simple design or days for a big and complicated design.

- Removal: depending on the technology used, removal steps vary, most of the technology consists of taking out the part from the chamber and removing it from the build plate, but some technologies may need debinding processing or sintering processing.

- Machining: after the part is completely printed, machining may be required, most of the time in the removal of the supports used to print the part of the separation of the part from the build plate, for example, in a metal part that was printed in a metal plate.

- Heat Treatment: optional step; depending on the application or purpose of the part [20], different heat treatments can provide microstructure homogeneity and improve the mechanical properties of the printed part [21].

- Inspection: parts are subjected to external testing, such as surface roughness, visual test, and dimensional accuracy.

- Handover: part is finalized, ready to use, or sent to the customer or company.

### 2.1.1 Laser Powder Bed Fusion

Laser powder bed fusion is one of the most common metal additive manufacturing technologies in the industry to create a 3D object [22]; compared to other commonly used alloys such as titanium and steel, aluminum is the most used alloy for this technology [23], it can use a laser beam or an electron beam, the technologies used are direct metal laser sintering, selective laser melting, selective laser sintering, or electron beam melting [24]. Some advantages this technology has are the high accuracy and high resolution of the parts, with high strength due to the denseness of the parts. But this technology also has several disadvantages, principally the residual stress due to the inconsistent heating and cooling of the process during the melting or sintering of the powder, it can only use a single material at a time, and require support structures most of the times, mainly in complicated designs.

Laser powder bed fusion consists, as with every other additive manufacturing technology, it prints a 3D part layer by layer; in this specific technology, a roller or rake transports the powder from the powder dispenser, which can be a platform next to the build platform or a hooper that transports the powder from one side to another, this new powder is placed in the powder bed and, depending on the technology, a laser or an electron beam melt or sinter the powder to create a solidified portion of the design, then, the platform is lowered the layer thickness establish in the process parameters, and a new layer of powder is deposited in the powder bed, these steps continue repeating until the part is complete [25]. To prevent the oxidation of the material during the process, an inert gas is used; argon and nitrogen are commonly the principal gases used to avoid it [26].

The laser beam work with a set of mirrors, with the purpose of redirecting the laser to the desired path's direction [27]. As with other additive manufacturing technologies, laser powder bed

fusion deal with different defects during production, mainly the porosity, fusion errors, shrinkage on the structure during printing, and gas errors; all these contribute to the porosity of the part. Figure 2 illustrates a schematic for a common LPBF system.

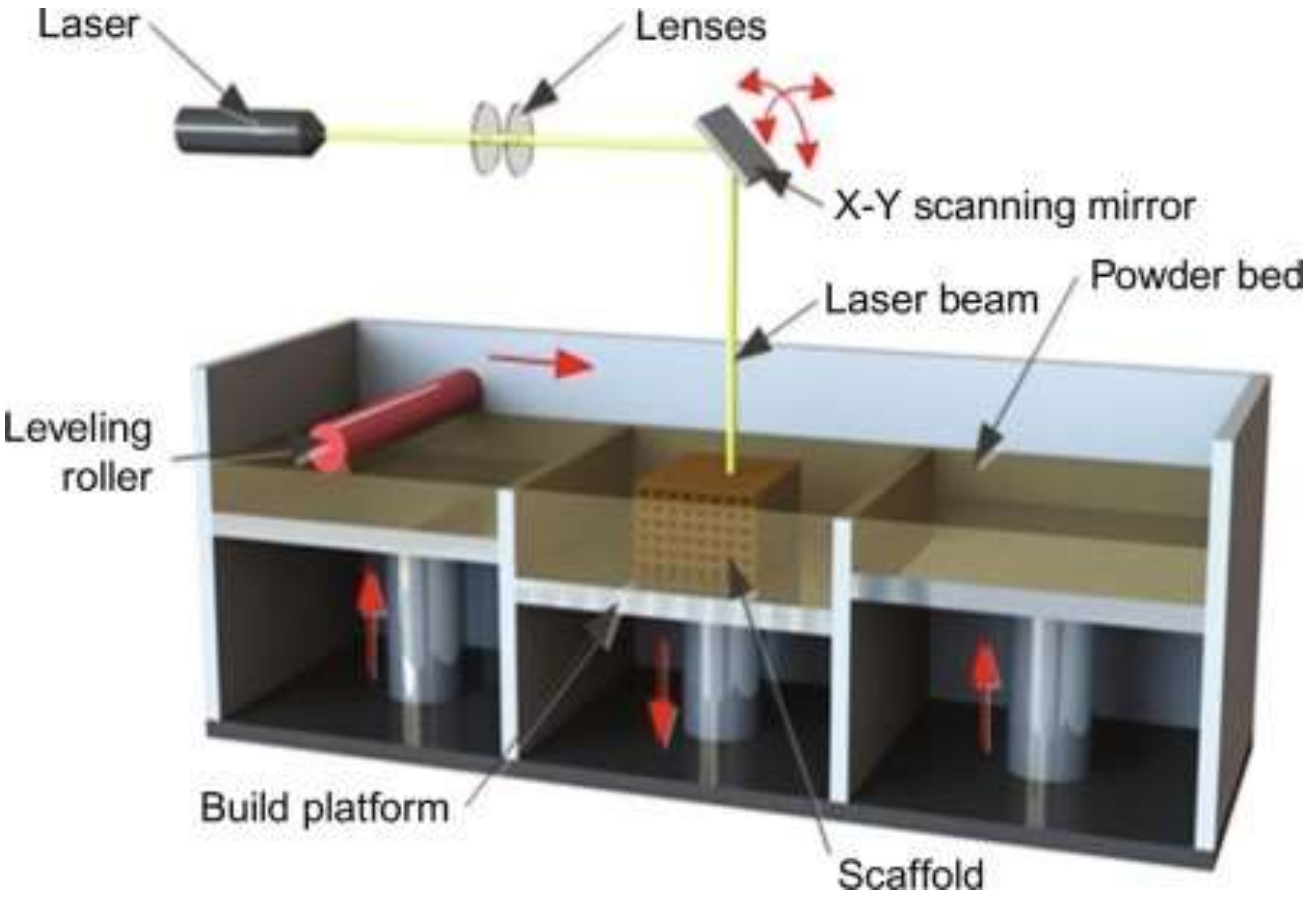


Figure 2. Laser powder bed fusion process [28].

### 2.1.2 Electron Beam Melting

Electron beam melting (EBM) is another powder bed fusion technology; instead of a laser, this technology uses an electron gun running at 4kW with a better plug efficiency than a laser beam; this is one of the few differences with a laser powder bed fusion printer. Another important difference is that the EBM fabrication process requires a vacuum environment to avoid the interaction between air and electrons [29] to produce dense and complex parts. Regarding these two main differences, EBM technologies work similarly to a laser powder bed fusion machine; a uniform layer of powder is placed in the build plate and dispersed by a rake, repeating this step until the process is done.

Some of the disadvantages of EBM is the reduced palette of materials available; these are limited to CoCr, titanium, and superalloys due to the difficult process of optimizing the process parameters for other materials [30]. Smoking is one of the most common defects in EBM, consisting of the jumping of powder particles from the bed. To prevent smoking, the build plate and powder are preheated to sinter the powder particles before melting; this is one of the principal differences between EBM and LPBF, the high temperature at the EBM machines print. As a result of this, it improves the mechanical, chemical, and material properties. Figure 3 illustrates the schematic Electron Beam Melting process.

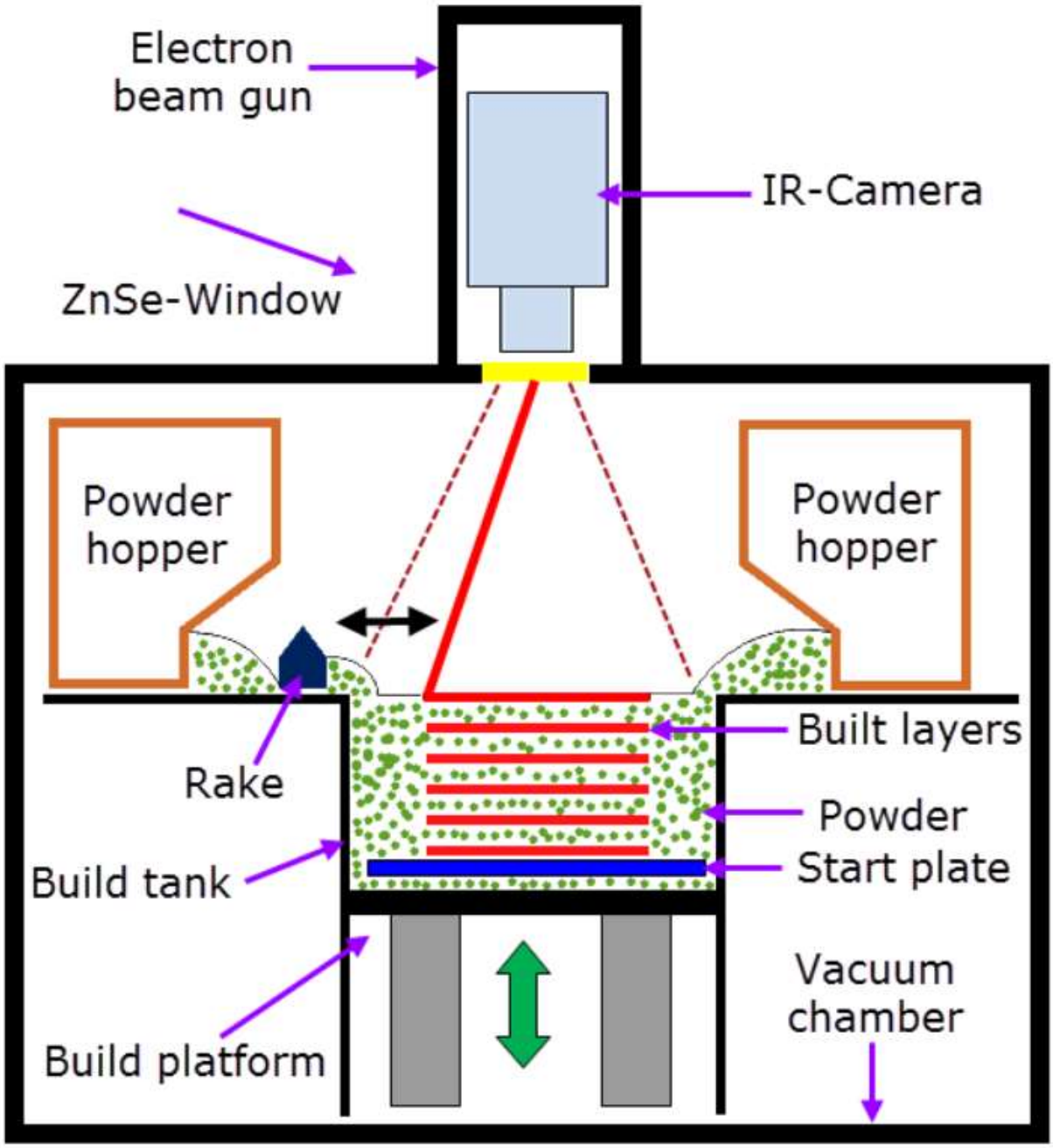


Figure 3. Schematic of Electron Beam Melting [31]

## 2.2 Laser Powder Bed Fusion Defects

In laser powder bed fusion, the process parameters affect the quality of the printed part; as it was already mentioned, parameters that can affect the part are the layer thickness, laser power, scan speed, the hatch spacing, among others, even with the huge progress among the years. To ensure a full density of a part, an optimal combination of these parameters should be performed; that's why before any printing, a parameter development should be run to try different combinations of parameters and get the highest density possible for the specific material, for this process, tools like a pycnometer can be used to calculate the specific density of the part.

After printing, finished parts contain residual stresses all over the body that create cracks and distortion of the part, derivate from these stresses that are caused by the quick solidification and variable cooling rates of the process [32]. These defects affect the performance of the part; mechanical and thermal properties can vary due to the residual stresses in the part. McClung [33] has shown that a large presence of residual stresses can directly affect the fatigue and tensile performance of the part. To avoid these problems, several strategies have been followed, like heating the building platform/plate before every print [34].

During the creation of 3D printed parts, microstructural defects are also created due to the parameters of the printing, such as gas porosity, lack of fusion, keyhole, and balling; these problems affect the density of the part and their mechanical properties, to avoid these, specific strategies should be followed to prevent it [35].

### 2.2.1 Gas Porosity

This defect refers to the type of porosity already on the powder induced by the gas atomization process but also to the entrapped gases created because of the weld pool instabilities [36]. The gas bubbles trapped in the powder can result in porosity once these particles are melted to create a solid part; these pores have a spherical shape on the sample and can be easily identified [37]. Due to the fast solidification process of laser powder bed fusion, these bubbles can't escape during the melting [38]. Figure 4 illustrates an example of gas porosity.

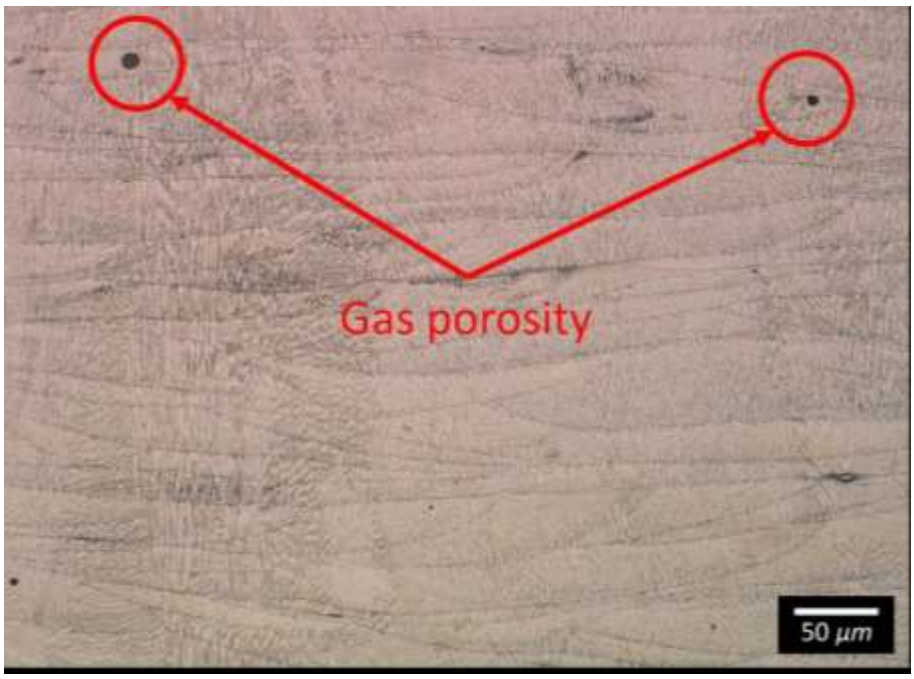


Figure 4. Example of gas porosity formed during Laser Powder Bed Fusion process [39].

### 2.2.2 Keyhole

Spherical shaped pores usually with a diameter of less than 100 µm produced by deep penetration due to an excessive amount of energy input by the laser on the metal powder bed, keyhole density and size will increase as energy input increases. In addition, just like any other

defect keyholes will also affect the mechanical properties of the material and will be visible on micrographs [40],[41].

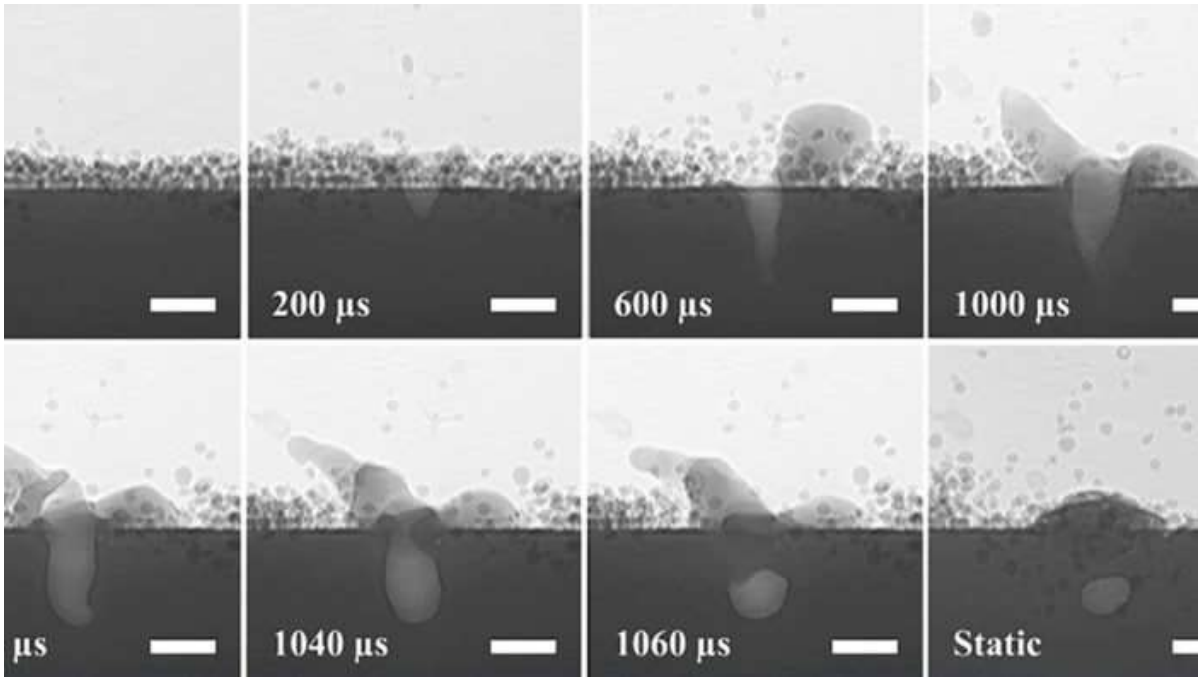


Figure 5. Formation of keyhole [42].

### 2.2.3 Lack of Fusion

Lack of energy input by the laser on the metal powder bed and insufficient overlapping of melt pools between the layers and track will lead to unmelted powder-producing porosity. Lack of fusion (LoF) will affect the mechanical properties of the material and potentially cause failure. The pores in lack of fusion are formed at very low energy densities [41]. Keyholes are aligned with layer direction, and unmelted powder particles are common to observe due to the lack of fusion, and these unfused particles act as the initiation of cracks during fatigue testing. With the lack of fusion porosity, is common the increase of interlayer bonding and a rough surface finish [43].

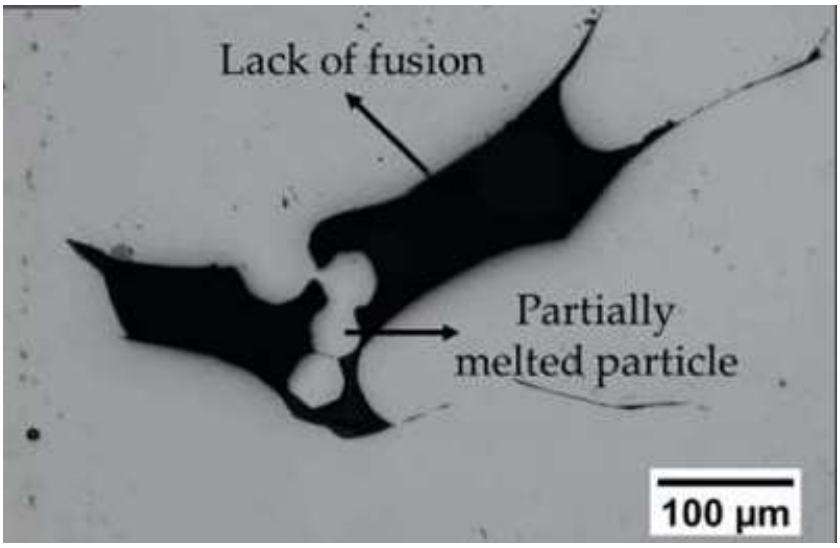


Figure 6. Lack of fusion defect present in LPBF process *[44]*.

Shape and size of the weld pool is defined and controlled by the input parameters, specifically the energy density based on a specific zone [45].

### 2.2.4 Balling

Produced by an overflow of the melt pool which then solidifies, this overflow is usually produced by excessively fast scanning speed and energy input by the laser. These defects can be easily noticed on exterior surfaces since a bump will be visible. In addition, balling is a surface tension-based defect where the melt pools collect creating spherical balls during the sintering process [46]. For example, high laser power and slow scanning speed can result in excessive melting and overheating of the powder, leading to the formation of balling porosity. Similarly, using a powder material with poor thermal conductivity or a low melting point can also increase the likelihood of balling porosity formation [47], [48].

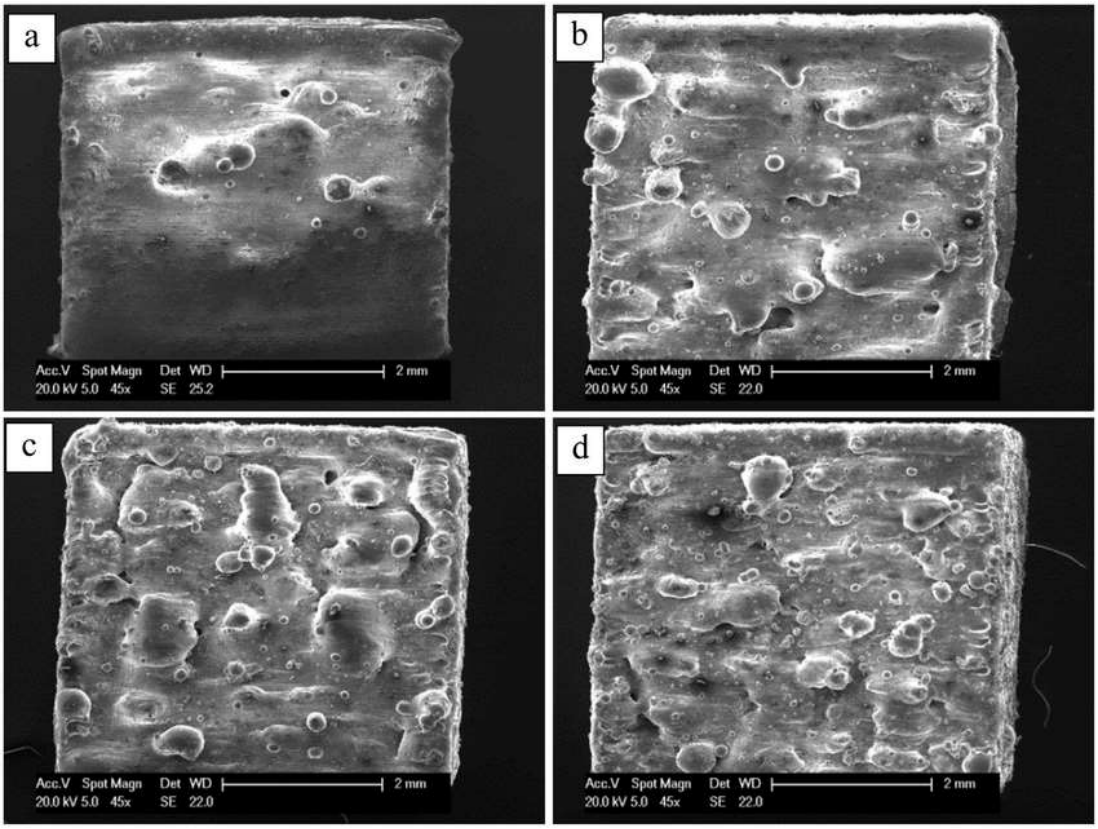


*Figure 7. Balling effect with different scanning speeds [49, p. 6], [50].*

## 2.3 Heat Treatments

Heat treatments are necessary for most of the laser powder bed fusion printed parts; it only varies depending on the specific material used, the intended application of the piece, and the decided properties of the final printed part [51], [52]. Also known as the post-processing of post-printing process, heat treatments are a second step that involves the parts to heating and cooling cycles to change specific properties or microstructure of the part.

There are many purposes for a part to be subjected to a heat treatment, but some of the main ones are:

- Improving mechanical properties: Heat treatment can help optimize the mechanical properties of LPBF printed parts by modifying their microstructure. For example, it can be used to refine the grain structure, reduce residual stresses, and improve the material's

strength, toughness, and fatigue resistance. Heat treatment can also help relieve residual stresses that may have accumulated during the LPBF process, which can minimize the risk of part distortion or cracking [53], [54].

- Enhancing material properties: Heat treatment can be used to induce desired material properties in LPBF printed parts. For example, it can be used to increase the hardness, wear resistance, or corrosion resistance of the material, depending on the specific heat treatment process used and the material being printed [55].
- Achieving specific microstructural changes: Heat treatment can be used to achieve specific changes in the microstructure of the material, such as phase transformations or precipitation hardening [56]. This can result in desired material properties, such as improved thermal or electrical conductivity, magnetic properties, or other specific characteristics [57].
- Removing residual stresses: LPBF printed parts can accumulate residual stresses during the printing process due to the rapid heating and cooling cycles involved. Heat treatment can help relieve these residual stresses, reducing the risk of part distortion, cracking, or failure during service [33].
- Ensuring dimensional stability: Heat treatment can be used to minimize dimensional changes that may occur during the LPBF process, such as part shrinkage or warping, by stabilizing the material's microstructure.

### 2.3.1 SR1

Stress relief is a type of heat treatment looking for the reduction of residual stresses inside the part; these stresses were introduced or created during the manufacturing printing process. Residual stresses can have negative effects on the mechanical properties and dimensional stability of metal printed parts. They can cause part distortion, warping, or cracking and can potentially reduce the overall performance and reliability of the parts. Stress relief heat treatment is used to alleviate or minimize these residual stresses, leading to improved part quality and performance [58], [59].

The stress relief process typically involves heating the metal printed parts to a specific temperature below the recrystallization temperature of the material and holding them for a certain amount of time, typically hours; this allows the material to undergo plastic deformation inside the part and relaxation of the internal stresses, then, the part is cooled at room temperature to avoid new stresses to the part [59].

Based on the material used, specific temperatures, duration, and cooling rates will be used. Also, the part geometry and the desired stress relief level are important for the heat treatment, as well as the process parameters of the printed part to determine the optimal stress relief heat treatment parameters [60].

### 2.3.2 HIP

HIP, or Hot Isostatic Pressing, is a type of heat treatment process used for metal printed parts to improve their density, integrity, and mechanical properties. HIP is a post-printing treatment that involves subjecting the metal-printed parts to high temperature and pressure in an inert gas environment, typically argon, to consolidate and densify the material [61].

During the HIP process, the metal printed parts are placed in a sealed container, often referred to as a HIP can or HIP capsule, along with a protective gas, such as argon. The container is then heated to a high temperature, typically above the material's recrystallization temperature, and pressurized uniformly from all directions using an isostatic press. The high temperature and pressure cause the material to undergo plastic deformation, allowing for the consolidation of voids, porosities, and other defects that may have formed during the metal printing process. The pressurizing effect helps to close porosities and create a more homogeneous and dense material [61]–[64].

The HIP process can significantly improve the density and mechanical properties of metal printed parts, such as tensile strength, fatigue resistance, and toughness, by reducing the presence of voids, porosities, and other defects that may be inherent in metal printed parts [65]. It can also enhance the material's isotropic properties, as the applied pressure during HIP helps to equalize the material's properties in all directions, resulting in more uniform mechanical behavior [62]–[64].

HIP is commonly used for metal printed parts made from various materials, including but not limited to titanium, stainless steel, nickel-based superalloys, and other high-performance alloys. It is often employed in aerospace, medical, and other high-performance applications where the material's integrity and mechanical properties are critical for the part's performance and reliability.

It's worth noting that the HIP process is typically carried out by specialized equipment and requires careful control of temperature, pressure, and other process parameters to achieve the desired results. The specific HIP parameters, such as temperature, pressure, and duration, may vary depending on the material used, the part's geometry, and the desired properties of the final parts

and should be determined based on material and process characterization, as well as part performance requirements [66].

### 2.3.3 T6

T6 heat treatment, typically applied to aluminum alloys, is the designation for the tempering process that the parts undergo, which involves the heating of the parts to a specific temperature and then cooling rapidly with water or oil.

The process of this heat treatment consists of heating the part above the alloy's solidus temperature and holding them to dissolve any precipitates or other phases that may have formed during the printing process; this step is followed by the quenching process.

Quenching is defined as the process of rapidly cooling a part after it has been heatedly treated using water or oil; depending on the liquid used, a different surface finish will be left on the outer layer of the treated part. The quenching process will considerably increase the hardness of the outer layers while maintaining ductility at the inside of the part; this makes it appropriate for mechanical parts that require high wear and corrosion resistance yet be able to absorb mechanical loadings without fracturing [67].

During a quenching process, the external walls of the part are rapidly cooled down, and grains at the surface considerably reduce their size, pulling inner grains, which are still hot and malleable, producing tension among the part [68]. In order to release this tension, the part can be subjected to a stress relief treatment where the part will be under high temperatures and then be air-cooled, allowing grains to properly arrange without producing any internal tension. This process usually decreases strength and hardness [69], [70].

## 2.4 Aging

Aging, also known as precipitation hardening, is a heat treatment process used for certain metal printed parts to enhance their mechanical properties, particularly strength, and hardness. Aging heat treatment is typically performed after the initial heat treatment, such as solutions and quenching, and it involves a controlled heating and cooling process to encourage the formation of fine precipitates within the material's microstructure. The aging process is commonly used for metal printed parts made from precipitation-hardening alloys, which are materials that exhibit a phase transformation from a supersaturated solid solution to a more stable state, resulting in the formation of small precipitates within the microstructure. These precipitates act as obstacles to the movement of dislocations, which are responsible for plastic deformation in metals, and thus strengthen the material [71]–[73].

The aging heat treatment typically involves two main steps: precipitation and aging. In the precipitation step, the metal printed parts are heated to a specific temperature, known as the aging temperature, which is typically below the material's melting point but above its room temperature. This allows for the formation of fine precipitates within the material's microstructure through a process called nucleation and growth. The parts are then held at this temperature for a certain duration of time to allow the precipitates to fully form and grow to the desired size and distribution [71], [74], [75].

After the precipitation step, the metal printed parts are typically cooled rapidly to room temperature in a process called quenching. This helps to trap the precipitates in the microstructure and prevent them from coarsening. The parts are then subjected to the aging step, where they are heated again, but this time to a lower temperature compared to the precipitation step, and held at

that temperature for a specific duration of time. This allows the precipitates to further strengthen the material through a process called age hardening [76], [77].

The aging heat treatment can significantly improve the mechanical properties of metal printed parts, particularly their strength, hardness, and sometimes even toughness. It can also affect other material properties, such as corrosion resistance, fatigue performance, and dimensional stability. The specific aging heat treatment parameters, such as temperature, duration, and cooling rate, are typically determined based on the material used, the part's design, and the desired properties of the final parts and require careful consideration and optimization to achieve the desired results [5], [71], [78], [79].

## 2.5 F357 Applications

AlSi7Mg alloy is commonly used in various applications, such as structural components in aerospace, automotive, and marine industries, as well as in general engineering and construction. It offers good strength, excellent machinability, and good corrosion resistance, making it suitable for a wide range of applications [7]. Additionally, AlSi7Mg alloy can be heat treated to improve its mechanical properties, such as strength and hardness, as we already discussed in this paper. It is important to note that specific properties and characteristics of AlSi7Mg alloy may vary depending on the specific heat treatment, temper, and processing conditions used [10]. Each application is specifically described in the following text:

- Aerospace: AlSi7Mg alloy is used in the aerospace industry for structural components such as aircraft wings, fuselages, and landing gear due to its high strength-to-weight ratio and good machinability.

- Automotive: This alloy is utilized in automotive applications such as engine components, suspension parts, and structural components due to its high strength, good corrosion resistance, and weldability.
- Marine: AlSi7Mg alloy is suitable for marine applications such as boat hulls, marine structures, and offshore platforms due to its corrosion resistance in saltwater environments.
- General engineering: It is used in general engineering applications, including machined parts, brackets, and frames, due to its good machinability and mechanical properties.
- Construction: AlSi7Mg alloy is utilized in construction applications such as scaffolding, ladders, and structural components due to its strength, durability, and corrosion resistance.
- Sports equipment: This alloy is used in the manufacturing of sports equipment such as bicycle frames, climbing gear, and sports accessories due to its lightweight and high-strength properties.
- Electrical industry: AlSi7Mg alloy is used in electrical enclosures, heat sinks, and other electrical components due to its good thermal conductivity and electrical conductivity.
- It's important to note that the specific applications of AlSi7Mg alloy may vary depending on the requirements of the industry or application and proper engineering considerations and testing should always be undertaken to ensure suitability and performance.

# CHAPTER 3: EXPERIMENTAL METHODS

## 3.1 Powder Feedstock

The powder utilized in the EOS system was atomized F357 (AlSi7Mg), shown in Table 1 and Figure. 11 (a) and (b), provided by Valimet, AM 357C (Stockton, California). A Retsch Camsizer X2 (Haan, Germany) was used in order to study the particle size and shape of the powder through dynamic image analysis with a two-camera system; the Camsizer yields consistent particle size distribution and shape analysis. The stock powder had a particle size distribution of D10: 24.4 μm, D50: 39.3 μm, and D90: 60.4 μm.

Table 1. Powder chemical composition (wt-%) for EOS and SLM

| Alloy | Al | Si | Fe | Cu | Mn | Mg | Zn | Ti | Be | Other elements, each | Other elements, total |
|---|---|---|---|---|---|---|---|---|---|---|---|
| F357 EOS | Balance | 6.5 - 7.5 | 0.10 | 0.20 | 0.10 | 0.40 - 0.70 | 0.10 | 0.04 - 0.20 | 0.002 | 0.05 | 0.15 |
| F357 SLM | Balance | 7.1 | 0.08 | 0.001 | 0.001 | 0.56 | 0.002 | 0.07 | - | - | - |

The powder utilized in the SLM system was atomized F357 (AlSi7Mg) shown in Table 1; supplied by IMR Metal Technologies (Frankfurt am Main, Germany). The powder had a particle size distribution of D10: 26.4 μm, D50: 39.7 μm, and D90: 59.7 μm.

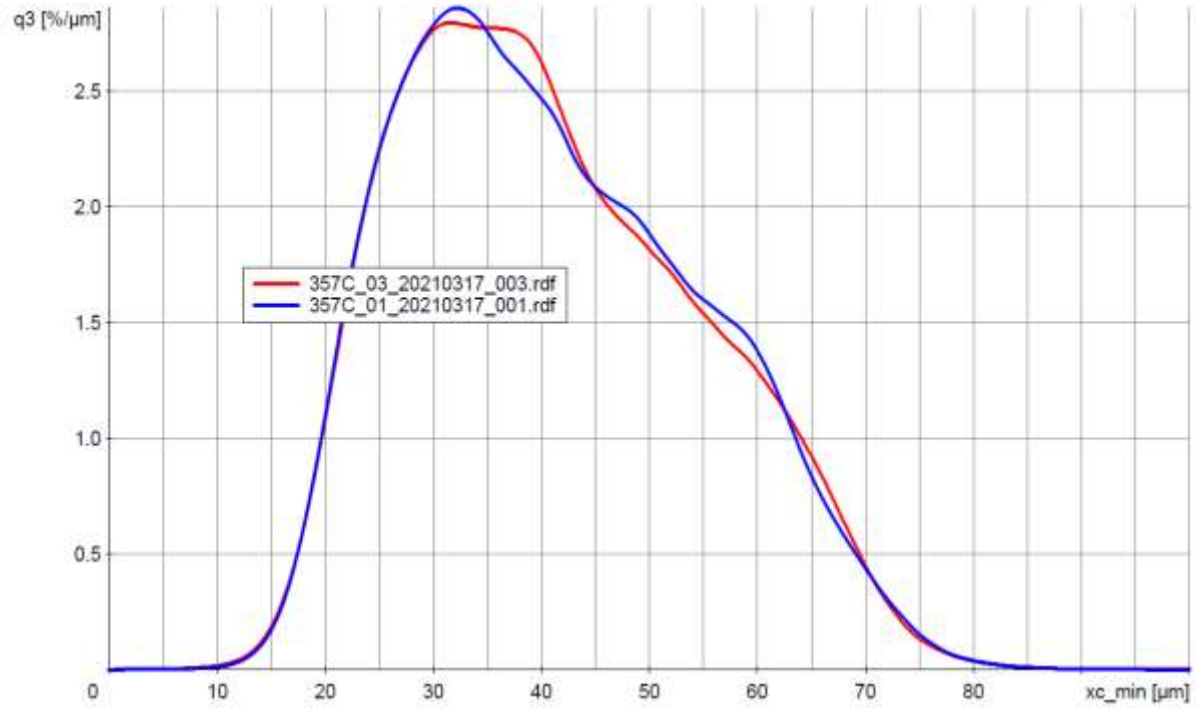


Figure 8. Particle Size Distribution (EOS)

| Size class | [µm] | p3 [%] | Q3 [%] | 1-Q3 [%] | q3 [%/µm] | xc_min3 | Compct3 |
|---|---|---|---|---|---|---|---|
| 0.0 | 10.0 | 0.04 | 0.04 | 99.96 | 0.004 | 7.0 | 0.890 |
| 10.0 | 20.0 | 2.43 | 2.47 | 97.53 | 0.243 | 18.1 | 0.902 |
| 20.0 | 30.0 | 21.88 | 24.35 | 75.65 | 2.188 | 25.6 | 0.910 |
| 30.0 | 40.0 | 27.25 | 51.60 | 48.40 | 2.725 | 34.7 | 0.905 |
| 40.0 | 50.0 | 21.60 | 73.20 | 26.80 | 2.160 | 44.7 | 0.896 |
| 50.0 | 60.0 | 16.21 | 89.41 | 10.59 | 1.621 | 54.8 | 0.896 |
| 60.0 | 70.0 | 8.73 | 98.14 | 1.86 | 0.873 | 66.5 | 0.905 |
| 70.0 | 80.0 | 1.68 | 99.82 | 0.18 | 0.168 | 73.5 | 0.910 |
| 80.0 | 90.0 | 0.13 | 99.95 | 0.05 | 0.013 | 84.3 | 0.885 |
| 90.0 | 100.0 | 0.02 | 99.97 | 0.03 | 0.002 | 93.9 | 0.891 |
| > 100.0 | | 0.03 | 100.00 | 0.00 | 0.000 | 112.2 | 0.921 |

Figure 9. Particle Size Class Distribution (EOS)

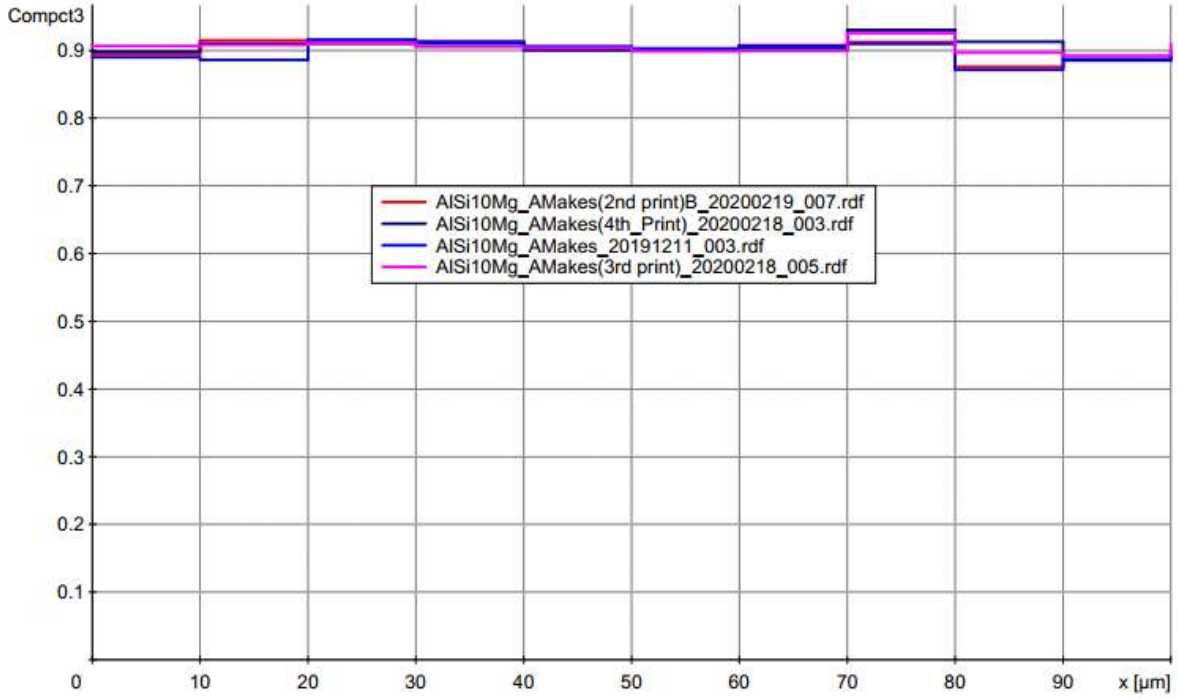


Figure 10. Particle Shape Distribution (EOS)

For further analysis, a JEOL JSM-IT500 Scanning Electron Microscope (SEM) was used to produce images and for analysis which revealed minimal porosity and spherical morphology of the powder, shown in Figure 11.

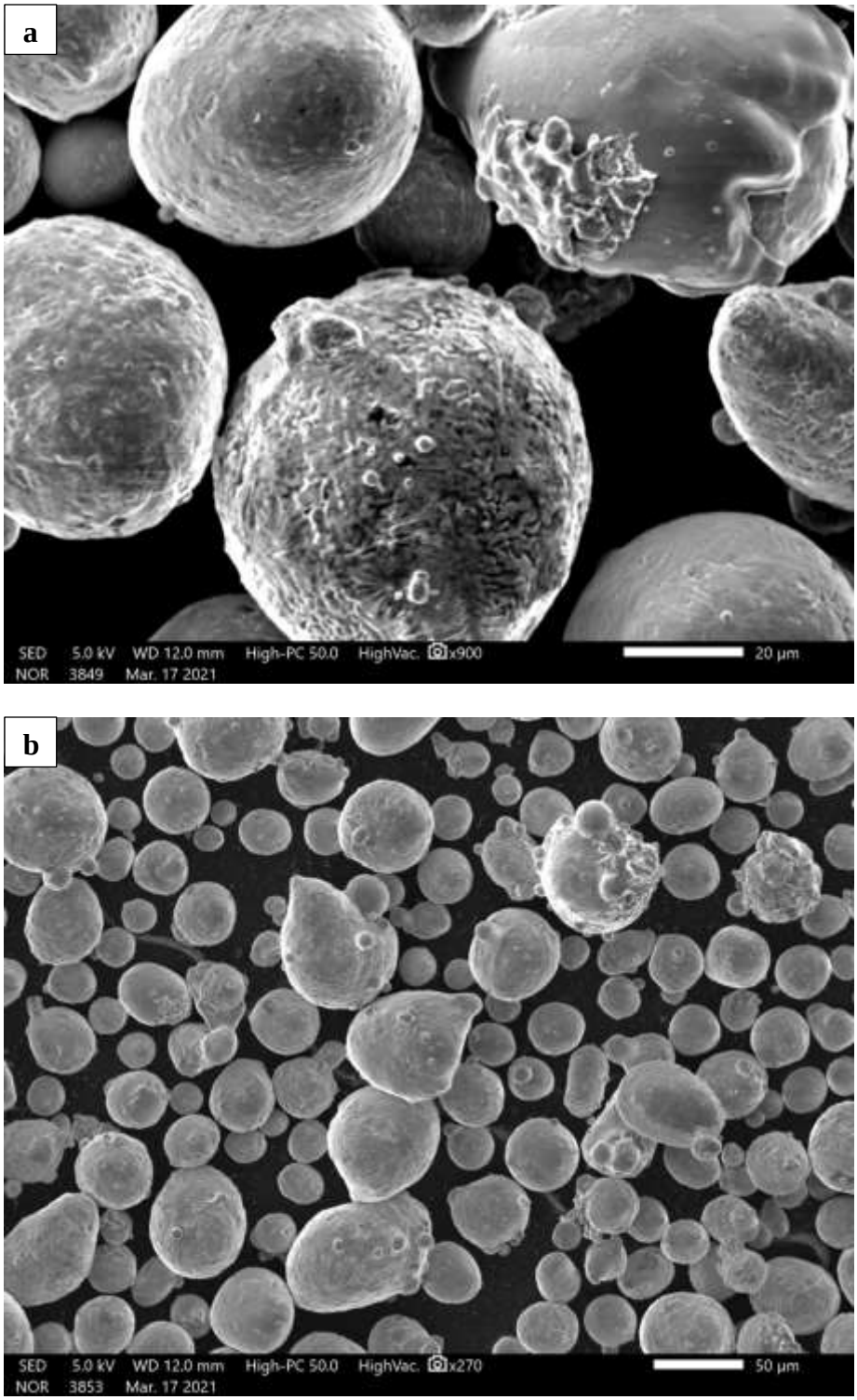


Figure 11. F357 Aluminum powder SEM images (EOS) a) High magnification b) Low magnification

A metallography analysis of the powder interior reveals a micro-dentritic Al structure with secondary arm spacing of approximately 0.8 microns with minimal porosity, as shown in Figure 12.

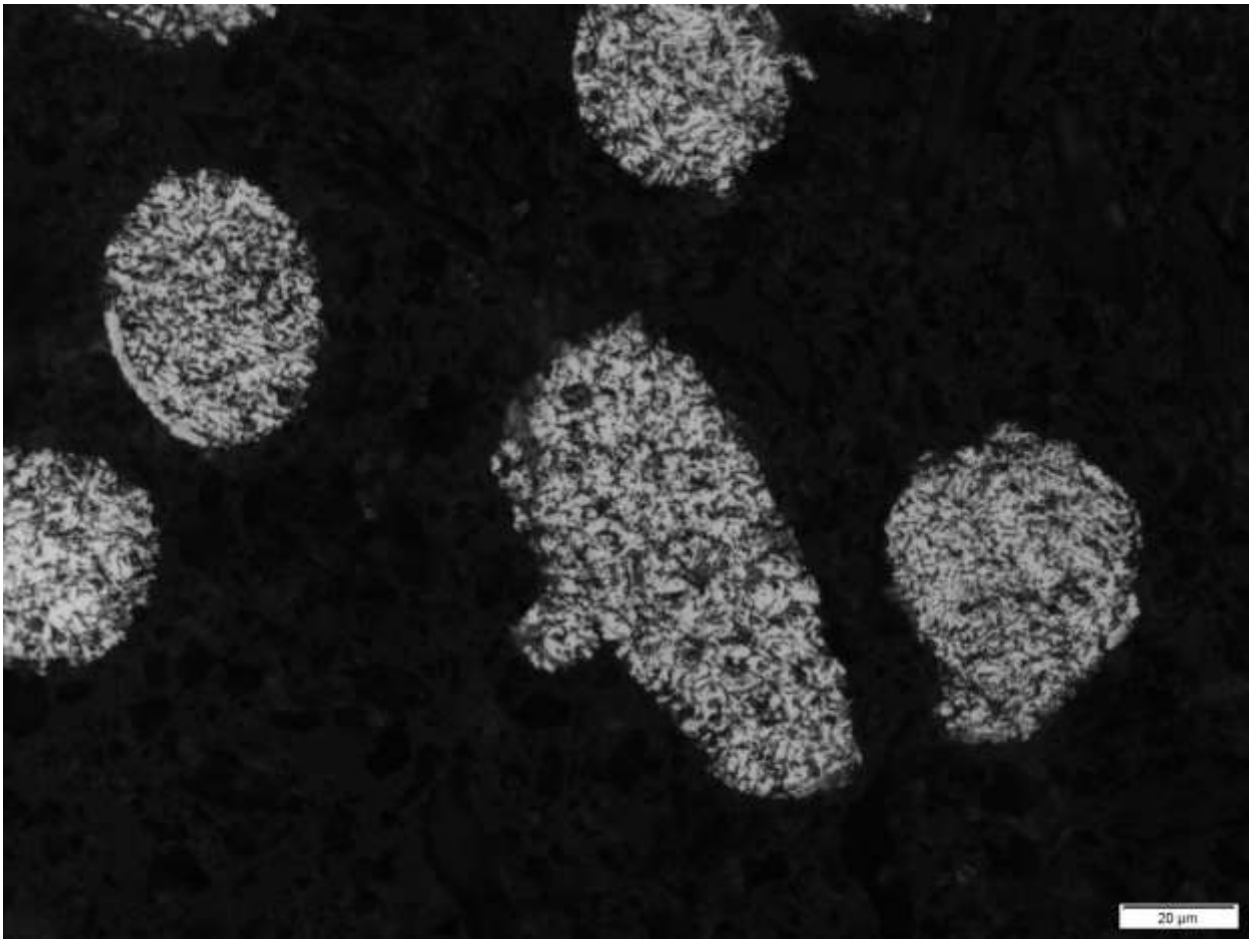


Figure 12. Powder Microstructure

## 3.2 Laser Powder Bed Fusion Systems

The two printers used for this project were the EOS M290 and SLM 280, two Laser Powder Bed Fusion systems that have been adjusted with their corresponding optimal parameters based on the parameters developed.

The EOS M290 Direct Metal Laser Sintering (DMLS) machine has a construction volume of 250 x 250 x 325 mm (9.85 x 9.85 x 12.8 in), including the build plate [80], with a ytterbium-fiber laser [75] of 400 W, a scan speed up to 7.0 m/s and a focus diameter of 100 μm (0.004 in) approximately. Figure 13 illustrates the composition of the EOS M 290 printer.


Figure 13. Laser Powder Bed Fusion-EOS M290 printer*[81]*

SLM 280 printer has a construction volume are of 280 x 280 x 365 mm (11.02 x 11.02 x 14.4 in) [82], with a multi-beam (single or twin) laser of 400 W or 700 W IPG fiber laser, with a maximum scan speed of 10 m/s and an adjustable focus diameter from 80µm – 115µm. Figure 14 illustrates the SLM 280 printer machine used for this project.


Figure 14. Laser Powder Bed Fusion-SLM 280 printer*[83]*

## 3.3 Parameters Development

A first pre-test job build is performed to validate the machine setup and different process parameters; after that, a scan speed with variations on the parameters is performed [84]. In the SLM 280, 24 cubes with dimensions of 15x15x15 mm^3 are placed at the right and left of the build plate, also 15 bigger cubes are placed in the middle of the build plate, just to have a higher exposure area and a more realistic job [85]. In Figure 15, a build job overview of the process is shown, with the 24 cubes at the left and right edge, with the 15 bigger cubes at the center.

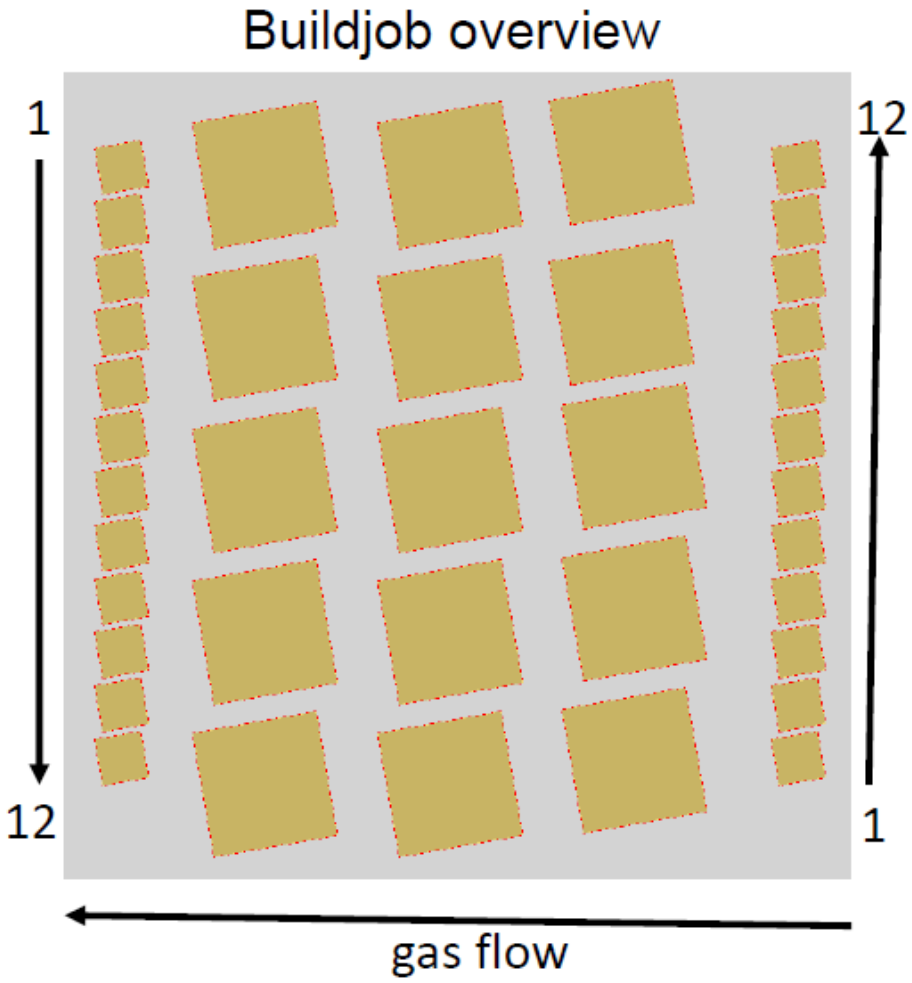


Figure 15. Buildjob Overview for the SLM validation

For this validation process pre-test job, the settings of the machine were the following:

- Layer thickness: 30 µm, Laser power: 370 W
- Preheating temp. 150°C
- Gas flow speed: 22 mm/s
- Process gas: argon
- For the small cubes (15x15x15 $mm^3$), the scan speed was varied from 1200 mm/s to 1470 mm/s, detailed overview on Table 2, the big baffler was built with a fixed parameter (scan speed of 1200 mm/s, laser power 370 W, hatch distance 0,1 mm)
- All cubes were built with one laser.

Table 2. Combination of printing parameters with corresponding densities (SLM)

| Cube | Laser power (W) | Scan Speed (mm/s) | Density (%) |
|---|---|---|---|
| 1 | 370 | 1200 | 99.93 |
| 2 | 370 | 1225 | 99.92 |
| 3 | 370 | 1250 | 99.92 |
| 4 | 370 | 1275 | 99.91 |
| 5 | 370 | 1300 | 99.90 |
| 6 | 370 | 1325 | 99.88 |
| 7 | 370 | 1350 | 99.89 |
| 8 | 370 | 1375 | 99.86 |
| 9 | 370 | 1400 | 99.84 |
| 10 | 370 | 1425 | 99.85 |
| 11 | 370 | 1450 | 99.85 |
| 12 | 370 | 1475 | 99.79 |

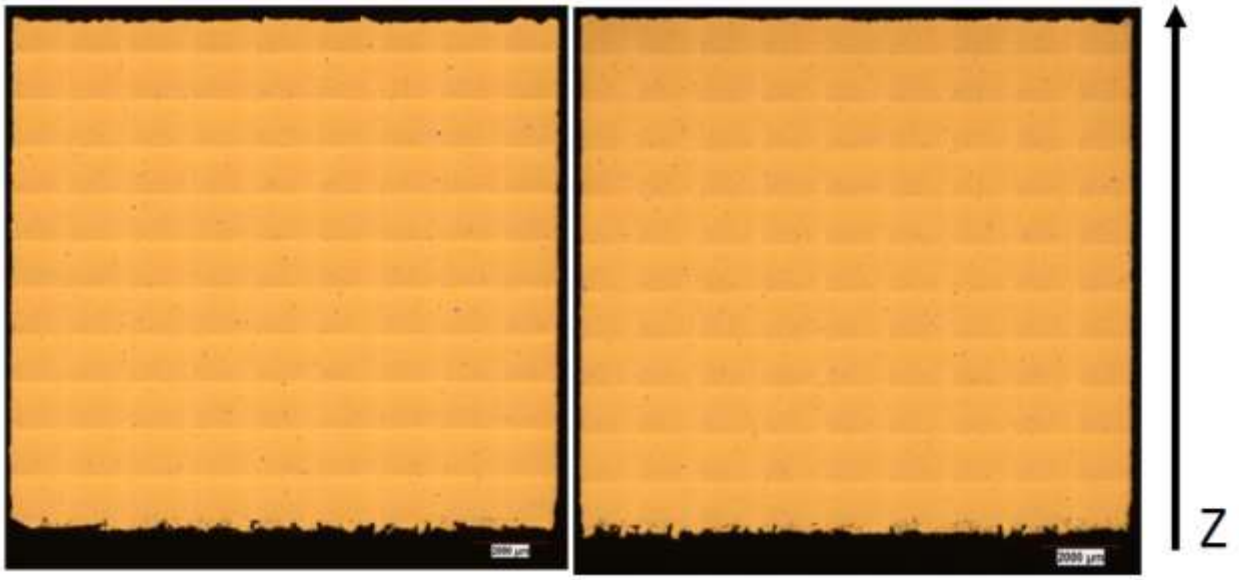


Figure 16. Microstructure as polished variant with >99.9% on relative density

For the EOS M290 building, a parameter development was also performed to determine the best parameter strategy for this printing; ten cubes were printed over the building plate, each with a different parameter combination between laser power and scan speed, everything with the goal of performing the build with the highest material density. The parameters and results of each variant are shown in Table 3.

Table 3. Combination of printing parameters with corresponding densities (EOS)

| Cube | Scan speed (mm/s) | Laser power (W) | Hatch (mm) | LT (µm) | Stripe (mm) | e (J/mm3) | Density g/cc | Density % |
|---|---|---|---|---|---|---|---|---|
| #1 | 1300 | 360 | 0.13 | 30 | 7 | 71.0 | **2.672** | 99.701% |
| #2 | **1325** | 370 | 0.13 | 30 | 7 | 71.6 | **2.6725** | 99.720% |
| #3 | **1270** | 365 | 0.13 | 30 | 7 | 73.7 | 2.669 | 99.590% |
| #4 | 1285 | **365** | 0.13 | 30 | 7 | 72.8 | 2.6704 | 99.642% |
| *#5 | 1300 | **365** | 0.13 | 30 | 7 | 72.0 | 2.6686 | 99.575% |
| #6 | 1315 | **365** | 0.13 | 30 | 7 | 71.2 | 2.671 | 99.664% |
| #7 | 1160 | 370 | 0.17 | 30 | 7 | 62.5 | 2.6703 | 99.638% |
| #8 | **1175** | 370 | 0.17 | 30 | 7 | 61.7 | 2.6686 | 99.575% |
| *#9 | **1200** | 370 | 0.17 | 30 | 7 | 60.5 | 2.6708 | 99.657% |
| #10 | 1225 | **370** | 0.17 | 30 | 7 | 59.2 | 2.6698 | 99.619% |

After the build, the little cubes will be removed from the build plate and sectioned to determine the density with an Accupyc II 1340 Pycnometer (Norcross, United States)[86] with the helium gas displacement method. Figure 17 are shown the cubes on the build plate. The next step was to do metallography work on the cubes to have a visible porosity overview; mounting and polishing work was performed on the samples; Figure 18 shows the pictures of the porosity on the sample with the best possible density result; a microscope was used to evaluate the microstructure over the sample.

Figure 17. Variant cubes from 1 -10 parameters combination

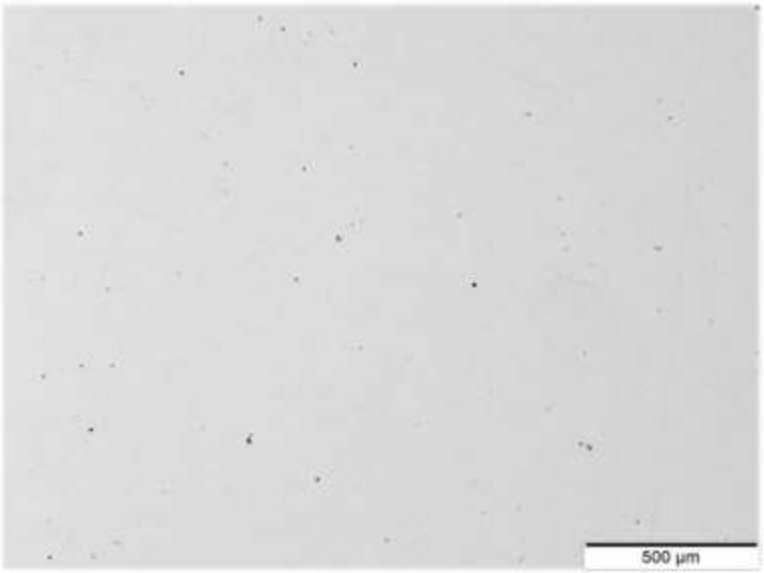


Figure 18. Micrograph of as-polished sample with highest density %

## 3.4 Process Parameters, Setup and Printing

To produce the tensile specimens on the EOS M290, a total of 130 vertical and 130 horizontal specimens were printed. The parameters selected from the process development were the following, the specimens were printed on a build plate preheated at 80° C, a scanning speed of 1300 m/s and a laser power set to 370 W, a hatch distance of 0.13 mm with a layer thickness of 30 μm. With a height of 80mm and 14mm in diameter for each cylinder, the bars had dimensions of 14 x 71 x 77 mm, where each bar was divided into six separate bars. A total of 3 prints were performed to print the 260 samples for the EOS M290 printer. Figures 19 to 21 show the distribution of the sample on the build plate. Additionally, Figure 22 shows a picture of the printed parts attached to the building plate.

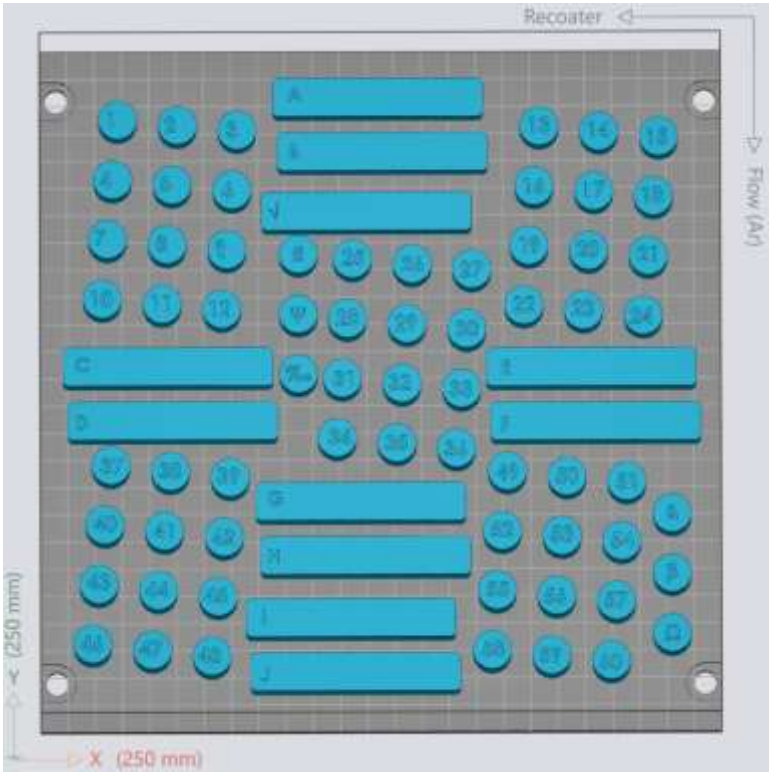


Figure 19. First print layout (EOS)

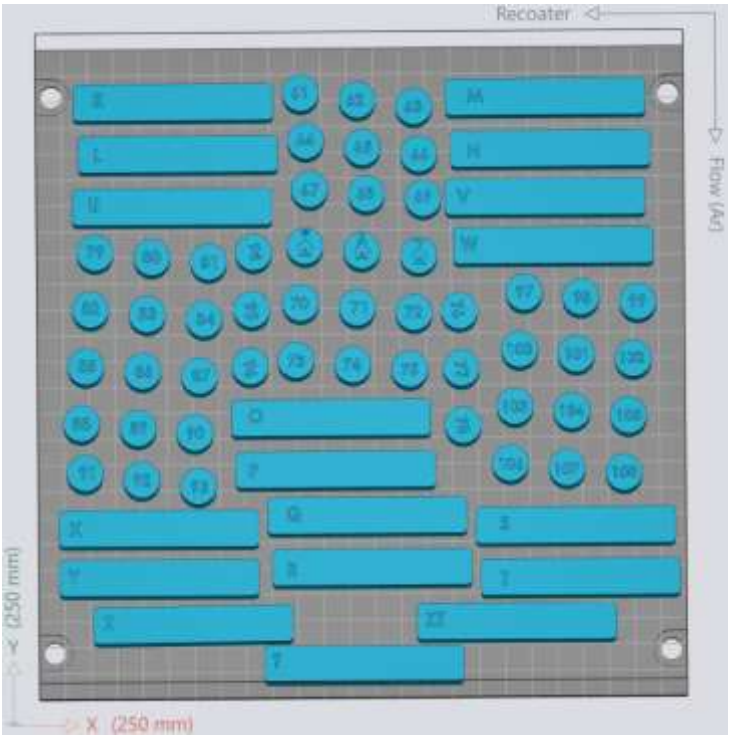


Figure 20. Second print layout (EOS)

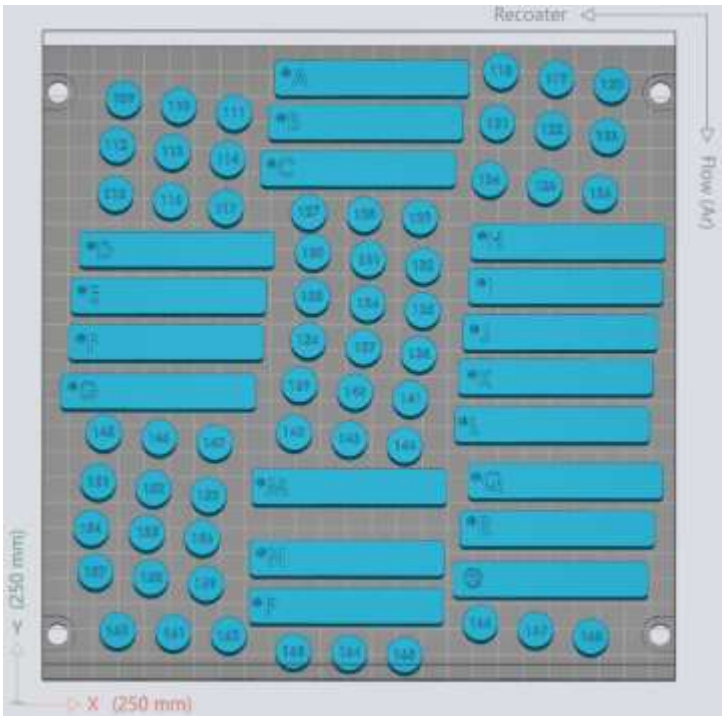


Figure 21. Third print layout (EOS)

Figure 22. Second print layout printed over the plate (EOS)

For the SLM 280 printer, a total of 124 vertical cylinders and 13 horizontal bars specimens were printed. From the parameter's development, the parameters selected were a laser power of 370 W and a scan speed of 1200 mm/s with a layer thickness the same as the EOS print, 30 μm. With a height of 320mm and 15mm in diameter for the vertical cylinders, three cylinders were obtained from each large cylinder. 2 lasers were used for the center part, as you can see in Figure 23, the red zone used optic 1 and 2, above the red area, optic two was used, and below the red zone, optic one was used for the printing. The bars had dimensions of 55 x 16 x 320 mm, and each bar was divided into eight separate bars. Same as the cylinders, the red zone used optics 1 and 2; above the red zone, optic two was used, and below the red area, optic one was used. Figures 23 o 24 show the distribution of the specimens on the build plate; additionally, Figures 25 to 26 show the printed parts attached to the build plate.

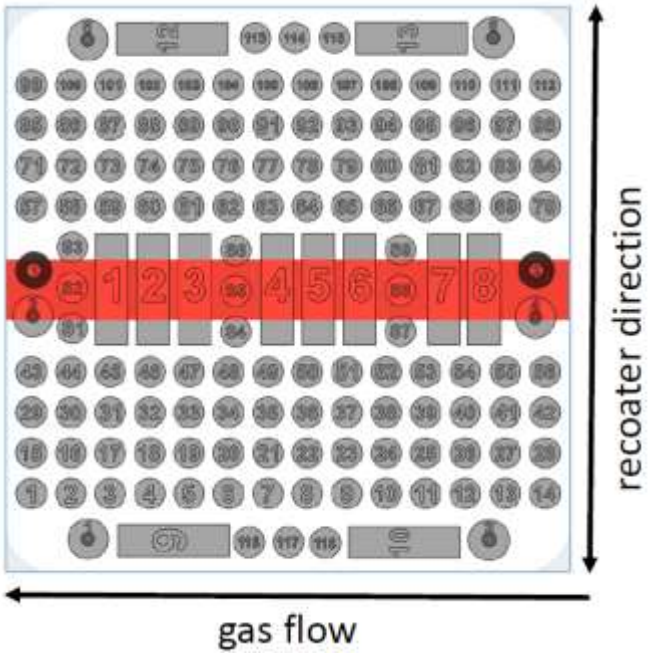


Figure 23. SLM print layout (top view)

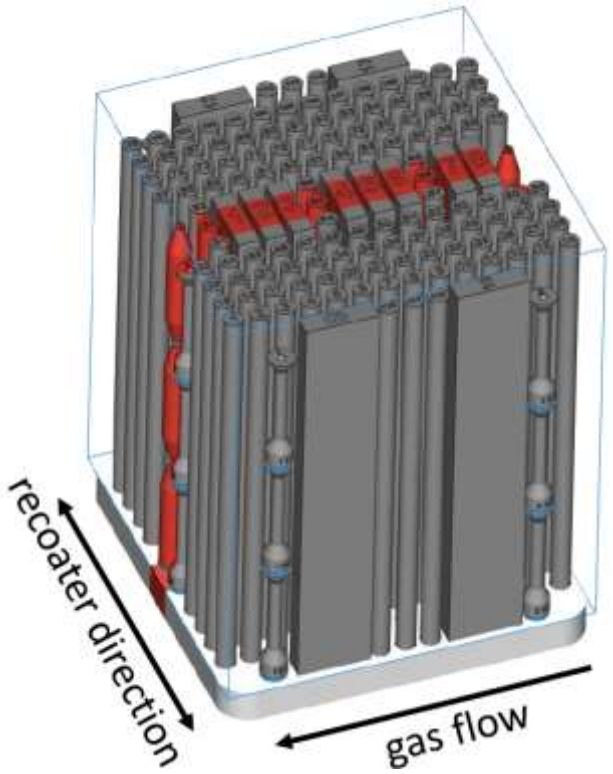


Figure 24. SLM print layout (front-to-side view)

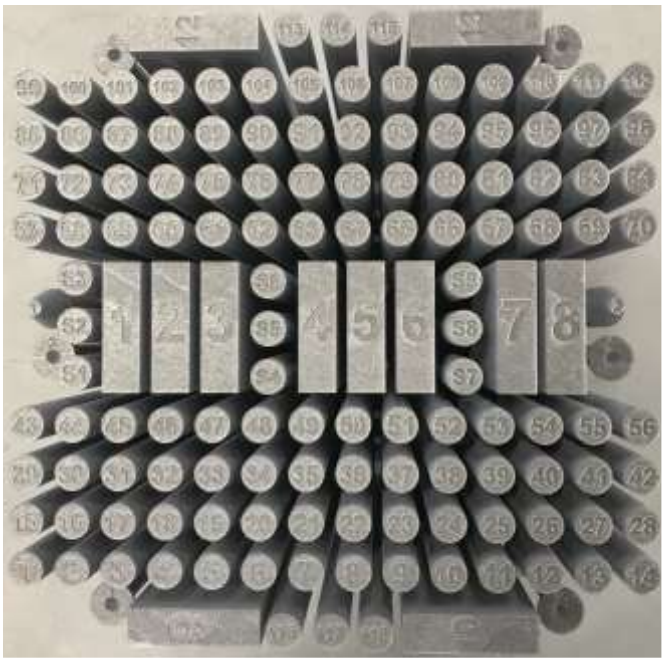

Figure 25. SLM printed parts on the build plate (top view)

Figure 26. SLM printed parts on the build plate (front-side view)

## 3.5 Sampling

After printing and retire the specimens from the build plate, rods and bars were sampled and sorted randomly form build jobs into different categories, these categories with the number of samples are specified in Figure 27.

| Test Matrix F357 EOS M290 / SLM 280 | | Hours at 285°F | | | | | |
|---|---|---|---|---|---|---|---|
| | | 0 | | 100 | | 1000 | |
| | | XY | Z | XY | Z | XY | Z |
| Post Process | As Built | 4/4 | 4/4 | 4/4 | 4/4 | 4/4 | 4/4 |
| | *T6 | 6/6 | 6/6 | 6/6 | 6/6 | 6/6 | 6/6 |
| | HIP | 4/4 | 4/4 | 4/4 | 4/4 | 4/4 | 4/4 |
| | *HIP+ T6 | 6/6 | 6/6 | 6/6 | 6/6 | 6/6 | 6/6 |
| | *SR1 | 6/6 | 6/6 | 6/6 | 6/6 | 6/6 | 6/6 |

| Test Matrix F357 EOS M290 / SLM 280 | | Hours at 350°F | | | | | |
|---|---|---|---|---|---|---|---|
| | | 0 | | 100 | | 1000 | |
| | | XY | Z | XY | Z | XY | Z |
| Post Process | As Built | same from 285° | same from 285° | 4/4 | 4/4 | 4/4 | 4/4 |
| | *T6 | same from 285° | same from 285° | 6/6 | 6/6 | 6/6 | 6/6 |
| | HIP | same from 285° | same from 285° | 4/4 | 4/4 | 4/4 | 4/4 |
| | *HIP+ T6 | same from 285° | same from 285° | 6/6 | 6/6 | 6/6 | 6/6 |
| | *SR1 | same from 285° | same from 285° | 6/6 | 6/6 | 6/6 | 6/6 |

Figure 27. F357 General Matrix

Every single specimen is individually tracked and sorted on individual aluminum containers, shown in Figure 28 the rod (vertical) ID's start with a number, in other hand, the bar (horizontal) ID's start with a letter.

Figure 28. Aluminum containers to divide into categories.

## 3.6 Heat Treatment and Aging Parameters

There is currently no ASTM standard for heat-treating additively manufactured aluminum F357; however, ASTM F3318 [87] standard was followed in this F357 study. Studies have shown the modification of microstructure and of the mechanical properties at room temperature (25 °C) of laser powder bed fusion aluminum F357 parts involve a variety of post-process heat treatments. In this work, the following heat treatments were applied to the F357: NHT condition (no heat treatment required), stress relief (SR) anneals at 285 °C held for 120 min (±15 min) and cooled at a rate equal to air cooling or faster, T6 condition held at 530 °C for 360 min, then quenched in water or glycol and aged at 160 °C for 360 min and hot isostatic pressing condition (HIP) under an inert atmosphere at 100 MPa, ~515 °C and HIP + T6 condition.

In addition, since it is of interest to know the performance of the F357 under service conditions, artificial thermal aging was held on some of the specimens to observe the changes in microstructure and mechanical properties. The aging was divided into two different temperatures, 140.5 °C and 177 °C, and three different aging times were selected (0 h, 100 h, and 1000 h). The resulting microstructures were characterized by optical metallography and associated mechanical

properties, including room temperature tensile tests and Vickers micro-indentation hardness measurements.

Heat treatments consist of the use of temperature and time at temperature to modify the properties of a material, in this case, printed aluminum F357. The schedules of the heat treatments consist of the aging of as-built F357 samples, one stress relief treatment (SR1), HIP, T6, and HIP+T6 treatments of the printed samples. ASTM F3318 was used for heat treatment standards shown below:

Heat treatments:

- SR1: 285°C (±14°C) for 120 min (±15 min), air cooled
- HIP: 100MPa, 515°C (±14°C) for 180 min, inert atmosphere cooled
- T6: 530°C (±6°C) for 360 min, quenched in water, aged 160°C (±6°C) for 360 min
- HIP + T6: HIP, followed by T6 processing

Aging:

- Times: 0hr, 100hr, 1000hr.
- Temperatures: 140°C and 177°C.

## 3.7 Different Variants

Knowing that five heat treatments and five different aging conditions were applied to the specimens, A total of 100 experimental variants were created with these two orientations, times, and temperatures, as listed in Table 4 and Table 5 below for each of the LPBF systems utilized in this study.

Table 4. Heat treatment matrix. Note each orientation (XY and Z) contains 50 samples each

| Variant | Heat Treatment | Aging (Hours and Temperature) | Printer |
|---|---|---|---|
| 1 | None | 0hr | EOS |
| 2 | None | 100hr 140°C | EOS |
| 3 | None | 1000hr 140°C | EOS |
| 4 | None | 100hr 177°C | EOS |
| 5 | None | 1000hr 177°C | EOS |
| 6 | SR | 0hr | EOS |
| 7 | SR | 100hr 140°C | EOS |
| 8 | SR | 1000hr 140°C | EOS |
| 9 | SR | 100hr 177°C | EOS |
| 10 | SR | 1000hr 177°C | EOS |
| 11 | HIP | 0hr | EOS |
| 12 | HIP | 100hr 140°C | EOS |
| 13 | HIP | 1000hr 140°C | EOS |
| 14 | HIP | 100hr 177°C | EOS |
| 15 | HIP | 1000hr 177°C | EOS |
| 16 | T6 | 0hr | EOS |
| 17 | T6 | 100hr 140°C | EOS |
| 18 | T6 | 1000hr 140°C | EOS |
| 19 | T6 | 100hr 177°C | EOS |
| 20 | T6 | 1000hr 177°C | EOS |
| 21 | HIP+T6 | 0hr | EOS |
| 22 | HIP+T6 | 100hr 140°C | EOS |
| 23 | HIP+T6 | 1000hr 140°C | EOS |
| 24 | HIP+T6 | 100hr 177°C | EOS |
| 25 | HIP+T6 | 1000hr 177°C | EOS |
| 26 | None | 0hr | SLM |

| | | | |
|---|---|---|---|
| 27 | None | 100hr 140°C | SLM |
| 28 | None | 1000hr 140°C | SLM |
| 29 | None | 100hr 177°C | SLM |
| 30 | None | 1000hr 177°C | SLM |
| 31 | SR | 0hr | SLM |
| 32 | SR | 100hr 140°C | SLM |
| 33 | SR | 1000hr 140°C | SLM |
| 34 | SR | 100hr 177°C | SLM |
| 35 | SR | 1000hr 177°C | SLM |
| 36 | HIP | 0hr | SLM |
| 37 | HIP | 100hr 140°C | SLM |
| 38 | HIP | 1000hr 140°C | SLM |
| 39 | HIP | 100hr 177°C | SLM |
| 40 | HIP | 1000hr 177°C | SLM |
| 41 | T6 | 0hr | SLM |
| 42 | T6 | 100hr 140°C | SLM |
| 43 | T6 | 1000hr 140°C | SLM |
| 44 | T6 | 100hr 177°C | SLM |
| 45 | T6 | 1000hr 177°C | SLM |
| 46 | HIP+T6 | 0hr | SLM |
| 47 | HIP+T6 | 100hr 140°C | SLM |
| 48 | HIP+T6 | 1000hr 140°C | SLM |
| 49 | HIP+T6 | 100hr 177°C | SLM |
| 50 | HIP+T6 | 1000hr 177°C | SLM |

Table 5.Heat treatment parameters

| Material Process | Pressure (psi) | Temperature (°C) | Hold Time (min) | Cooling Method |
|---|---|---|---|---|
| SR | None | 285 | 120 | Air |
| HIP | 14,500 | 515 | 180 | Air |
| T6 (Annealing) | None | 530 | 360 | Quench |
| T6 (Aging) | None | 160 | 360 | Air |
| HIP+T6 | HIP shall be followed by T6 processing | | | |

Aging was monitored with external type K thermocouples and recorded by two independent automatic data loggers every 30min to ensure the temperature continued constant at 140°C and 177°C for the 100 and 1000 hours.

## 3.8 Machining and Mechanical Testing

Tensile testing was performed on all samples using an MTS Landmark [88] (Eden Praire, US) servo-hydraulic system, which has a force capacity of 100 kN. The system is equipped with threaded grips where the specimens are placed. In addition, an MTS 25.4mm axial clip extensometer is used, as shown in Figure 2. All samples are machined following ASTM E8 standard guidelines. The speed of testing was controlled by a crosshead displacement speed of 0.476 mm/min. The mechanical properties results shown in this work are the average of samples composed of either 4 or 6 specimens per each condition and per each orientation, as is shown in Figure 30. The mechanical properties of each specimen were calculated from its individual stress-strain diagram. Yield stress measurements involved a 0.2 % strain offset. The As-built and HIP conditions have four specimens per sample, and T6, HIP+T6, and SR1 have six specimens per sample.

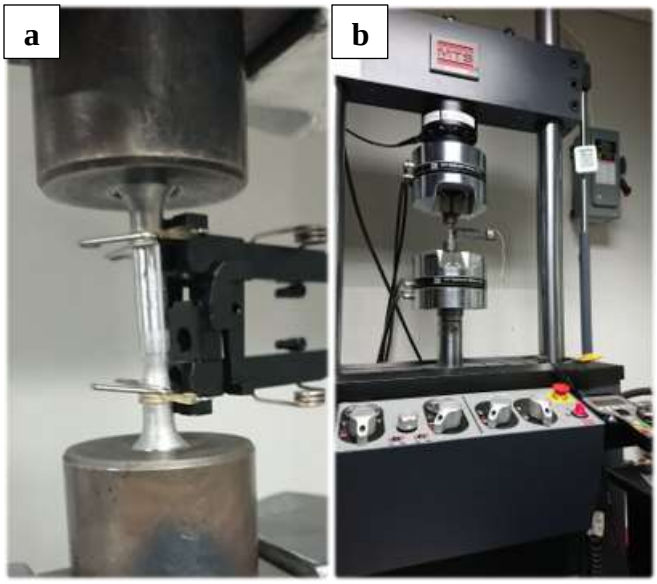


Figure 29. a) Tensile test performing sample, b) MTS Landmark servo-hydraulic system

## 3.9 Density Measurement

Density measurements were obtained through the helium gas displacement method with an Accupyc II 1340 Pycnometer [89] (Norcross, United States). The pycnometer performs ten measurements for each experimental variant. Mass measurements are obtained using a Sartorius CP124S weight balance (Sartorius AG, Germany). Density was then calculated with the resulting mass and volume measurements.

## 3.10 Microstructure Characterization

After the tensile test was performed, the fracture surfaces were protected, and the threaded part of the specimen was sectioned into three different planes: Y-Z, X-Z, and X-Y planes. Once sectioned, an ATM OPAL 460 [90] (Haan, Germany) hot mounting press was used to create metallographic samples out of phenolic powder and back epoxy. Once mounted, the samples were ground and polished with an ATM SAPHIR 530 semi-automatic system [91].

The sample preparation started with the grinding of samples with silicon carbide grinding papers of 320 grit at 300 rpm with 25 N of force, and after 1 min of grinding, the paper was changed to 800 grit paper, using the same presets, and using continuous water while the machine was running. The samples were then moved to an abrasive diamond disc and ground with a nine μm diamond suspension at 150 rpm with 25 N of force for 3:30 min. Once this step was finished, the samples were polished using a woven white wool cloth with a three μm diamond suspension at 150 rpm with 20 N of force for 5 min. Samples were finally polished using 0.2 μm fumed silica at 150 rpm with 15 N of force for 10 min.

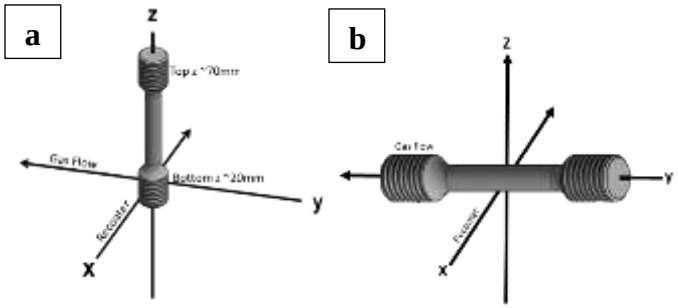


Figure 30. Machined tensile sample orientation a) Z orientation, b) XY orientation

## 3.11 Etching

The microstructure was revealed using Keller's etchant. This etchant consisted of 5 mL of Nitric Acid, 3 mL of Hydrochloric Acid, 2 mL of Hydrofluoric Acid, and 190 mL of Distilled Water. The submersion method was used for a range of 36 s to 39 s. All optical micrographs were taken on an Olympus GX53 [92] (Olympus Inc., Tokyo, Japan) inverted optical microscope.

## 3.12 Hardness Testing

Hardness testing was performed on a Qatm - Qness 30 CHD Master+ [93] using Vickers (HV) scale. Measurements were taken from X, Y and Z plane, from samples printed in vertical (Z)

direction. The load used for the measurement was 100gf, five indentations separated by at least three millimeters were performed on the surface for each sample.

# CHAPTER 4: RESULTS AND DISCUSSION

## 4.1 Microstructure Analysis

The current study compares the spectrum of microstructures and corresponding mechanical property data for AlSi7Mg alloy for the EOS system and in the SLM 280HL LPBF system. The full spectrum of mechanical properties data measured for each LPBF system included tensile and micro indentation hardness (HV) for components fabricated in both the Z-direction (parallel to the build direction) and the XY-direction (perpendicular to the build direction). Taken together with four post-process heat treatments: stress relief (SR1), HIP, T6, and HIP + T6, as well as aging treatments for 100 h and 1000 h each at 140 °C and 177 °C, respectively, resulted in 100 variants (Tables 4 and 5). This resulted in a total of 520 measured tensile and HV data values, 260 for each LPBF system.

Figure 31, it is compared the light (optical) microscope images for unaged, Z-direction, as-built, SR1 treated, HIP, T6, and T6 + HIP treatment for EOS LPBF fabricated AlSi7Mg alloy components. Figure 31 displays the microstructure representation for each different condition (a-e), along with a corresponding stress-strain diagram (f). The initial microstructure (a) features 1-micron micro dendritic cells, which are slightly altered at the interlayer melt bands. This microstructure remains relatively unchanged after SR1 anneal at 285°C (b). Treating the components with T6 at 530°C, which is approximately 0.8 melting point (615°C), leads to complete recrystallization of the dendritic microstructures seen in (a) and (b), resulting in an average grain size of ~15 microns. This recrystallized grain structure contains mostly coarse, eutectic Si particles as large as 5 microns (c). Following HIP treatment at 515°C (d), the Si particles have a wider size distribution, and higher particle density, with a more globular shape and interparticle spacing of ~1 micron. The stress-strain diagram in (f) shows a decrease in yield

strength (YS) and ultimate tensile strength (UTS), with an increase in ductility (elongation) for the HIP treatment, in contrast to the as-built, SR, and T6 treated components. Similar results were observed in previous studies on LPBF fabrication and heat treatment of AlSi10Mg alloy [5], [94], [95]. Components treated with HIP + T6 (e) exhibit a coarse Si particle size smaller than the HIP Si particles seen in (c) as a result of the T6 treatment following the HIP treatment. The particle density and interparticle spacing are similar to those seen in (c) for the T6 treatment.

Examining Figures 32 and 33 in tandem provides useful insight, as they depict the as-built and heat-treated AlSi7Mg components from Figure 31 following aging for 100 hours and 1000 hours at 140°C, respectively. The microstructures of the components in Figures 32 and 33 are essentially the same and unchanged from those in Figure 31, except for the HIP + 1000-hour aging at 140°C (Figure 33 (d)), which has a denser distribution of Si particles. The stress-strain diagrams in Figures 32(f) and 33(f) also show the same extremes between the as-built, SR, and HIP-treated components as those in Figure 31(f). Interestingly, the alloy components processed by HIP and aged for both 100 hours and 1000 hours at 177°C exhibit very dense distributions of eutectic Si particles: Figures 34(d) and 35(d), respectively. The corresponding stress-strain diagrams in Figures 34(f) and 35(f) are similar to those in Figures 31(f) to 33(f), particularly for the HIP treatment. It is noteworthy that the eutectic Si particles in all cases are smaller, denser, and have a smaller interparticle spacing for HIP treatment than for either T6 or HIP + T6 treatments, as seen in Figures 31(d) to 35(d) compared to Figures 31 to 35(c) and (e). This is somewhat anomalous because smaller-spaced particles typically increase strength and decrease ductility (elongation), contrary to the HIP-related stress-strain diagrams, particularly when compared to those for the T6 and HIP + T6 treatment diagrams. However, in this case, the large and irregular Si particles in the T6 and HIP + T6 treated components behave differently and may mimic a duplex structure in

conjunction with the small grains (~ 12-15 microns, compared to 5-micron Si particles). This would lead to higher strength and lower ductility for the T6 and HIP + T6 components shown in the respective stress-strain diagrams [96]. It is noteworthy that this phenomenon was also observed in our prior study of LPBF-fabricated and heat-treated AlSi10Mg [95], which discussed other related complexities of precipitation hardening.

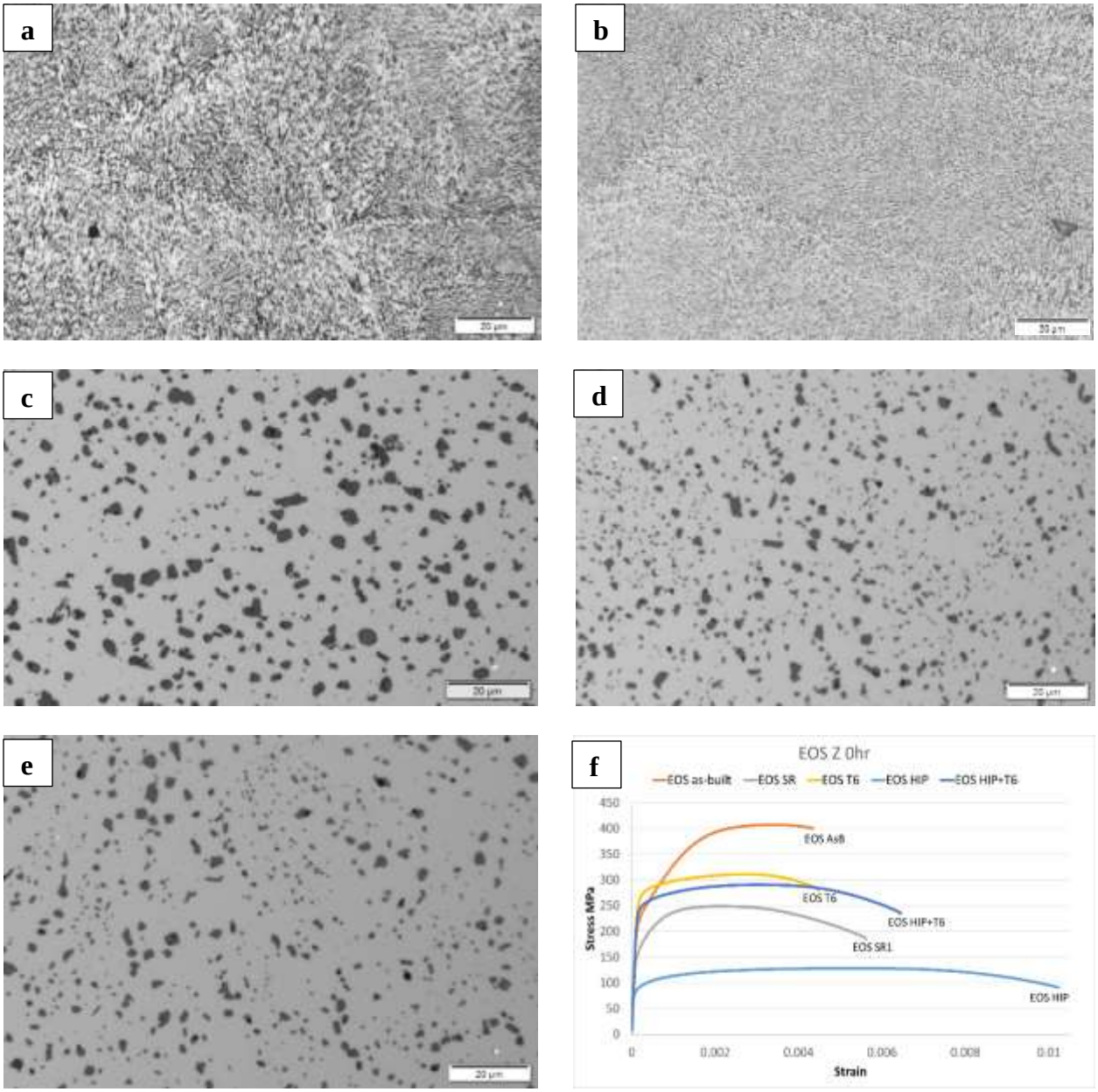


Figure 31. Microstructure images and corresponding stress-strain diagram for EOS F357 z-axis built and post process heat treatments with no aging. a) As built, b) SR c) T6, d) HIP, e) HIP+T6, f) Stress-strain diagram.

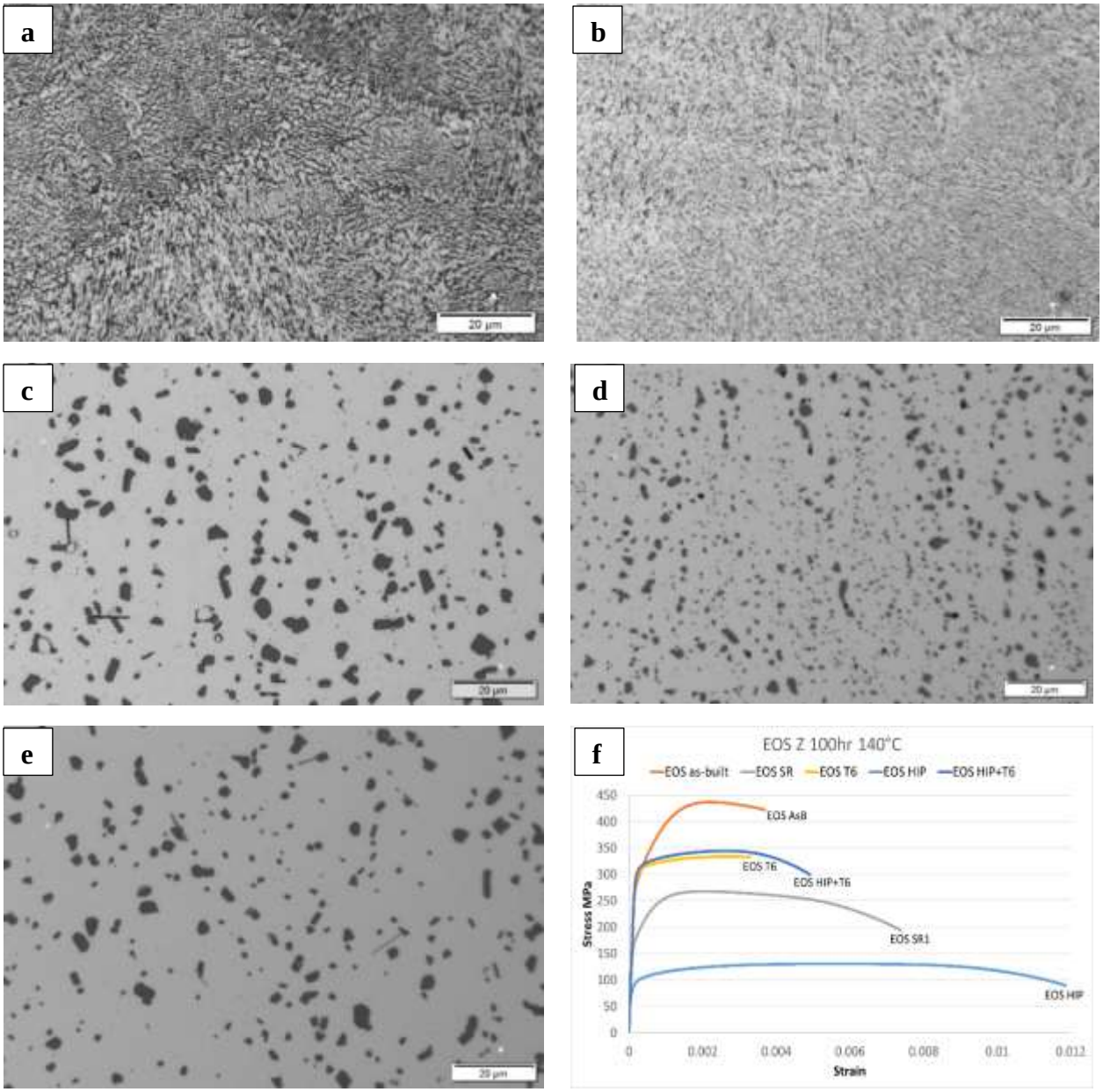


Figure 32. Microstructure images and corresponding stress-strain diagram for EOS F357 z-axis built and post process heat treatments aged for 100h at 140°C. a) As built, b) SR, c) T6, d) HIP, e) HIP+T6, f) Stress-strain diagram.

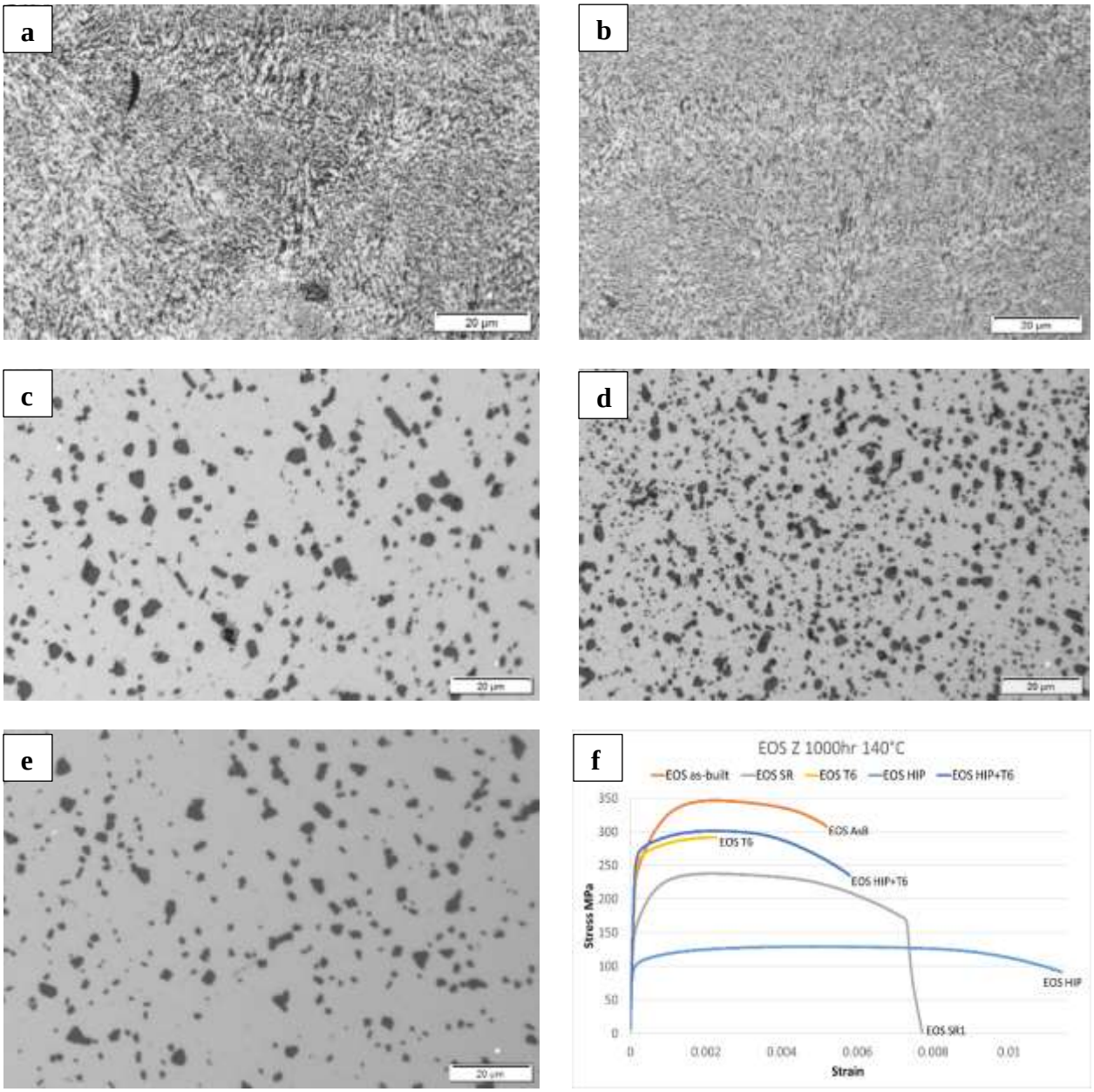


Figure 33. Microstructure images and corresponding stress-strain diagram for EOS F357 z-axis built and post process heat treatments aged for 1000h at 140°C. a) As built, b) SR c) T6, d) HIP, e) HIP+T6, f) Stress-strain diagram.

Figures 31 to 35 depict the range of microstructures and stress-strain properties observed for AlSi7Mg alloy components fabricated with the EOS system and subjected to different post-

processing heat treatments and aging treatments in the Z or build direction. Similar components fabricated in the XY direction exhibited the same microstructures and stress-strain diagrams. Furthermore, similar trends were observed for components fabricated using the SLM LPBF system in both the Z and XY directions. Figure 36 provides evidence for this observation by comparing the stress-strain diagrams of the EOS and SLM system components fabricated in both loading directions without aging. The trends in the stress-strain diagrams of Figure 36 are consistent with previous studies and show that the as-built components have the highest strength and lowest elongation to fracture, while the HIP components exhibit the lowest strength and highest elongation to fracture. The stress-strain diagrams of the EOS and SLM system components exhibit essentially the same trends.

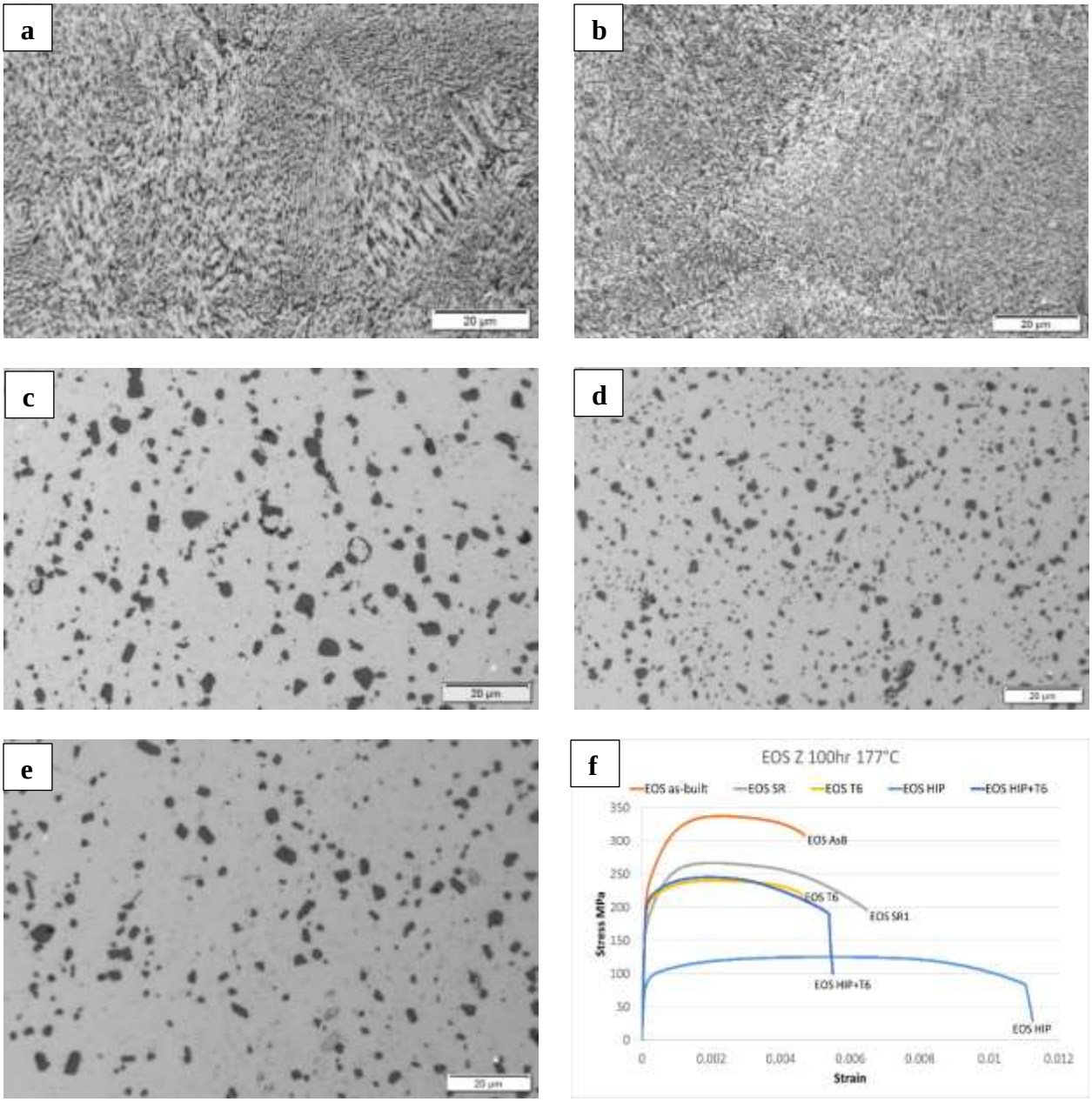


Figure 34. Microstructure images and corresponding stress-strain diagram for EOS F357 z-axis built and post process heat treatments aged for 100h at 177°C. a) As built, b) SR, c) T6, d) HIP, e) HIP+T6, f) Stress-strain diagram.

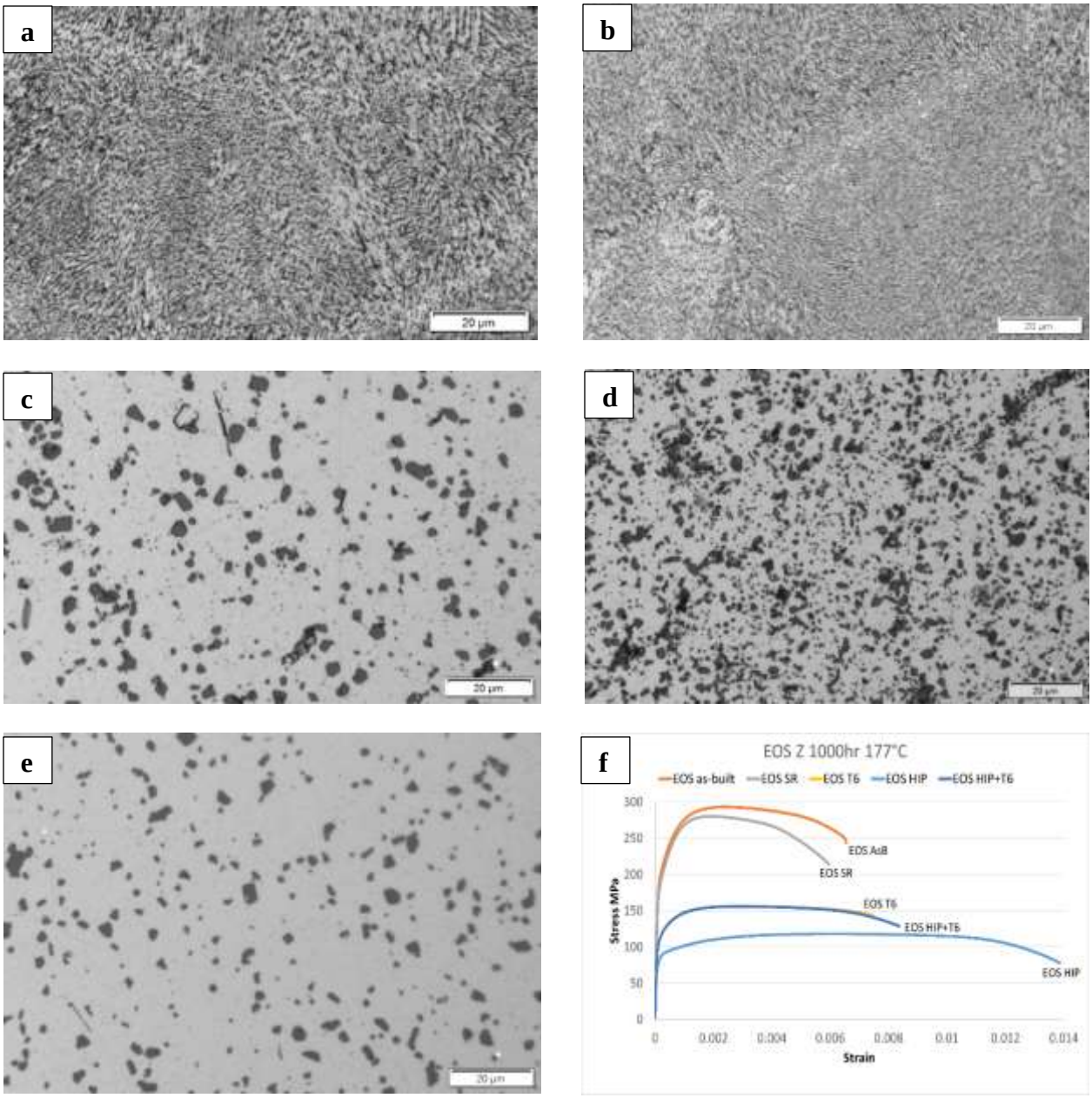


Figure 35. Microstructure images and corresponding stress-strain diagram for EOS F357 z-axis built and post process heat treatments aged for 1000h at 177°C. a) As built, b) SR, c) T6, d) HIP, e) HIP+T6, f) Stress-strain diagram.

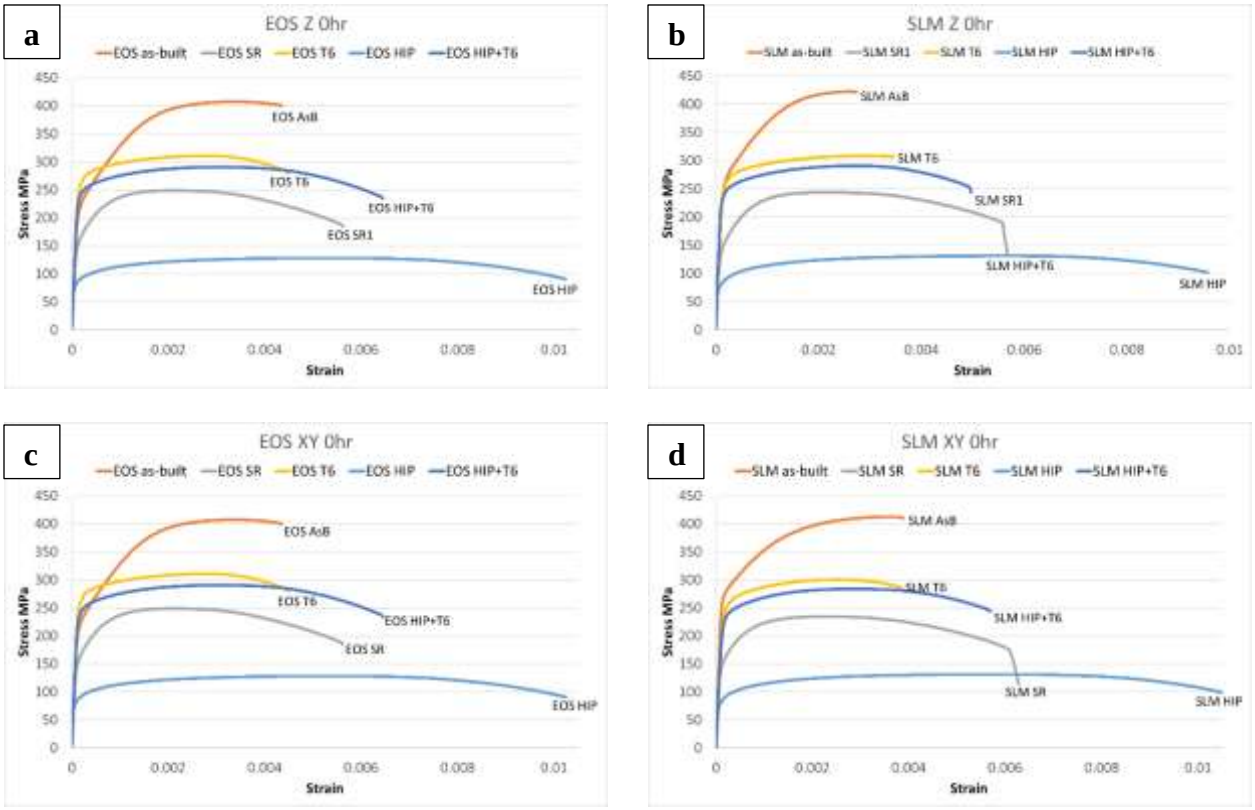


Figure 36. Characteristic curves for a) EOS printed parts in Z orientation, b) SLM printed parts in Z orientation, c) EOS printed parts in XY orientation and d) SLM printed parts in XY orientation.

Figure 37 and 38 illustrates comparisons of stress-strain diagrams between components fabricated using the EOS system and aged on the left-hand side of the figure (Figure 37 (a), (c) and Figure 38 (a), (c)), as well as corresponding components fabricated using the SLM system on the right-hand side of the figure (Figure 37 (b), (d), and Figure 38 (b), (d)). Despite some similarities in the trends of the stress-strain curves, there is a notable difference in their shapes. Specifically, the stress-strain curves for the SR-treated components in Fig 38 (a) and (c) for the EOS system and Figure 38 (b) and (d) for the SLM system, which represents tensile testing in the Z and XY directions, respectively, exhibit a steep decline in stress over a narrow strain window. This is indicative of rapid thermal softening or necking due to a rapid increase in void fraction,

which ultimately leads to failure. This phenomenon has been discussed in detail by Pineau, et al.[97] and Wcislik and Pala [98] for metal failure in general.

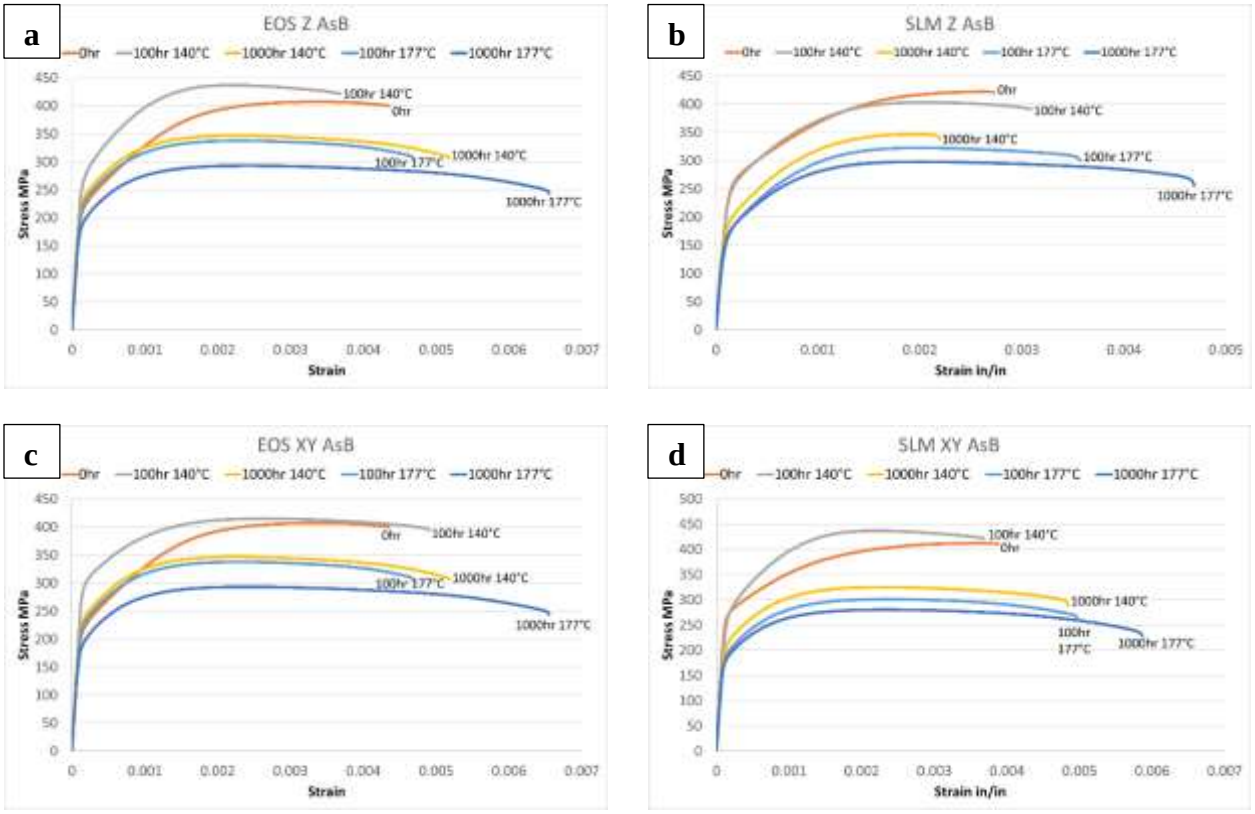


Figure 37. Characteristic curves for printed parts on a) EOS Z as built, b) SLM Z as built, c) EOS XY as built, d) SLM XY as built

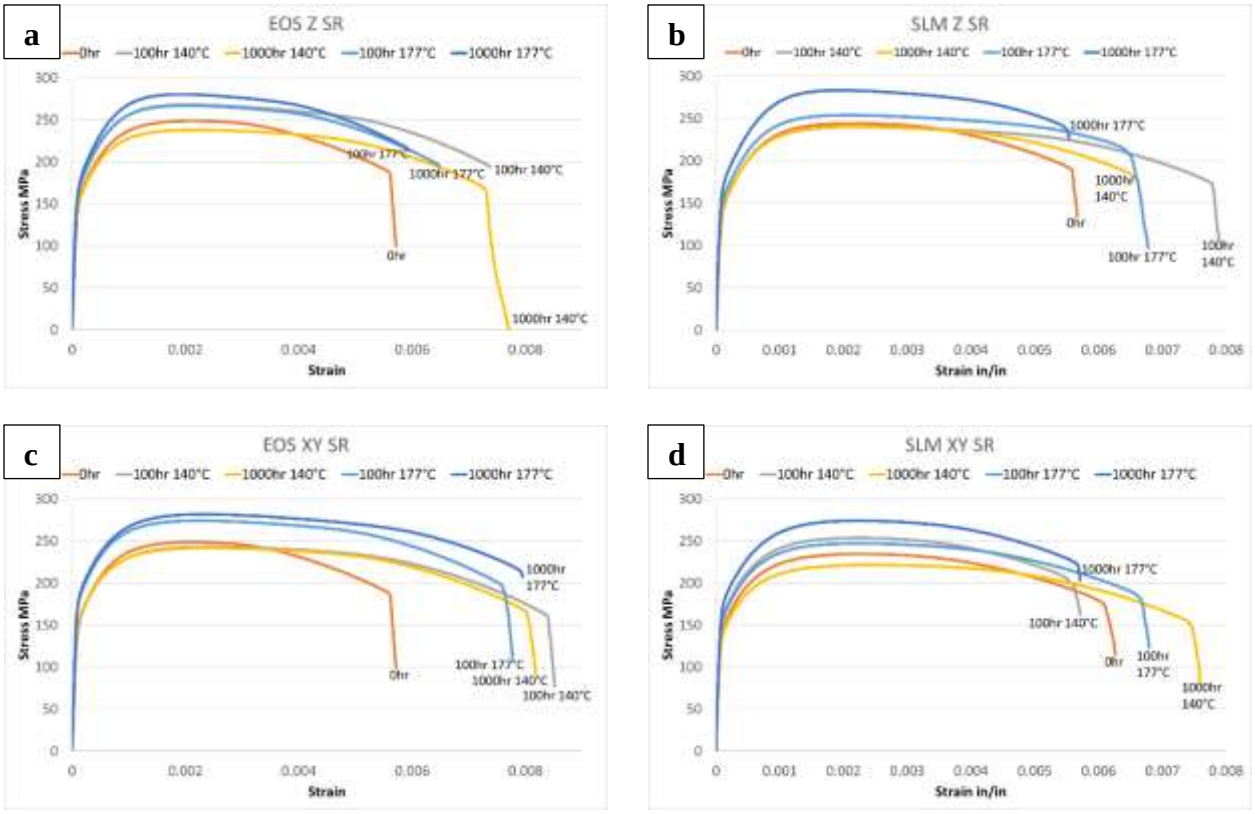


Figure 38.Characteristic curves for printed parts on a) EOS Z stress relief, b) SLM Z stress relief, c) EOS XY stress relief, d) SLM XY stress relief

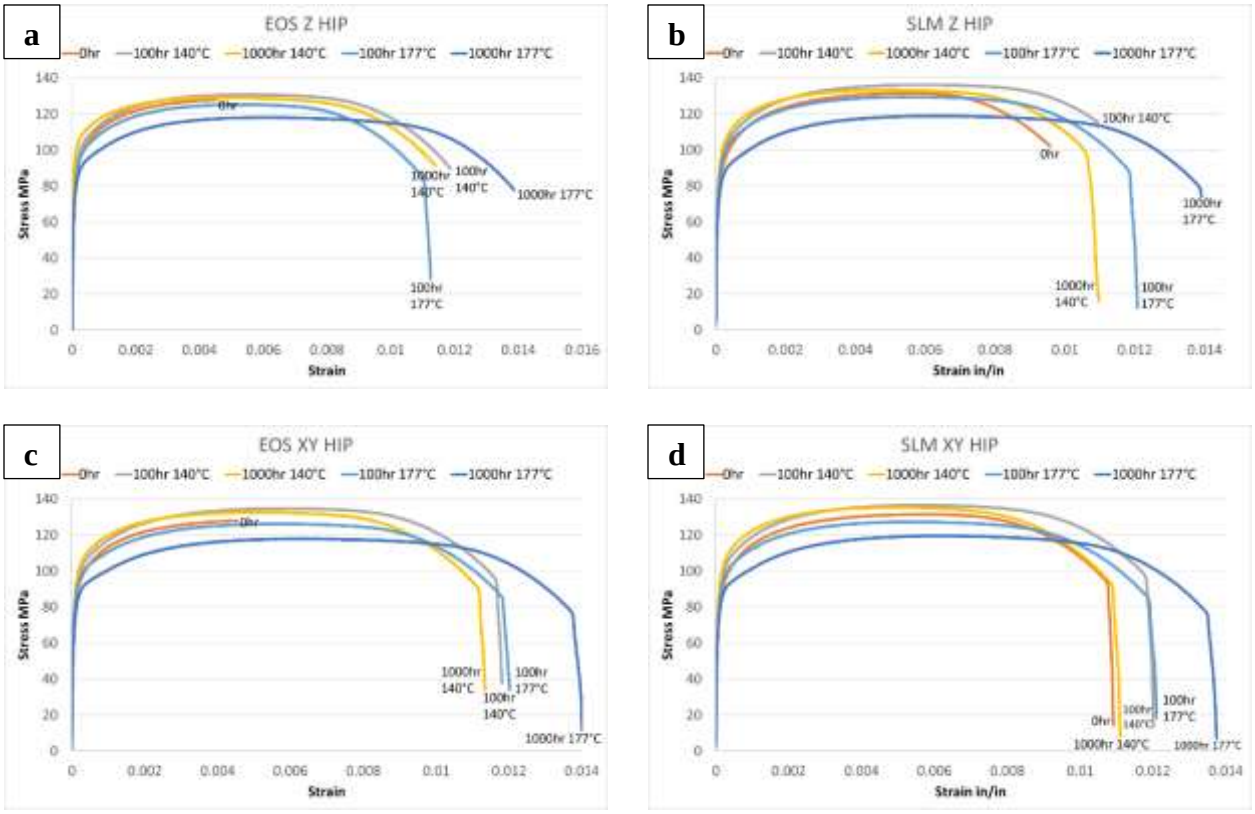


Figure 39. Characteristic curves for printed parts on a) EOS Z HIP, b) SLM Z HIP, c) EOS XY HIP, d) SLM XY HIP

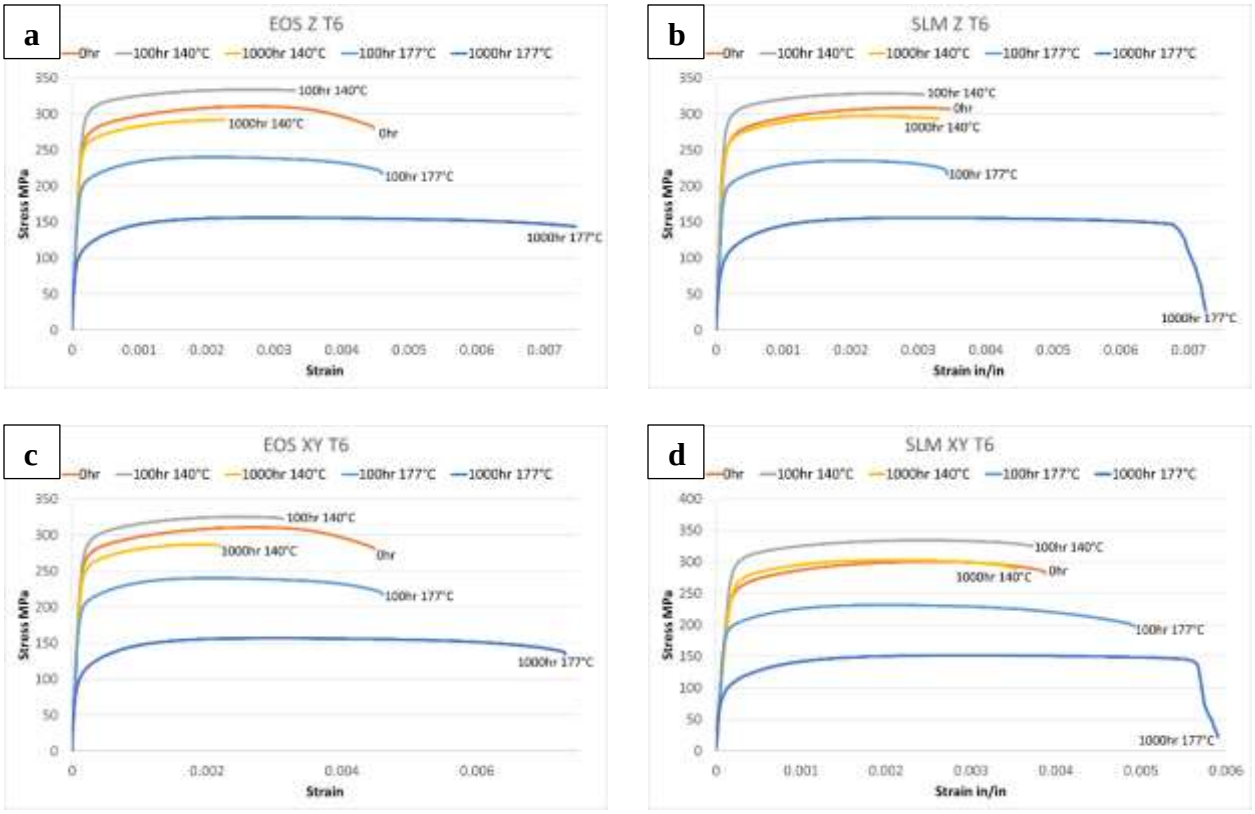


Figure 40. Characteristic curves for printed parts on a) EOS Z T6, b) SLM Z T6, c) EOS XY T6, d) SLM XY T6

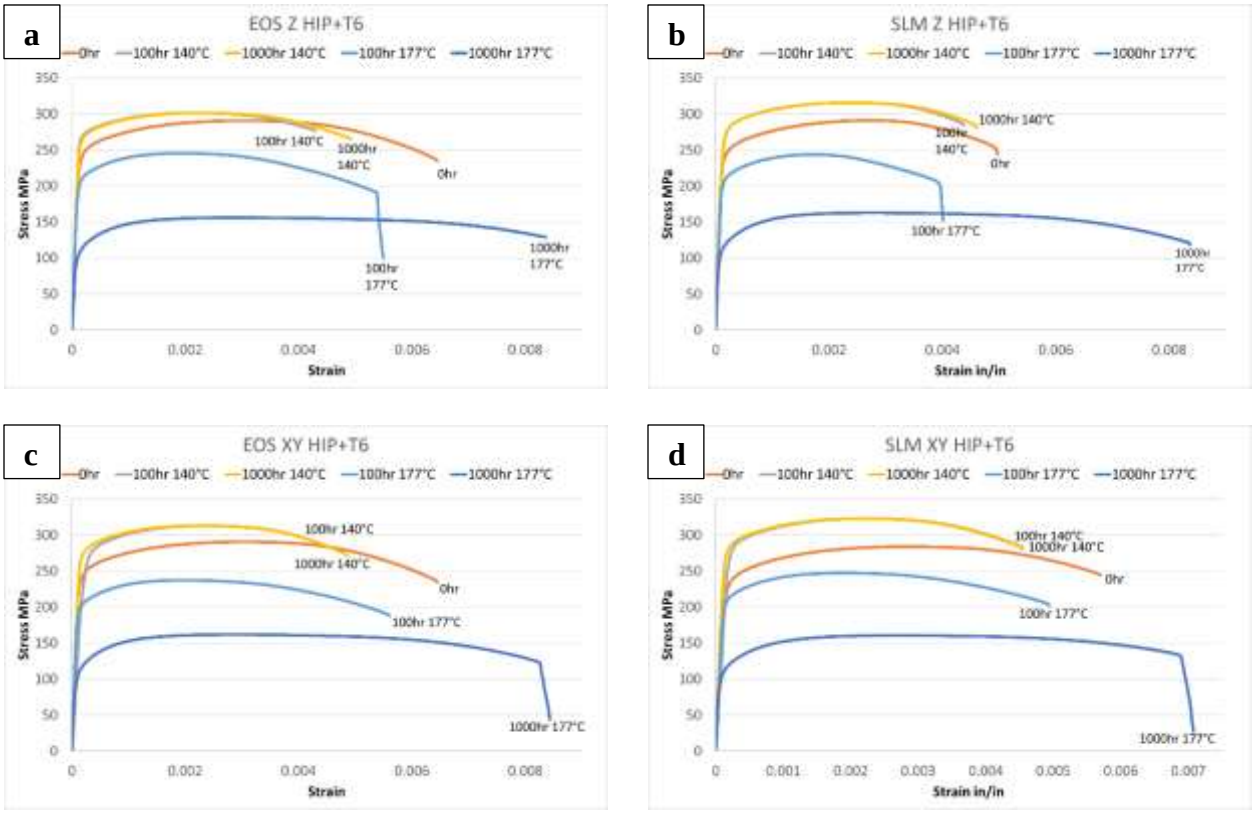


*Figure 41. Characteristic curves for printed parts on a) EOS Z HIP+T6, b) SLM Z HIP+T6, c) EOS XY HIP+T6, d) SLM XY HIP+T6*

Figures 39 to 41 demonstrate that there is a prevalent occurrence of steep softening in HIPed and aged tensile components that were fabricated in the Z and XY directions using both the EOS and SLM systems. The steep softening is particularly noticeable in the XY direction, as shown in Figure 39 (c) and (d). These findings suggest that in certain applications, components made of AlSi7Mg alloy that are fabricated in the XY direction using either the EOS or SLM systems may be of concern after undergoing HIP and aging. This is due to a broader range of lower strengths, which is in contrast to other heat treatments.

## 4.2 Mechanical Properties

Two powder suppliers were used for this project; SLM printing uses atomized F357(Alsi7Mg) by IMR Technologies; on the other hand, EOS system powder was provided by Valimet, and both powder chemical composition can be found in Table 1. Even with the different suppliers, mechanical properties results were consistent between different printers (EOS and SLM systems) after heat treat the specimens. The only condition that demonstrates a significant difference between the printers was the as-built samples, from yield stress, ultimate tensile strength, and elongation. In industry, heat treatments are necessary for every specimen and printed parts, and as it's demonstrated in Tables 6 to 9, after heat treat the specimens, the results remain consistent for the HIP, T6, Stress Relief, and HIP + T6 conditions, so the different powder feedstocks will not have a significant impact in this study, which gives greater importance to the project, because it demonstrates that even with different powder, different process strategy, different parameters, and machines, the results remain consistent after the heat treatment, that is required for any part in the industry nowadays.

Although Figures 31 to 41 provide a useful graphical overview and summary of the tensile properties - yield stress (YS), ultimate tensile strength (UTS), and elongation (%) - of the AlSi7Mg alloy components that were subjected to various heat treatments and aging processes, the actual measured values are not immediately apparent. The average measured values for mechanical properties (YS, UTS, and elongation), as well as the densities and micro indentation hardness (HV) values of the various components, are provided in Tables 6 to 9.

As evidenced by the stress-strain diagram comparisons and Tables 6 to 9, the yield stress (YS) and elongation values for the as-built components are reversed in comparison to those for the hot isostatic pressing (HIP) values. Specifically, the as-built YS values are approximately three

times higher than those of the HIP values, while the elongations for as-built components are roughly half of those for the HIP components. Furthermore, the YS and elongation values for XY-built components are generally higher than those for the corresponding as-built Z-direction components, whereas the HIP component values remain largely unchanged. This suggests that the microstructures and mechanical properties of the XY-built components are more homogenized. These findings are consistent across components fabricated using either the EOS or SLM systems, confirming that the mechanical properties of AlSi7Mg components fabricated and heat-treated from either LPBF system do not differ significantly.

Tables 6 to 9 also reveal that aging at 177°C for 1000 hours resulted in decreased yield stress and corresponding micro indentation hardness (HV) for all as-built, hot isostatic pressing (HIPed), T6, and HIP + T6 treated components, in both loading directions (Z and XY), for both the EOS and SLM LPBF systems. This contrasts with the unaged condition, where the YS and HV values were higher. The only exception to this trend was observed in the SR-treated components, where both the YS and HV values increased from the unaged condition.

Table 6. Mechanical properties and related data for as built, SR, HIP, T6 and HIP+T6 on EOS Z build direction

| EOS (Z) | | | | | | |
|---|---|---|---|---|---|---|
| Heat Treatment | Aging Condition | Avg. YS (Mpa) | Avg. UTS (MPa) | Avg Elongation (%) | Density (g/cm³) | Hardness (HV) |
| As Built | 0hr | 225 | 410 | 13.2 | 2.65 | 120 |
| | 100hr 140°C | 282 | 440 | 8.5 | 2.65 | 133 |
| | 1000hr 140°C | 212 | 372 | 9.2 | 2.65 | 115 |
| | 100hr 177°C | 196 | 348 | 8.3 | 2.66 | 104 |
| | 1000hr 177°C | 193 | 327 | 10.1 | 2.65 | 106 |
| SR | 0hr | 159 | 250 | 18.2 | 2.65 | 79 |
| | 100hr 140°C | 177 | 272 | 17.5 | 2.64 | 82 |
| | 1000hr 140°C | 160 | 246 | 18.1 | 2.65 | 79 |
| | 100hr 177°C | 170 | 261 | 15.9 | 2.65 | 89 |
| | 1000hr 177°C | 189 | 290 | 13.9 | 2.65 | 96 |
| HIP | 0hr | 87 | 132 | 25.3 | 2.65 | 51 |
| | 100hr 140°C | 88 | 133 | 35.4 | 2.63 | 50 |
| | 1000hr 140°C | 97 | 131 | 34.9 | 2.66 | 52 |
| | 100hr 177°C | 84 | 126 | 34.6 | 2.64 | 50 |
| | 1000hr 177°C | 81 | 118 | 41.3 | 2.65 | 44 |
| T6 | 0hr | 263 | 312 | 14.2 | 2.62 | 107 |
| | 100hr 140°C | 291 | 330 | 12.8 | 2.59 | 118 |
| | 1000hr 140°C | 264 | 303 | 10.0 | 2.62 | 112 |
| | 100hr 177°C | 201 | 237 | 14.2 | 2.66 | 88 |
| | 1000hr 177°C | 104 | 158 | 22.9 | 2.63 | 58 |
| HIP + T6 | 0hr | 205 | 258 | 18.7 | 2.66 | 60 |
| | 100hr 140°C | 309 | 350 | 15.7 | 2.66 | 123 |
| | 1000hr 140°C | 278 | 316 | 15.9 | 2.66 | 109 |
| | 100hr 177°C | 206 | 243 | 16.6 | 2.67 | 86 |
| | 1000hr 177°C | 109 | 158 | 27.2 | 2.65 | 59 |

Table 7. Mechanical properties and related data for as built, SR, HIP, T6 and HIP+T6 on SLM Z build direction

| SLM (Z) | | | | | | |
|---|---|---|---|---|---|---|
| Heat Treatment | Aging Condition | Avg. YS (Mpa) | Avg. UTS (Mpa) | Avg Elongation (%) | Density ($g/cm^3$) | Hardness (HV) |
| As Built | 0hr | 263 | 409 | 6.9 | 2.64 | 122 |
| | 100hr 140°C | 271 | 411 | 8.3 | 2.65 | 125 |
| | 1000hr 140°C | 202 | 350 | 9.3 | 2.65 | 106 |
| | 100hr 177°C | 182 | 321 | 9.7 | 2.62 | 102 |
| | 1000hr 177°C | 183 | 291 | 14.2 | 2.65 | 91 |
| SR | 0hr | 156 | 253 | 16.3 | 2.65 | 80 |
| | 100hr 140°C | 156 | 241 | 20.3 | 2.65 | 81 |
| | 1000hr 140°C | 149 | 237 | 21.6 | 2.65 | 77 |
| | 100hr 177°C | 158 | 251 | 19.7 | 2.65 | 81 |
| | 1000hr 177°C | 177 | 279 | 16.8 | 2.65 | 89 |
| HIP | 0hr | 85 | 135 | 31.3 | 2.65 | 51 |
| | 100hr 140°C | 88 | 136 | 36.1 | 2.64 | 51 |
| | 1000hr 140°C | 93 | 134 | 35.7 | 2.66 | 53 |
| | 100hr 177°C | 88 | 130 | 36.5 | 2.62 | 48 |
| | 1000hr 177°C | 80 | 119 | 41.8 | 2.65 | 47 |
| T6 | 0hr | 267 | 316 | 11.2 | 2.62 | 113 |
| | 100hr 140°C | 292 | 330 | 10.3 | 2.57 | 113 |
| | 1000hr 140°C | 268 | 299 | 10.9 | 2.63 | 110 |
| | 100hr 177°C | 201 | 240 | 12.1 | 2.58 | 87 |
| | 1000hr 177°C | 102 | 157 | 21.8 | 2.55 | 57 |
| HIP + T6 | 0hr | 199 | 258 | 19.2 | 2.67 | 65 |
| | 100hr 140°C | 314 | 352 | 17.6 | 2.66 | 126 |
| | 1000hr 140°C | 278 | 316 | 15.2 | 2.66 | 111 |
| | 100hr 177°C | 212 | 238 | 14.4 | 2.65 | 81 |
| | 1000hr 177°C | 111 | 160 | 24.3 | 2.65 | 58 |

The associated micro indentation hardness (HV) values show a trend that corresponds to the yield stress (YS) values. The as-built components with high YS values also have high HV values, while the HIP components with low YS values have correspondingly low HV values. In Tables 8 and 9, it is also observed that the YS values for products fabricated in the XY direction are approximately 12% higher than those fabricated in the Z direction. However, elongations for HIP components are generally similar for both Z and XY builds, with the highest elongations of around 40% uniformly occurring for HIP + aging at 177°C for 1000 hours.

The densities measured and shown in Tables 6 to 9 range from 2.53 g/cm3 to 2.67 g/cm3. However, this spread in measured densities does not appear to have any systematic heat treatment basis and is likely primarily due to measurement error. There is no correlation between the measured densities and the associated mechanical properties, including the micro indentation hardnesses. It should be noted that a previous study by Girelli, et al. [99], showed that solution treatments of AlSi10Mg at 540°C reduced the density due to the diffusion of dissolved hydrogen and increasing gas porosity. However, there is no evidence of these phenomena in the present study.

Although Tables 6 to 9 offer a comprehensive matrix for selecting mechanical properties and design strategies for LPBF-fabricated AlSi7Mg alloy products, comparing the properties, especially mechanical properties, can be challenging, even when examining stress-strain diagram comparisons in Figures 31 to 41. I have prepared a series of comparative and systematic bar graph summaries that illustrate the heat-treatment regimens and corresponding aging treatments for AlSi7Mg alloy fabricated in both the EOS and SLM LPBF systems and in both the Z and XY loading directions relative to the build direction. These bar graphs are shown in Figures 42 and 43.

Table 8. Mechanical properties and related data for as built, SR, HIP, T6 and HIP+T6 on EOS XY build direction

| EOS (XY) | | | | | | |
|---|---|---|---|---|---|---|
| Heat Treatment | Aging Condition | Avg. YS (Mpa) | Avg. UTS (MPa) | Avg Elongation (%) | Density ($g/cm^3$) | Hardness (HV) |
| As Built | 0hr | 257 | 410 | 17.2 | 2.65 | 122 |
| | 100hr 140°C | 311 | 421 | 14.6 | 2.66 | 136 |
| | 1000hr 140°C | 237 | 350 | 14.9 | 2.66 | 111 |
| | 100hr 177°C | 218 | 325 | 16.0 | 2.65 | 110 |
| | 1000hr 177°C | 199 | 298 | 20.1 | 2.67 | 97 |
| SR | 0hr | 163 | 249 | 20.4 | 2.65 | 79 |
| | 100hr 140°C | 170 | 252 | 23.8 | 2.66 | 90 |
| | 1000hr 140°C | 162 | 228 | 24.5 | 2.66 | 81 |
| | 100hr 177°C | 176 | 259 | 23.1 | 2.65 | 91 |
| | 1000hr 177°C | 189 | 278 | 23.1 | 2.53 | 91 |
| HIP | 0hr | 89 | 136 | 28.1 | 2.66 | 51 |
| | 100hr 140°C | 92 | 137 | 36.0 | 2.64 | 48 |
| | 1000hr 140°C | 95 | 135 | 35.6 | 2.67 | 51 |
| | 100hr 177°C | 86 | 127 | 35.5 | 2.63 | 48 |
| | 1000hr 177°C | 82 | 120 | 41.5 | 2.66 | 46 |
| T6 | 0hr | 263 | 315 | 12.8 | 2.62 | 109 |
| | 100hr 140°C | 291 | 330 | 10.2 | 2.62 | 113 |
| | 1000hr 140°C | 262 | 300 | 7.8 | 2.59 | 102 |
| | 100hr 177°C | 204 | 242 | 14.2 | 2.59 | 86 |
| | 1000hr 177°C | 104 | 150 | 17.8 | 2.58 | 55 |
| HIP + T6 | 0hr | 216 | 275 | 18.4 | 2.66 | 59 |
| | 100hr 140°C | 301 | 348 | 15.1 | 2.67 | 119 |
| | 1000hr 140°C | 281 | 320 | 13.6 | 2.64 | 105 |
| | 100hr 177°C | 199 | 240 | 17.7 | 2.68 | 87 |
| | 1000hr 177°C | 113 | 165 | 26.3 | 2.67 | 59 |

Table 9. Mechanical properties and related data for as built, SR, HIP, T6 and HIP+T6 on SLM XY build direction

| SLM (XY) | | | | | | |
|---|---|---|---|---|---|---|
| Heat Treatment | Aging Condition | Avg. YS (Mpa) | Avg. UTS (Mpa) | Avg Elongation (%) | Density (g/cm^3) | Hardness (HV) |
| As Built | 0hr | 295 | 412 | 13.1 | 2.65 | 133 |
| | 100hr 140°C | 283 | 392 | 11.8 | 2.65 | 130 |
| | 1000hr 140°C | 215 | 322 | 14.4 | 2.66 | 101 |
| | 100hr 177°C | 196 | 303 | 14.7 | 2.65 | 95 |
| | 1000hr 177°C | 188 | 285 | 16.5 | 2.67 | 93 |
| SR | 0hr | 155 | 241 | 19.3 | 2.65 | 79 |
| | 100hr 140°C | 164 | 234 | 18.0 | 2.65 | 81 |
| | 1000hr 140°C | 148 | 226 | 21.4 | 2.65 | 74 |
| | 100hr 177°C | 163 | 245 | 19.7 | 2.65 | 80 |
| | 1000hr 177°C | 180 | 254 | 17.5 | 2.65 | 90 |
| HIP | 0hr | 125 | 181 | 17.6 | 2.65 | 49 |
| | 100hr 140°C | 90 | 139 | 36.0 | 2.57 | 49 |
| | 1000hr 140°C | 95 | 137 | 32.6 | 2.66 | 49 |
| | 100hr 177°C | 88 | 129 | 35.7 | 2.56 | 47 |
| | 1000hr 177°C | 82 | 120 | 39.8 | 2.65 | 43 |
| T6 | 0hr | 260 | 311 | 12.9 | 2.63 | 107 |
| | 100hr 140°C | 295 | 334 | 10.4 | 2.56 | 120 |
| | 1000hr 140°C | 258 | 297 | 8.9 | 2.61 | 108 |
| | 100hr 177°C | 197 | 235 | 14.1 | 2.59 | 81 |
| | 1000hr 177°C | 103 | 156 | 19.8 | 2.67 | 56 |
| HIP + T6 | 0hr | 228 | 281 | 16.5 | 2.66 | 65 |
| | 100hr 140°C | 309 | 352 | 15.9 | 2.66 | 122 |
| | 1000hr 140°C | 286 | 326 | 13.9 | 2.67 | 111 |
| | 100hr 177°C | 210 | 247 | 14.3 | 2.66 | 89 |
| | 1000hr 177°C | 111 | 162 | 23.1 | 2.65 | 58 |

Notably, these comparative figures, one for each LPBF system, are essentially templates of each other, demonstrating the same trend described earlier. Additionally, Figure 13 for the EOS system is a template for the heat treatment schedule trends identified in LPBF fabrication of AlSi10Mg alloy components, as reported in Figure 5 of our previous article [5]. Moreover, it is observed that the as-built and as-built and aged components in Figures 42 and 43 exhibits a reversed trend for YS and UTS versus elongation, in contrast to HIP and aged components: higher YS and UTS exhibit lower elongations, while lower YS and UTS exhibit higher elongations.

Looking back at the introduction of this study, it is notable that prior research on post-process heat treatments for LPBF fabrication of AlSi10Mg alloy components has been more extensive compared to AlSi7Mg (F357) alloy. Recent studies by Vanzetti et al. and Fiocchi et al. have described short heat treatments for F357 (AlSi7Mg) alloy processed by LPBF, resulting in optimized yield stress values of 308 MPa and 257 MPa, respectively, with low elongation values. In contrast, the present study has demonstrated significantly higher elongation values at the same yield stress levels for as-built and aged AlSi7Mg components fabricated using both EOS and SLM LPBF systems. Recent optimization studies of T6 heat treatment parameters of cast AlSi7Mg alloy by Pezda have shown an increase in elongation of 250% at aging temperatures above 300°C, which is characteristic of HIP treatment and aging, as demonstrated in the current study. However, few prior reports have examined HIP of LPBF-fabricated AlSi7Mg alloy.


Figure 42. Comparative bar graphs showing mechanical properties for F357 on EOS printer, under different aging conditions for the different heat treatments and built in Z and XY orientation, a), d) Yield strength, b), e) UTS and c), f) Elongation; notice strength decreases with aging in a), b), d) and e), while elongation increases in c) and f) for T6, HIP and HIP+T6.

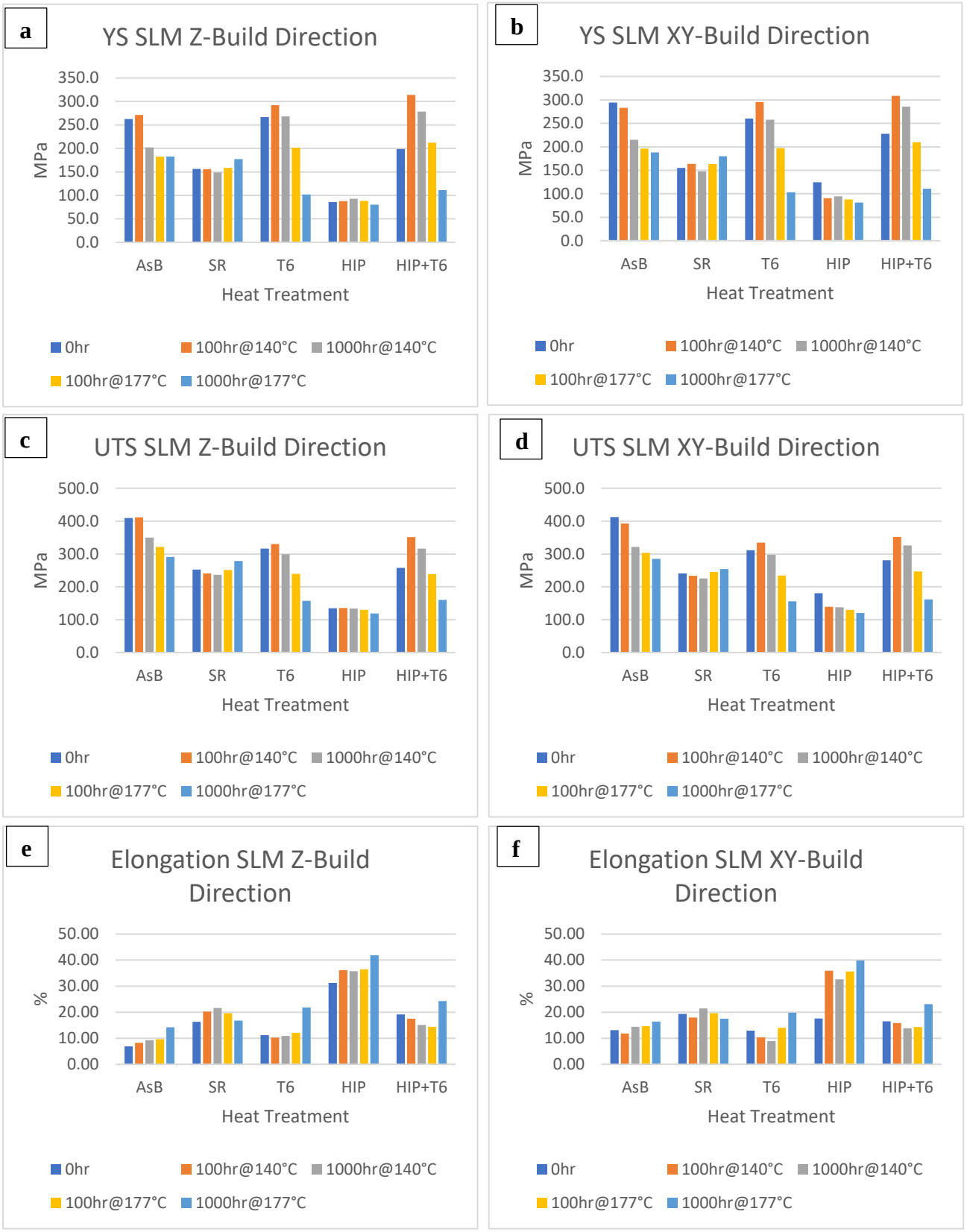


Figure 43. Comparative bar graphs showing mechanical properties for F357 on SLM printer, under different aging conditions for the different heat treatments and built in Z and XY orientation, a), d) Yield strength, b), e) UTS and c), f) Elongation; notice strength decreases with aging in a), b), d) and e), while elongation increases in c) and f) for T6, HIP and HIP+T6.

A recent study by Oliveira de Menezes et al. for LPBF fabrication of AlSi7Mg alloy found notable anisotropy in mechanical properties between components built parallel and perpendicular to the build direction (Z), which can be reduced or eliminated by heat treatment (such as T6 temper) as observed for numerous other aluminum alloys, as well as many other metals and alloys. The current study has also observed anisotropy in yield stress values (~16%) between AlSi7Mg alloy components built in both the EOS and SLM LPBF systems in the Z and XY loading directions. However, after T6 treatment, the anisotropy is reduced, with similar yield stress values observed in both directions in the EOS system, and a smaller difference in the SLM system. This information is presented in Tables 6-9.

## 4.3 Fracture surface structure and discussion

Figures 44 to 46 depict various SEM fracture surface images for AlSi7Mg (F357) alloy fabricated using the EOS system in different conditions. Figure 44 displays low-magnification images of the ripple surface features of the alloy in the as-built (Z) direction, aged for 1000 hours at 140 °C and aged for 100 hours at 177 °C. These images show similar surface features, which appear as small and shallow, equiaxed ductile dimples at high magnification. The average size of the dimples in Figure 44 (d) to (f) is approximately 0.3 to 0.35 microns, corresponding to the same micro dendritic cell size. The yield stress/elongation values for these aging conditions are 225 MPa/13.2 %, 212 MPa/9.2 %, and 193 MPa/10.1 %, respectively (Table 6).

On the other hand, Figure 45 shows larger and deeper ductile dimple features for the EOS(Z)-built and HIP components that are unaged, aged for 1000 hours at 140 oC, and aged for 1000 hours at 177 oC. The dimple sizes in each case average around 3 microns, which is approximately ten times larger than those in the as-built and aged components in Figure 44. The corresponding yield stress/elongation values for these conditions are 87 MPa/25 %, 97 MPa/35 %,

and 81 MPa/41 %, respectively (Table 6). These images demonstrate that the size of the dimples increases as the aging temperature declines, indicating a decline in yield stress values.

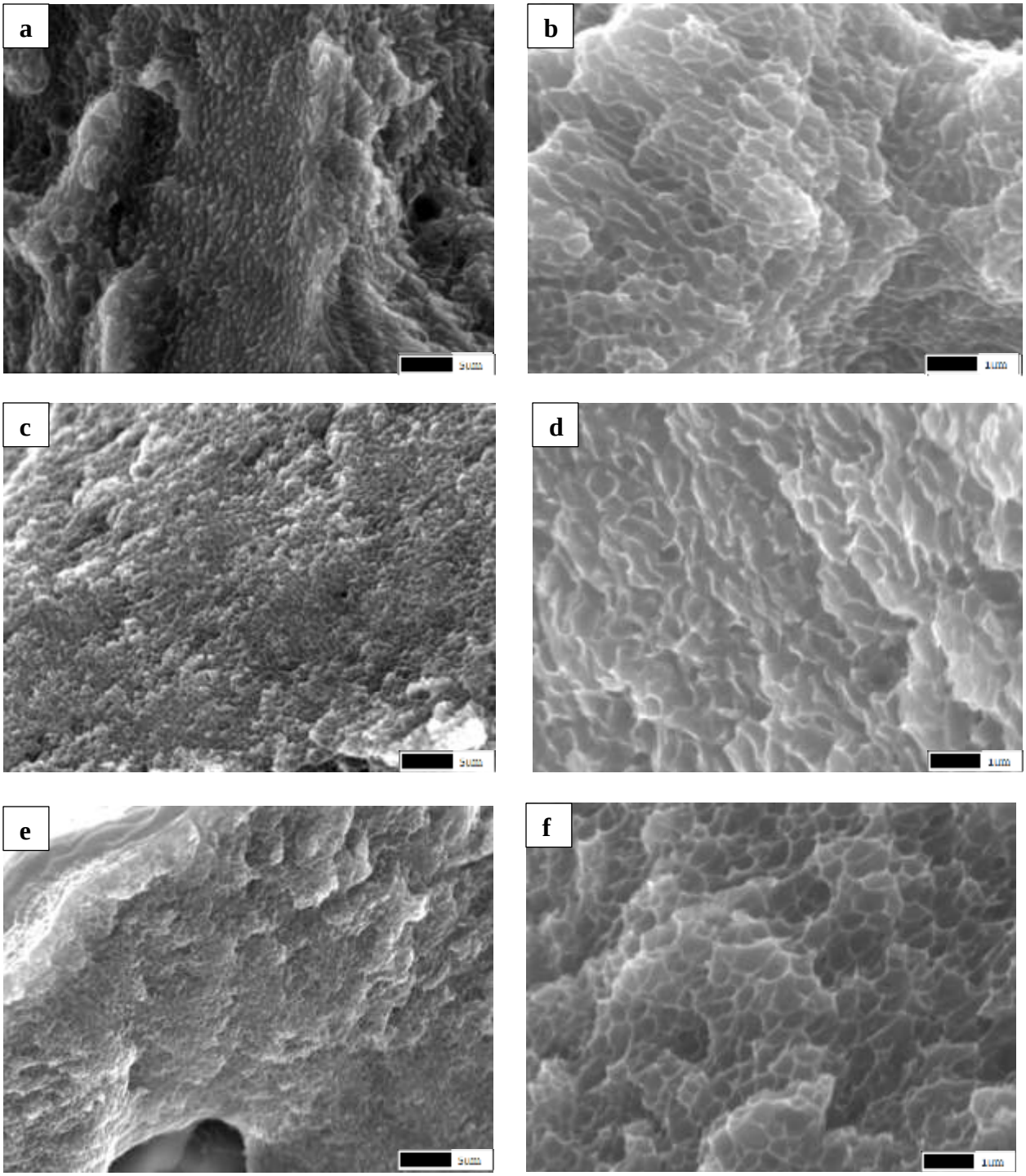


Figure 44. SEM fractographs of As-built EOS Z F357 aluminum samples at different aging conditions, a) 0hr and c) 1000hr at 140°C, e) 1000hr at 177°C at x3,500 magnification, b) 0hr, d) 1000hr at 140°C, f) 1000hr at 177°C at x12,000 magnification.

Figure 46 depicts the EOS-fabricated F357 alloy components that underwent HIP + T6 treatment (Figure 46 (a)) and aging at 140 °C (Figure 46 (c)) and 177 °C (Figure 46 (e)) for 1000 hours. The corresponding yield stress/elongation values for these figures were 205 MPa/19%, 278 MPa/16%, and 109 MPa/27%, respectively. The dimple sizes in Figure 46 were found to be slightly larger compared to those in Figure 45, with an average size of ~4 microns in Figure 46 (a) and (c), and ~5 microns in Figure 46 (e) for higher temperature aging. It is worth noting that the yield stress/elongation of the as-built and 1000-hour aged components at 177 °C (Figure 44 (e)) changed from 193 MPa/10% to 81 MPa/41% for the HIP-treated and aged components (Table 6), resulting in an increase in dimple size and depth by a factor of ~10. Similar to our previous study on LPBF-fabricated and heat-treated AlSi10Mg alloy [5], the observed fracture dimple phenomena is consistent with numerous published studies that relate dimple size to YS, elongation, and grain size, with dimple size ~=(grain size)0.5 [100], [101], ~1/(YS)1.2 [102], and dimple geometry correlations [103], [104]. Additionally, Manjunath, et al. [105] demonstrated that fracture dimple size decreases with equal channel angular pressing from ~5-20 microns to 0.3 microns.

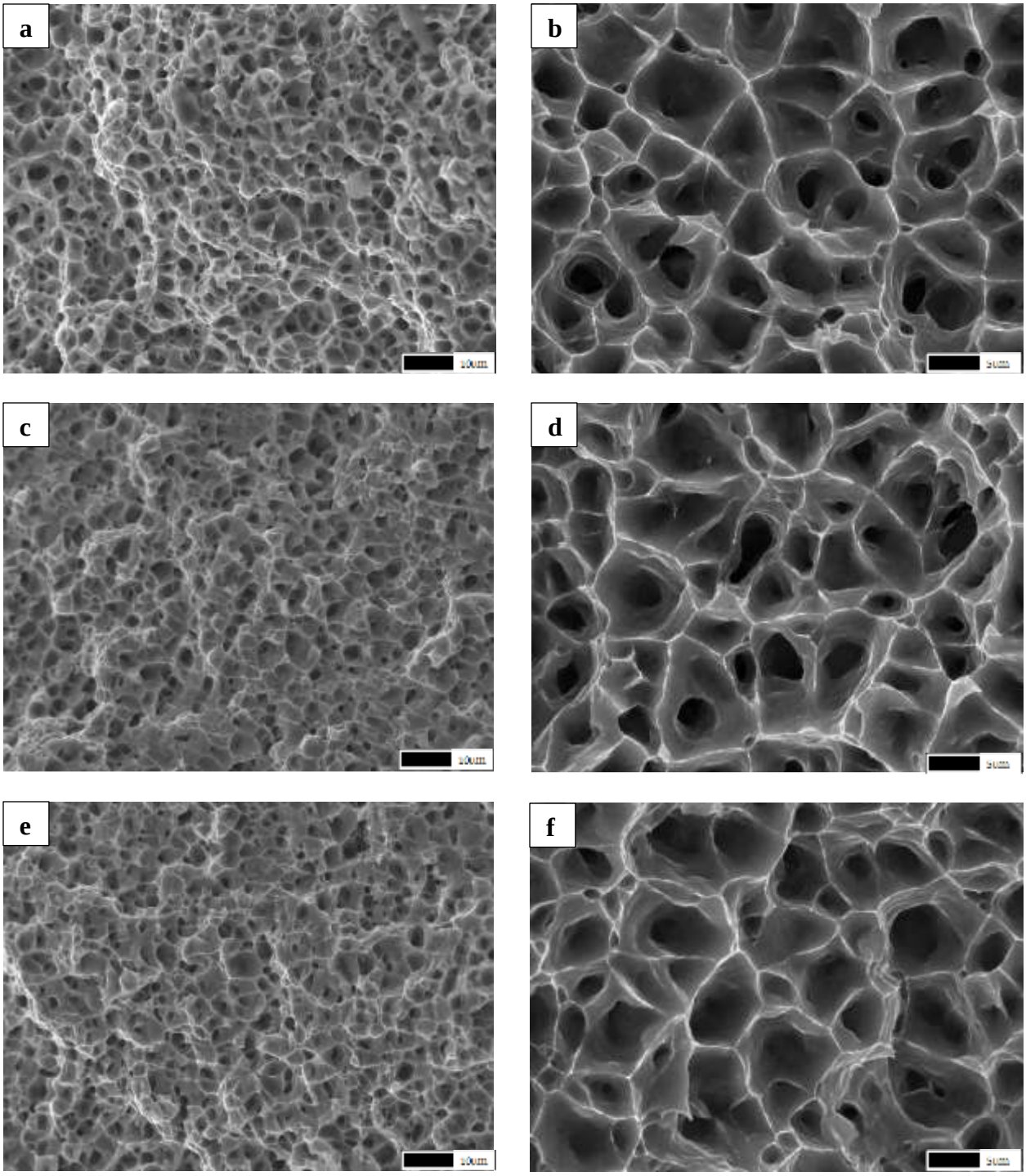


Figure 45. SEM fractographs of HIP EOS Z F357 aluminum samples at different aging conditions, a) 0hr and c) 1000hr at 140°C, e) 1000hr at 177°C, at x1000 magnification, b) 0hr and d) 1000hr at 140°C, f) 1000hr at 177°C, at x3500 magnification

It is noteworthy that the ductile dimple characteristics are also noticeable in both the as-built EOS (Z) F357 alloy components (Figure 44) and the HIP + T6 and aged alloy components (Figure 46). However, the dimple sizes are even larger for higher yield stress values and smaller elongations. This deviation is attributed to the microstructure features mentioned earlier in Figures 33 and 35, which compare the EOS (Z) as-built and aged, as-built and HIPed, and aged F357 alloy components (also see Table 6). These microstructure features are similar to those previously observed in LPBF-fabricated and heat-treated AlSi10Mg alloy (A356) [5].

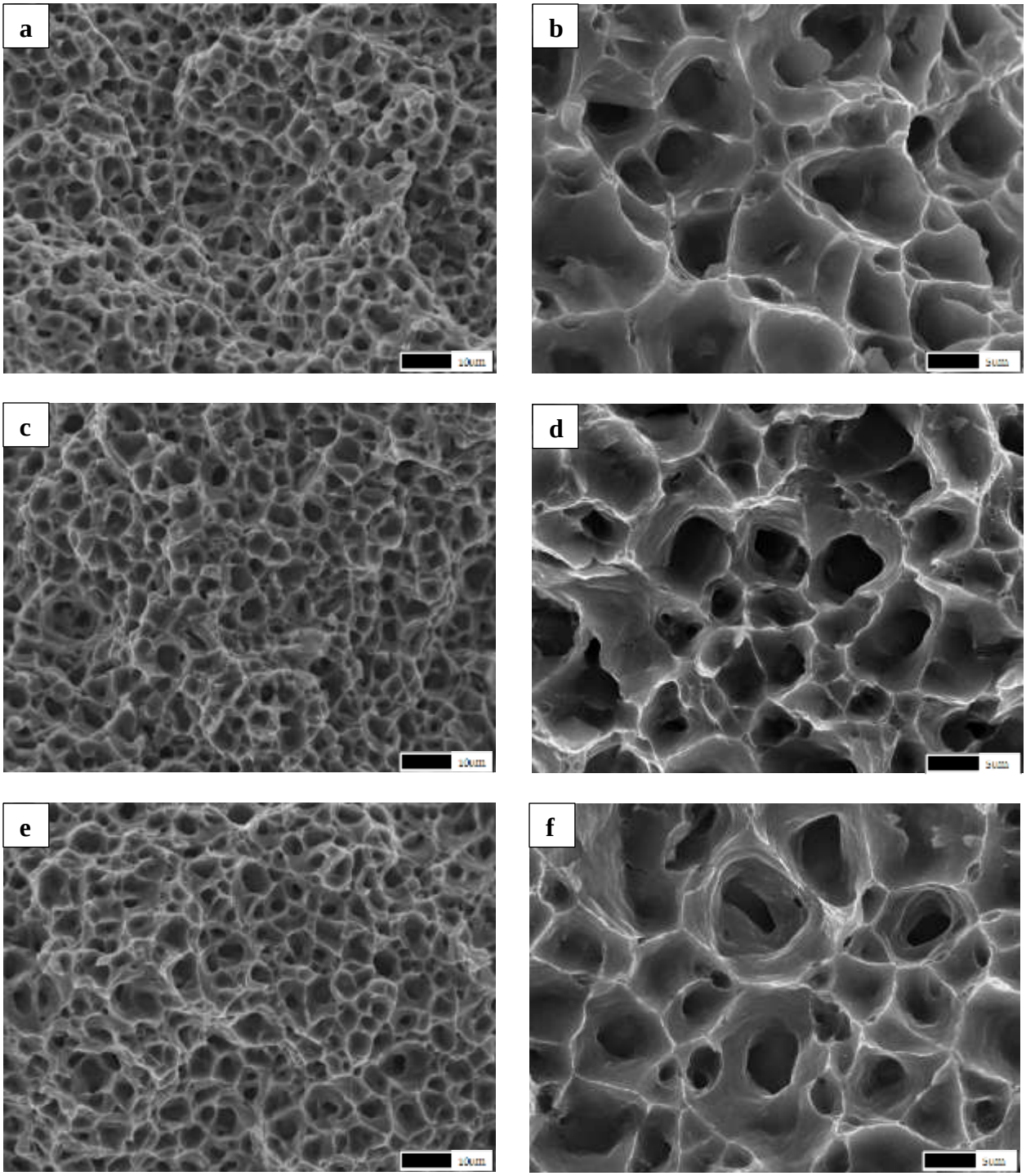


Figure 46. SEM fractographs of HIP+T6 EOS Z F357 aluminum samples at different aging conditions, a) 0hr and c) 1000hr at 140°C, e) 1000hr at 177°C, at x1000 magnification, b) 0hr and d) 1000hr at 140°C, f) 1000hr at 177°C, at x3500 magnification

# CHAPTER 5: CONCLUSION

This research program stands out as one of the most extensive investigations into LPBF fabrication and heat treatment of AlSi7Mg (F357) alloy and probably any other aluminum alloy system. The program produced LPBF-fabricated F357 alloy components in the as-built condition using two different commercial systems: EOS M290 and SLM 280HL. Tensile specimens were created in both the Z(build) and XY loading directions in each LPBF system. These as-built tensile components underwent aging for 100 hours and 1000 hours at 140 °C and 177 °C, respectively. They were also heat-treated using stress relief (SR) anneal, HIP, at 515 °C, T6 treatment at 530 °C, and HIP + T6 treatment. Each of these treatment schedules was followed by the aging treatments mentioned previously. The different, as-built tensile heat treatment and aging schedules resulted in 1600 measurements, which included 0.2 % offset yield stress (YS), ultimate tensile strength (UTS), elongation (%), and micro indentation hardness (HV). Additionally, 100 density measurements were taken for each of these specific measured properties, as outlined in Tables 4-7.

Optical metallography was utilized to characterize a wide range of microstructures corresponding to the mechanical property measurements described above, and SEM imaging was used to compare corresponding and representative fracture surface structures. The microstructures of the as-built and aged components were characterized by layer thickness-related melt bands and micro dendritic cell structures. Upon heat treatment, recrystallized grains varying in size from ~ 12 to 15 microns were observed, with eutectic Si particles at the grain boundaries and within the grains. For HIP components, these Si particles were relatively dense and generally globular with diameters of ~ 1 micron. However, for T6 and HIP + T6 treated and aged components, the Si particles became much coarser with irregular shapes and sizes of ~ 5 microns. The corresponding

SEM fracture surface images showed shallow, ductile dimples with sizes ranging from 0.3 to 0.35 microns. In contrast, the HIP, T6, and HIP + T6 treated component fracture surfaces exhibited much larger ductile dimples ranging in size from 3 to 5 microns.

The LPBF-fabricated AlSi7Mg alloy components displayed a classic anisotropy between the Z and XY loading direction mechanical properties for each LPBF system, as observed in many other LPBF-fabricated aluminum alloys and other alloy systems. For instance, the unaged YS for EOS (Z) was 225 MPa, while the unaged YS for EOS (XY) was 257 MPa. Similarly, the unaged YS for SLM (Z) was 263 MPa, whereas, for SLM (XY), it was 295 MPa. Similar values were also observed for LPBF-fabricated AlSi10Mg alloy. The associated micro indentation hardness (HV) measurements for the LPBF-fabricated AlSi7Mg alloy components were also consistent. The HV for EOS (Z) and EOS (XY) were HV 120 and HV 122, respectively, while SLM (Z) and SLM (XY) hardnesses were HV 122 and HV 133, respectively.

The T6 treatment + 100 h aging at 140°C consistently yielded the highest YS values, as evidenced by the EOS (Z) and (XY) components with YS of 291 MPa and 292 MPa, respectively, and the SLM (Z) and (XY) components with YS of 292 MPa and 295 MPa, respectively. Notably, the variance in YS values was narrow, ranging from only 291 MPa to 295 MPa (Tables 6-9), while elongation ranged from 10% to 13% (with hardness ranging from HV 113 to HV 107). In contrast, components that were HIPed and aged for 1000 h at 177°C exhibited the lowest YS values, ranging from 80 MPa to 82 MPa, with corresponding elongations ranging from 40% to 42% (Tables 6-9). These findings demonstrate the wide range of mechanical property design strategies available for LPBF-fabricated, heat-treated, and aged AlSi7Mg (F357) alloy components.

Specific conclusions which can generally be drawn from this research program are as follows:

- Although only two different LPBF systems (EOS and SLM) were compared in this study, it would appear that machine differences do not significantly alter AlSi7Mg alloy products produced, and any inhomogeneities and anisotropies are erased as a result of heat treatment, especially HIP, T6 and HIP + T6 treatments.
- As-built AlSi7Mg alloy products fabricated in the build (Z) direction varied in yield stress from 225 MPa to 295 MPa in this study; with corresponding elongation variations 0f 7 % to 17 %. These properties reflect the most economical and process efficient strategy.
- While HIP treatment can produce a homogenized microstructure even without aging, the resulting yield stress values were observed to vary from 85 MPa to 87 MPa for Z-direction fabricated components; with corresponding elongations varying from 25 % to 31 %. The highest elongation was observed for HIP + 1000 h aging at 177 oC: 42 %.
- Bar graph representations of the tensile properties (YS, UTS, elongation) for both the LPBF systems heat treated and heat treated + aging (as shown in Figures 13 and 14) were templates of one another.

# REFERENCES


[1] P. A. Rometsch, Y. Zhu, X. Wu, and A. Huang, “Review of high-strength aluminium alloys for additive manufacturing by laser powder bed fusion,” *Materials & Design*, vol. 219, p. 110779, Jul. 2022, doi: 10.1016/j.matdes.2022.110779.

[2] I. M. Kusoglu, B. Gökce, and S. Barcikowski, “Research trends in laser powder bed fusion of Al alloys within the last decade,” *Additive Manufacturing*, vol. 36, p. 101489, Dec. 2020, doi: 10.1016/j.addma.2020.101489.

[3] R. Krishna, M. Manjaiah, and C. B. Mohan, “Chapter 3 - Developments in additive manufacturing,” in *Additive Manufacturing*, M. Manjaiah, K. Raghavendra, N. Balashanmugam, and J. P. Davim, Eds., in Woodhead Publishing Reviews: Mechanical Engineering Series. Woodhead Publishing, 2021, pp. 37–62. doi: 10.1016/B978-0-12-822056-6.00002-3.

[4] M. Theron, R. D. Knutsen, L. H. Ivanchev, and H. P. Burger, “Effect of heat treatment on the properties of laser-beam welded rheo-cast F357 aluminum,” *Journal of Materials Processing Technology*, vol. 212, no. 2, pp. 465–470, Feb. 2012, doi: 10.1016/j.jmatprotec.2011.10.010.

[5] J. Merino *et al.*, “Multiple, comparative heat treatment and aging schedules for controlling the microstructures and mechanical properties of laser powder bed fusion fabricated AlSi10Mg alloy,” *Journal of Materials Research and Technology*, vol. 13, pp. 669–685, Jul. 2021, doi: 10.1016/j.jmrt.2021.04.062.

[6] M. Rashad *et al.*, “Improved strength and ductility of magnesium with addition of aluminum and graphene nanoplatelets (Al+GNPs) using semi powder metallurgy method,” *Journal of Industrial and Engineering Chemistry*, vol. 23, pp. 243–250, Mar. 2015, doi: 10.1016/j.jiec.2014.08.024.

[7] K. Tsaknopoulos, J. Grubbs, M. Siopis, A. Nardi, and D. Cote, “Microstructure and Mechanical Property Evaluation of Aluminum F357 Powder for Cold Spray Applications,” *J Therm Spray Tech*, vol. 30, no. 3, pp. 643–654, Feb. 2021, doi: 10.1007/s11666-020-01140-4.

[8] A. K. Dahle, K. Nogita, S. D. McDonald, C. Dinnis, and L. Lu, “Eutectic modification and microstructure development in Al–Si Alloys,” *Materials Science and Engineering: A*, vol. 413–414, pp. 243–248, Dec. 2005, doi: 10.1016/j.msea.2005.09.055.

[9] “Aluminum A357.0-T61, Permanent Mold Cast.” https://www.matweb.com/search/datasheet.aspx?matguid=3033751a102b4fd08bc568f0784ac907&ckck=1 (accessed Sep. 26, 2022).

[10] M. Vanzetti *et al.*, “Short Heat Treatments for the F357 Aluminum Alloy Processed by Laser Powder Bed Fusion,” *Materials*, vol. 14, no. 20, p. 6157, Oct. 2021, doi: 10.3390/ma14206157.

[11] H. Möller, G. Govender, S. Waldo, and P. Pistorius, “Comparison of heat treatment response of semisolid metal processed alloys A356 and F357,” *International Journal of Cast Metals Research*, vol. 23, Feb. 2010, doi: 10.1179/174313309X451252.

[12] A. Jadhav and V. S. Jadhav, “A review on 3D printing: An additive manufacturing technology,” *Materials Today: Proceedings*, vol. 62, pp. 2094–2099, Jan. 2022, doi: 10.1016/j.matpr.2022.02.558.

[13] D. Landi, F. C. Zefinetti, C. Spreafico, and D. Regazzoni, “Comparative life cycle assessment of two different manufacturing technologies: laser additive manufacturing and traditional technique,” *Procedia CIRP*, vol. 105, pp. 700–705, Jan. 2022, doi: 10.1016/j.procir.2022.02.117.

[14] M. Rinaldi, M. Caterino, M. Fera, P. Manco, and R. Macchiaroli, “Technology selection in green supply chains - the effects of additive and traditional manufacturing,” *Journal of Cleaner Production*, vol. 282, p. 124554, Feb. 2021, doi: 10.1016/j.jclepro.2020.124554.

[15] Y. Chen *et al.*, “Ultra-fast laser ultrasonic imaging method for online inspection of metal additive manufacturing,” *Optics and Lasers in Engineering*, vol. 160, p. 107244, Jan. 2023, doi: 10.1016/j.optlaseng.2022.107244.

[16] M. Armstrong, H. Mehrabi, and N. Naveed, “An overview of modern metal additive manufacturing technology,” *Journal of Manufacturing Processes*, vol. 84, pp. 1001–1029, Dec. 2022, doi: 10.1016/j.jmapro.2022.10.060.

[17] “What is CAD (Computer-Aided Design)?,” *WhatIs.com*. https://www.techtarget.com/whatis/definition/CAD-computer-aided-design (accessed Nov. 08, 2022).

[18] Y. Wang, M. Xiao, Z. Xia, P. Li, and L. Gao, “From Computer-Aided Design (CAD) Toward Human-Aided Design (HAD): An Isogeometric Topology Optimization Approach,” *Engineering*, Aug. 2022, doi: 10.1016/j.eng.2022.07.013.

[19] M. A., R. K. Y., and K. L., “Improve the accuracy, surface smoothing and material adaption in STL file for RP medical models,” *Journal of Manufacturing Processes*, vol. 21, pp. 46–55, Jan. 2016, doi: 10.1016/j.jmapro.2015.11.006.

[20] J. Weidner and M. Farfaglia, “Considerations for optimizing surface finishing of 3D printed metal parts,” *Metal Powder Report*, Mar. 2021, doi: 10.1016/j.mprp.2021.02.002.

[21] D. A. Lesyk, S. Martinez, B. N. Mordyuk, O. O. Pedash, V. V. Dzhemelinskyi, and A. Lamikiz, “Ultrasonic surface post-processing of hot isostatic pressed and heat treated

superalloy parts manufactured by laser powder bed fusion," *Additive Manufacturing Letters*, vol. 3, p. 100063, Dec. 2022, doi: 10.1016/j.addlet.2022.100063.

[22] W. Abd-Elaziem *et al.*, "On the current research progress of metallic materials fabricated by laser powder bed fusion process: a review," *Journal of Materials Research and Technology*, vol. 20, pp. 681–707, Sep. 2022, doi: 10.1016/j.jmrt.2022.07.085.

[23] S. Patel, H. Chen, M. Vlasea, and Y. Zou, "The influence of beam focus during laser powder bed fusion of a high reflectivity aluminium alloy — AlSi10Mg," *Additive Manufacturing*, vol. 59, p. 103112, Nov. 2022, doi: 10.1016/j.addma.2022.103112.

[24] X. Zhang and F. Liou, "Chapter 1 - Introduction to additive manufacturing," in *Additive Manufacturing*, J. Pou, A. Riveiro, and J. P. Davim, Eds., in Handbooks in Advanced Manufacturing. Elsevier, 2021, pp. 1–31. doi: 10.1016/B978-0-12-818411-0.00009-4.

[25] M. Leary, "Chapter 11 - Powder bed fusion," in *Design for Additive Manufacturing*, M. Leary, Ed., in Additive Manufacturing Materials and Technologies. Elsevier, 2020, pp. 295–319. doi: 10.1016/B978-0-12-816721-2.00011-7.

[26] P. Durai Murugan *et al.*, "A current state of metal additive manufacturing methods: A review," *Materials Today: Proceedings*, Dec. 2021, doi: 10.1016/j.matpr.2021.11.503.

[27] J. Zhang, B. Song, Q. Wei, D. Bourell, and Y. Shi, "A review of selective laser melting of aluminum alloys: Processing, microstructure, property and developing trends," *Journal of Materials Science & Technology*, vol. 35, no. 2, pp. 270–284, Feb. 2019, doi: 10.1016/j.jmst.2018.09.004.

[28] "Powder Bed Fusion - an overview | ScienceDirect Topics." https://www.sciencedirect.com/topics/engineering/powder-bed-fusion (accessed Nov. 10, 2022).

[29] Y. Li *et al.*, “Microstructure and mechanical properties of M2 high speed steel produced by electron beam melting,” *Materials Science and Engineering: A*, vol. 862, p. 144327, Jan. 2023, doi: 10.1016/j.msea.2022.144327.

[30] S. Dadbakhsh, X. Zhao, P. K. Chinnappan, V. Shanmugam, Z. Lin, and C. Hulme, “Process and geometrical integrity optimization of electron beam melting for copper,” *CIRP Annals*, vol. 71, no. 1, pp. 201–204, Jan. 2022, doi: 10.1016/j.cirp.2022.03.041.

[31] “Figure 2.9: A schematic diagram of the EBM process,” *ResearchGate*. https://www.researchgate.net/figure/A-schematic-diagram-of-the-EBM-process_fig9_335970676 (accessed Jan. 30, 2023).

[32] V. B. Vukkum and R. K. Gupta, “Review on corrosion performance of laser powder-bed fusion printed 316L stainless steel: Effect of processing parameters, manufacturing defects, post-processing, feedstock, and microstructure,” *Materials & Design*, vol. 221, p. 110874, Sep. 2022, doi: 10.1016/j.matdes.2022.110874.

[33] R. C. McCLUNG, “A literature survey on the stability and significance of residual stresses during fatigue,” *Fatigue & Fracture of Engineering Materials & Structures*, vol. 30, no. 3, pp. 173–205, 2007, doi: 10.1111/j.1460-2695.2007.01102.x.

[34] P. Sandmann *et al.*, “Influence of laser shock peening on the residual stresses in additively manufactured 316L by Laser Powder Bed Fusion: A combined experimental–numerical study,” *Additive Manufacturing*, vol. 60, p. 103204, Dec. 2022, doi: 10.1016/j.addma.2022.103204.

[35] Z. Snow, A. R. Nassar, and E. W. Reutzel, “Invited Review Article: Review of the formation and impact of flaws in powder bed fusion additive manufacturing,” *Additive Manufacturing*, vol. 36, p. 101457, Dec. 2020, doi: 10.1016/j.addma.2020.101457.

[36] E. O. Olakanmi, R. F. Cochrane, and K. W. Dalgarno, “A review on selective laser sintering/melting (SLS/SLM) of aluminium alloy powders: Processing, microstructure, and properties,” *Progress in Materials Science*, vol. 74, pp. 401–477, Oct. 2015, doi: 10.1016/j.pmatsci.2015.03.002.

[37] J. V. Gordon *et al.*, “Defect structure process maps for laser powder bed fusion additive manufacturing,” *Additive Manufacturing*, vol. 36, p. 101552, Dec. 2020, doi: 10.1016/j.addma.2020.101552.

[38] X. Li, Y. Liu, C. Tan, and Y. Zou, “Porosity formation mechanisms, microstructure evolution and mechanical performance of AlMgScZr alloy fabricated by laser powder bed fusion: Effect of hatch distance,” *Journal of Manufacturing Processes*, vol. 94, pp. 107–119, May 2023, doi: 10.1016/j.jmapro.2023.03.047.

[39] S. M. H. Hojjatzadeh *et al.*, “In-Situ Characterization of Pore Formation Dynamics in Pulsed Wave Laser Powder Bed Fusion,” *Materials*, vol. 14, no. 11, Art. no. 11, Jan. 2021, doi: 10.3390/ma14112936.

[40] “Figure 1. Formation of hydrogen-induced, keyhole, and lack-of-fusion...,” *ResearchGate*. https://www.researchgate.net/figure/Formation-of-hydrogen-induced-keyhole-and-lack-of-fusion-pores-during-laser-powder-bed_fig1_356648759 (accessed Apr. 03, 2023).

[41] S. Shrestha and K. Chou, “Formation of keyhole and lack of fusion pores during the laser powder bed fusion process,” *Manufacturing Letters*, vol. 32, pp. 19–23, Apr. 2022, doi: 10.1016/j.mfglet.2022.01.005.

[42] A. H, “Avoiding Defects in Laser Powder Bed Fusion,” *3Dnatives*, Dec. 16, 2020. https://www.3dnatives.com/en/avoiding-defects-in-laser-powder-bed-fusion-161220205/ (accessed Apr. 03, 2023).

[43] X. Yang, Y. Li, and B. Li, “Formation mechanisms of lack of fusion and keyhole-induced pore defects in laser powder bed fusion process: A numerical study,” *International Journal of Thermal Sciences*, vol. 188, p. 108221, Jun. 2023, doi: 10.1016/j.ijthermalsci.2023.108221.

[44] M. Zhang *et al.*, “Fatigue and Fracture Behaviour of Laser Powder Bed Fusion Stainless Steel 316 L: Influence of Processing Parameters,” *Materials Science and Engineering: A*, vol. 703, Jul. 2017, doi: 10.1016/j.msea.2017.07.071.

[45] “Figure 4 (a) Lack of fusion defects and un-melted powder in 0.7P0...,” *ResearchGate*. https://www.researchgate.net/figure/a-Lack-of-fusion-defects-and-un-melted-powder-in-07P0-vertical-plane-and-b_fig4_318646950 (accessed Apr. 03, 2023).

[46] W. Wang, J. Ning, and S. Y. Liang, “Analytical Prediction of Balling, Lack-of-Fusion and Keyholing Thresholds in Powder Bed Fusion,” *Applied Sciences*, vol. 11, no. 24, Art. no. 24, Jan. 2021, doi: 10.3390/app112412053.

[47] V. Lindström, G. Lupo, J. Yang, V. Turlo, and C. Leinenbach, “A simple scaling model for balling defect formation during laser powder bed fusion,” *Additive Manufacturing*, vol. 63, p. 103431, Feb. 2023, doi: 10.1016/j.addma.2023.103431.

[48] P. Hanzl, M. Zetek, T. Bakša, and T. Kroupa, “The Influence of Processing Parameters on the Mechanical Properties of SLM Parts,” *Procedia Engineering*, vol. 100, Dec. 2015, doi: 10.1016/j.proeng.2015.01.510.

[49] "Fig. 6. Balling increase with higher scanning speeds.," *ResearchGate*. https://www.researchgate.net/figure/Balling-increase-with-higher-scanning-speeds_fig14_264981022 (accessed Apr. 03, 2023).

[50] "(PDF) Reducing Porosity in AlSi10Mg Parts Processed by Selective Laser Melting." https://www.researchgate.net/publication/264981022_Reducing_Porosity_in_AlSi10Mg_Parts_Processed_by_Selective_Laser_Melting (accessed Apr. 03, 2023).

[51] T. DebRoy *et al.*, "Additive manufacturing of metallic components – Process, structure and properties," *Progress in Materials Science*, vol. 92, pp. 112–224, Mar. 2018, doi: 10.1016/j.pmatsci.2017.10.001.

[52] L. Vazquez, M. N. Rodriguez, I. Rodriguez, and P. Alvarez, "Influence of Post-Deposition Heat Treatments on the Microstructure and Tensile Properties of Ti-6Al-4V Parts Manufactured by CMT-WAAM," *Metals*, vol. 11, no. 8, Art. no. 8, Aug. 2021, doi: 10.3390/met11081161.

[53] F. Dababneh and H. Taheri, "Investigation of the influence of process interruption on mechanical properties of metal additive manufacturing parts," *CIRP Journal of Manufacturing Science and Technology*, vol. 38, pp. 706–716, Aug. 2022, doi: 10.1016/j.cirpj.2022.06.008.

[54] N. Jin, Z. Yan, Y. Wang, H. Cheng, and H. Zhang, "Effects of heat treatment on microstructure and mechanical properties of selective laser melted Ti-6Al-4V lattice materials," *International Journal of Mechanical Sciences*, vol. 190, p. 106042, Jan. 2021, doi: 10.1016/j.ijmecsci.2020.106042.

[55] A. K. Subramaniyan, A. S. Reddy, S. Mathias, A. Shrivastava, and P. Raghupatruni, "Influence of post-processing techniques on the microstructure, properties and surface

integrity of AlSiMg alloy processed by laser powder bed fusion technique," *Surface and Coatings Technology*, vol. 425, p. 127679, Nov. 2021, doi: 10.1016/j.surfcoat.2021.127679.

[56] C. Xu, W. Xiao, S. Hanada, H. Yamagata, and C. Ma, "The effect of scandium addition on microstructure and mechanical properties of Al–Si–Mg alloy: A multi-refinement modifier," *Materials Characterization*, vol. 110, pp. 160–169, Dec. 2015, doi: 10.1016/j.matchar.2015.10.030.

[57] J. J. S. Dilip *et al.*, "Influence of processing parameters on the evolution of melt pool, porosity, and microstructures in Ti-6Al-4V alloy parts fabricated by selective laser melting," *Prog Addit Manuf*, vol. 2, no. 3, pp. 157–167, Sep. 2017, doi: 10.1007/s40964-017-0030-2.

[58] E. Edin, F. Svahn, M. Neikter, and P. Åkerfeldt, "Stress relief heat treatment and mechanical properties of laser powder bed fusion built 21-6-9 stainless steel," *Materials Science and Engineering: A*, vol. 868, p. 144742, Mar. 2023, doi: 10.1016/j.msea.2023.144742.

[59] A. Banerjee *et al.*, "Effect of stress-relief heat treatments on the microstructure and mechanical response of additively manufactured IN625 thin-walled elements," *Materials Science and Engineering: A*, vol. 846, p. 143288, Jun. 2022, doi: 10.1016/j.msea.2022.143288.

[60] P. Dong, S. Song, and J. Zhang, "Analysis of residual stress relief mechanisms in post-weld heat treatment," *International Journal of Pressure Vessels and Piping*, vol. 122, pp. 6–14, Oct. 2014, doi: 10.1016/j.ijpvp.2014.06.002.

[61] P. Krakhmalev *et al.*, "Influence of heat treatment under hot isostatic pressing (HIP) on microstructure of intermetallic-reinforced tool steel manufactured by laser powder bed

fusion," *Materials Science and Engineering: A*, vol. 772, p. 138699, Jan. 2020, doi: 10.1016/j.msea.2019.138699.

[62] J. M. Alegre, A. Díaz, R. García, L. B. Peral, and I. I. Cuesta, "Effect of HIP post-processing at 850 °C/200 MPa in the fatigue behavior of Ti-6Al-4V alloy fabricated by Selective Laser Melting," *International Journal of Fatigue*, vol. 163, p. 107097, Oct. 2022, doi: 10.1016/j.ijfatigue.2022.107097.

[63] Y. Lu *et al.*, "The influence of heat treatment on the microstructure and properties of HIPped Ti-6Al-4V," *Acta Materialia*, vol. 165, pp. 520–527, Feb. 2019, doi: 10.1016/j.actamat.2018.12.025.

[64] S. Mirzababaei, B. K. Paul, and S. Pasebani, "Microstructure-property relationship in binder jet produced and vacuum sintered 316 L," *Additive Manufacturing*, vol. 53, p. 102720, May 2022, doi: 10.1016/j.addma.2022.102720.

[65] N. Mclean *et al.*, "Effect of Hot Isostatic Pressing and heat treatments on porosity of Wire Arc Additive Manufactured Al 2319," *Journal of Materials Processing Technology*, vol. 310, p. 117769, Dec. 2022, doi: 10.1016/j.jmatprotec.2022.117769.

[66] S. M. J. Razavi, A. Avanzini, G. Cornacchia, L. Giorleo, and F. Berto, "Effect of heat treatment on fatigue behavior of as-built notched Co-Cr-Mo parts produced by Selective Laser Melting," *International Journal of Fatigue*, vol. 142, p. 105926, Jan. 2021, doi: 10.1016/j.ijfatigue.2020.105926.

[67] A. Kurdi and A. K. Basak, "Micro-mechanical behaviour of selective laser melted Ti6Al4V under compression," *Materials Science and Engineering: A*, vol. 826, p. 141975, Oct. 2021, doi: 10.1016/j.msea.2021.141975.

[68] Y. Jiao, B. Tang, J. Wang, P. Jin, and X. Jiang, “Effects of the T6 heat treatment on the tribological behaviors of SiCp/7055Al composites,” *Materials Today Communications*, vol. 33, p. 104670, Dec. 2022, doi: 10.1016/j.mtcomm.2022.104670.

[69] X. Wang, Y. Wang, C. Ni, Y. Fang, X. Yu, and P. Zhang, “The effect of T4 and T6 heat treatments for dynamic impact behavior of casting Mg-Gd-based alloys,” *Vacuum*, vol. 205, p. 111450, Nov. 2022, doi: 10.1016/j.vacuum.2022.111450.

[70] Q. Chen *et al.*, “Effect of T6 heat treatment on microstructure and mechanical properties of large-weight aluminum alloy flywheel housing parts formed by local-loading squeeze casting,” *Journal of Materials Research and Technology*, vol. 24, pp. 1612–1625, May 2023, doi: 10.1016/j.jmrt.2023.03.084.

[71] J. Bi *et al.*, “Microstructure, tensile properties and heat-resistant properties of selective laser melted AlMgScZr alloy under long-term aging treatment,” *Materials Science and Engineering: A*, vol. 833, p. 142527, Jan. 2022, doi: 10.1016/j.msea.2021.142527.

[72] Q. Deng *et al.*, “Influence of friction stir processing and aging heat treatment on microstructure and mechanical properties of selective laser melted Mg-Gd-Zr alloy,” *Additive Manufacturing*, vol. 44, p. 102036, Aug. 2021, doi: 10.1016/j.addma.2021.102036.

[73] K. Kuwabara, T. Kimura, H. Shiratori, and Y. Daigo, “Enhanced strengthening effect of aging heat treatment found in additively-formed CoCrFeNiTi-based multiprincipal element alloy,” *Materials Today Communications*, vol. 35, p. 105938, Jun. 2023, doi: 10.1016/j.mtcomm.2023.105938.

[74] F. M. Moniruzzaman *et al.*, “Study of direct aging heat treatment of additively manufactured PH13-8Mo stainless steel: role of the manufacturing process, phase

transformation kinetics, and microstructure evolution," *Journal of Materials Research and Technology*, Apr. 2023, doi: 10.1016/j.jmrt.2023.04.023.

[75] C. K. P. Vallabh, S. Sridar, W. Xiong, and X. Zhao, "Predicting melt pool depth and grain length using multiple signatures from in-situ single camera two-wavelength imaging pyrometry for laser powder bed fusion," *Journal of Materials Processing Technology*, vol. 308, p. 117724, Oct. 2022, doi: 10.1016/j.jmatprotec.2022.117724.

[76] S. Harsha and S. M. Dasharath, "Effect of cryogenic heat treatment & ageing on ultra fine grained aluminium–lithium alloy- A review," *Materials Today: Proceedings*, vol. 45, pp. 338–348, Jan. 2021, doi: 10.1016/j.matpr.2020.10.1009.

[77] S. Sadeghi Borujeni, A. Shad, K. Abburi Venkata, N. Günther, and V. Ploshikhin, "Numerical simulation of shrinkage and deformation during sintering in metal binder jetting with experimental validation," *Materials & Design*, vol. 216, p. 110490, Apr. 2022, doi: 10.1016/j.matdes.2022.110490.

[78] H. M. Wang *et al.*, "Microstructure and properties of spinning deformed A356 alloy subject to the solution-DCT-aging multiplex heat treatment," *Journal of Materials Research and Technology*, vol. 23, pp. 5520–5533, Mar. 2023, doi: 10.1016/j.jmrt.2023.02.157.

[79] P. Peng *et al.*, "Investigation on the influence of Ta on the microstructure evolution of Ni-based superalloy DZ411 during directional solidification, heat treatment, and long-term aging," *Journal of Alloys and Compounds*, vol. 920, p. 165886, Nov. 2022, doi: 10.1016/j.jallcom.2022.165886.

[80] "Mid-Size Metal 3D Printer for all kind of materials." https://www.eos.info/en/industrial-3d-printer/metal/eos-m-290 (accessed Mar. 21, 2023).

[81] “EOS M 290 - EOS.” https://na.eos.info/Equipment/Metal-Platforms/EOS-M-290 (accessed Mar. 23, 2023).

[82] “Leistungsstarker Metalldrucker mittlerer Größe,” *SLM Solutions*. https://www.slm-solutions.com/de/produkte-und-loesungen/maschinen/slm-280/ (accessed Mar. 21, 2023).

[83] “SLM 280HL – 3D-print EKZO.” https://www.3dprintekzo.be/products-services/3d-printers/slm-hl280/ (accessed Mar. 23, 2023).

[84] V. Alfieri, V. Giannella, F. Caiazzo, and R. Sepe, “Influence of position and building orientation on the static properties of LPBF specimens in 17-4 PH stainless steel,” *Forces in Mechanics*, vol. 8, p. 100108, Aug. 2022, doi: 10.1016/j.finmec.2022.100108.

[85] H. Möller, W. E. Stumpf, and P. C. Pistorius, “Influence of elevated Fe, Ni and Cr levels on tensile properties of SSM-HPDC Al-Si-Mg alloy F357,” *Transactions of Nonferrous Metals Society of China*, vol. 20, pp. s842–s846, Sep. 2010, doi: 10.1016/S1003-6326(10)60592-4.

[86] superadmin, “AccuPyc II,” *Micromeritics*, Sep. 29, 2020. https://www.micromeritics.com/accupyc-ii/ (accessed Mar. 21, 2023).

[87] “compass.” https://compass.astm.org/document/?contentCode=ASTM%7CF3318-18%7Cen-US&proxycl=https%3A%2F%2Fsecure.astm.org&fromLogin=true (accessed Mar. 23, 2023).

[88] “Landmark Servohydraulic Test Systems.” https://www.mts.com/en/products/materials/dynamic-materials-test-systems/landmark-servohydraulic (accessed Mar. 23, 2023).

[89] “AccuPyc II - Micromeritics AccyPyc Gas Displacement Pycnometer.” https://www.micromeritics.com/accupyc-ii/ (accessed Mar. 23, 2023).

[90] “Hot Mounting Press OPAL 480 - QATM Metallography.” https://www.qatm.com/products/mounting/opal-480/ (accessed Mar. 23, 2023).

[91] “Automatic grinding & polishing machine SAPHIR 560.” https://www.qatm.com/products/grinding-polishing-etching/automatic-grinder-polisher/saphir-560-rubin-520/ (accessed Mar. 23, 2023).

[92] “GX53 | Inverted Metallurgical Microscopes | Olympus.” https://www.olympus-ims.com/en/microscope/gx53/ (accessed Mar. 23, 2023).

[93] “Brinell / Knoop / Vickers Hardness Testing with the CHD Master+.” https://www.qatm.com/products/hardness-testing/micro-hardness-tester/q10-30-60-chd-master-plus/ (accessed Mar. 23, 2023).

[94] C. Zhang, H. Zhu, Y. Qi, and X. Zeng, “The Effect of Annealing on Microstructure and Mechanical Properties of Selective Laser Melting AlSi10Mg,” *IOP Conf. Ser.: Mater. Sci. Eng.*, vol. 538, no. 1, p. 012023, May 2019, doi: 10.1088/1757-899X/538/1/012023.

[95] C. B. Finfrock, A. Exil, J. D. Carroll, and L. Deibler, “Effect of Hot Isostatic Pressing and Powder Feedstock on Porosity, Microstructure, and Mechanical Properties of Selective Laser Melted AlSi10Mg,” *Metallogr. Microstruct. Anal.*, vol. 7, no. 4, pp. 443–456, Aug. 2018, doi: 10.1007/s13632-018-0456-z.

[96] “(PDF) Relationship between Duplex Grain Structure and Grain-boundary Precipitates in Ni2M-stabilized Alloy.” https://www.researchgate.net/publication/284578696_Relationship_between_Duplex_Grain_Structure_and_Grain-boundary_Precipitates_in_Ni2M-stabilized_Alloy (accessed Apr. 13, 2023).

[97] A. Pineau, A. A. Benzerga, and T. Pardoen, “Failure of metals I: Brittle and ductile fracture,” *Acta Materialia*, vol. 107, pp. 424–483, Apr. 2016, doi: 10.1016/j.actamat.2015.12.034.

[98] W. Wciślik and R. Pała, “Some Microstructural Aspects of Ductile Fracture of Metals,” *Materials (Basel)*, vol. 14, no. 15, p. 4321, Aug. 2021, doi: 10.3390/ma14154321.

[99] “Optimization of heat treatment parameters for additive manufacturing and gravity casting AlSi10Mg alloy - IOPscience.” https://iopscience.iop.org/article/10.1088/1757-899X/264/1/012016 (accessed Apr. 13, 2023).

[100] W. Qin *et al.*, “Effects of grain size on tensile property and fracture morphology of 316L stainless steel,” *Materials Letters*, vol. 254, pp. 116–119, Nov. 2019, doi: 10.1016/j.matlet.2019.07.058.

[101] “(PDF) Grain Size Effect on Fracture Behavior of the Axis-Tensile Test of Inconel 718 Sheet.” https://www.researchgate.net/publication/292074748_Grain_Size_Effect_on_Fracture_Behavior_of_the_Axis-Tensile_Test_of_Inconel_718_Sheet (accessed Apr. 13, 2023).

[102] Y. Sun, X. Li, X. Yu, D. Ge, J. Chen, and J. Chen, “Fracture Morphologies of Advanced High Strength Steel During Deformation,” *Acta Metall. Sin. (Engl. Lett.)*, vol. 27, no. 1, pp. 101–106, Feb. 2014, doi: 10.1007/s40195-014-0032-8.

[103] A. Das and S. Tarafder, “Geometry of dimples and its correlation with mechanical properties in austenitic stainless steel,” *Scripta Materialia*, vol. 59, no. 9, pp. 1014–1017, Nov. 2008, doi: 10.1016/j.scriptamat.2008.07.012.

[104] O. Hilders, N. Zambrano, and R. Caballero, “Microstructure, Strength, and Fracture Topography Relations in AISI 316L Stainless Steel, as Seen through a Fractal Approach and

the Hall-Petch Law," *International Journal of Metals*, vol. 2015, pp. 1–10, Jul. 2015, doi: 10.1155/2015/624653.

[105] G. K. Manjunath, G. V. Preetham Kumar, and K. Udaya Bhat, "Tensile Properties and Tensile Fracture Characteristics of Cast Al–Zn–Mg Alloys Processed by Equal Channel Angular Pressing," *Trans Indian Inst Met*, vol. 70, no. 3, pp. 833–842, Apr. 2017, doi: 10.1007/s12666-017-1067-0.

# VITA

Victor Adrián Medrano Balderas was born in Ciudad Juárez, Chihuahua, México. He spent his whole life in Mexico until he moved to El Paso, Texas, United States, to start studying college at the University of Texas at El Paso in 2016. Graduated in 2021 from his Bachelor of Science in Mechanical Engineering, and after graduating from his undergraduate degree, he starts his graduate degree, graduating in 2023 from his Master of Science in Mechanical Engineering.

Victor started working as lifeguard at the Student Recreation Center in 2019, but in 2021 he starts working as Graduate Research Assistant in the W.M. Keck Center for 3D Innovation at the University of Texas at El Paso (UTEP). His research focused on Laser Powder Bed Fusion, Binder Jetting, Simulation software for Binder Jetting parts, surface finish, powder analysis, heat treatments, metallography process, microstructure analysis, mechanical testing, hardness testing and analysis, fracture analysis, AlSi7Mg Alloy (F357), Stainless steel 316L, AlSi10Mg Alloy, among other projects and processes.

Contact Information
Email: vamedranoba@miners.utep.edu
Personal Email: victormedrano10@gmail.com
Phone contact: 915-838-6440

This thesis was typed by Victor Adrian Medrano Balderas